Univerzita Karlova v Praze,
1. Lékařská Fakulta

Studijní program (Study program): Doktorský (Doctoral)
Studijní obor (Committee): Lékařská biofyzika (Medical Biophysics)

Mgr. Soma Chakraborty

Kinematic analysis of rhythmic motion: the cases of human hand tremor and fly wingbeat

Kinematická analýza rytmických pohybů: aplikace na třes rukou člověka a kmit křídel mušky octomilky

Disertační práce (Dissertation)

Školitel (supervisor): RNDr. Martin Zápotocký, Ph.D.

Prague (2017)

Prohlášení (Declaration)

Prohlašuji, že jsem závěrečnou práci zpracovala samostatně pod dohledem RNDr. Martina Zápotockého, Ph.D. a že jsem řádně uvedla a citovala všechny použité prameny a literaturu. Současně prohlašuji, že práce nebyla využita k získání jiného nebo stejného titulu.

Souhlasím s trvalým uložením elektronické verze mé práce v databázi systému meziuniverzitního projektu Theses.cz za účelem soustavné kontroly podobnosti kvalifikačních prací.

English translation:

I declare that the work presented in this thesis is my original research work done under the supervision of RNDr. Martin Zápotocký, Ph.D. and that I have duly noted and cited all used sources and literature. I also declare that the work was not used to obtain any other or the same academic degree.

I hereby give consent for cataloguing an electronic version of this thesis in the interuniversity database system Theses.cz, for the purpose of systematic similarity checks of theses.

v Praze, 03.01.2017

Soma Chakraborty

Identification record

Chakraborty, Soma. *Kinematická analýza rytmických pohybů: aplikace na třes rukou člověka a kmit křídel mušky octomilky. [Kinematic analysis of rhythmic motion: the cases of human hand tremor and fly wingbeat].* Praha, 2017. 174 s.,0 příl. Disertační práce (PhD.). Univerzita Karlova v Praze, 1. lékařská fakulta. Vedoucí práce Zápotocký, Martin.

Acknowledgements

First and foremost I want to thank my advisor RNDr. Martin Zápotocký, Ph.D. for providing me the opportunity to undergo this formal training of academic research under his able guidance. He has taught me, both consciously and unconsciously, the fundamentals of a good scientific research. His diligence for his research has shown me how hard work and persistence results in an ultimate gain and this has kept me motivated even during the tough times in the Ph.D. pursuit. I appreciate all his contributions of time, ideas, and funding to make my Ph.D. experience productive and stimulating.

I gratefully acknowledge the funding sources that made my Ph.D. work possible. I especially thank the 1st Faculty of Medicine for the Ph.D. fellowship I received for 4 years and the Grant Agency of the Charles University for awarding me extra funding to support my research (project GAUK 676812). The various other sources from where I received support as team member are: Volkswagen Foundation (I/80 984-986), the Grant Agency of the Czech Republic (P304-12-G069), project PRVOUK P26/LF1/4, SVV NeST 2 (Charles University in Prague) and last but not least, institutional support RVO:67985823.

I would like to thank my collaborators from Fry Lab (INI, ETH Zurich and University of Zurich) and Department of Neurology and Center of Clinical Neuroscience at Charles University in Prague, who have contributed immensely to my professional development during my Ph.D. I owe my special thanks to my colleague from Fry Lab, Dr. Jan Bartussek, who has not only been a very helpful senior but also a good friend. I also thank the people of my department, the Department of Computational Neuroscience at the Institute of Physiology of the Czech Academy of Sciences, for providing me a helpful and stimulating work environment. My thanks are due to Daniel Smit, Stepan Kortus and my colleagues from the department of Neurophysiology of memory for being the primary source of my social life in a foreign land. Especially, Dr. Iveta Fajnerova who has helped me in several ways all these years and become one of my closest friends. My heartiest thanks to Ing. Asit Baran De and Mrs. Aparajita De for being like a family to me and making me feel at home.

In the end I express my gratitude for the paramount support and encouragement I received from my family all these years. Without their love and support this journey would have never been possible. My husband Dr. Nachiketa Chakraborty has always been my strongest support and morale booster, helping me sail through even the toughest of times. I find myself lucky to not only have parents and siblings who always stood by my side with their unwavering trust, but also in-laws who kept me going with their constant encouragement and unconditional support. I take this opportunity to thank them all. I owe special thanks to the newest member of my family and my most effective stress buster, my little daughter Shreya, whose birth has changed my entire perspective on life.

Abstrakt

Rytmický pohyb, pravidelný nebo nepravidelný, je nedílnou součástí motorického chování a to jak ve zdraví, tak v průběhu nemoci. Hlubší pochopení geneze rytmického pohybu je důležité pro porozumění patofyziologii onemocnění, mezi jejichž projevy rytmický pohyb patří. V disertační práci jsem studovala dva konkrétní aspekty rytmického pohybu: bilaterální koordinaci a modulární řízení. První z nich jsem analyzovala na třesu lidských rukou, druhý na pohybu křídel u modelového organismu Drosophila melanogaster (octomilka obecná).

Mnoho typů třesu, včetně fyziologického třesu (PT) a esenciálního tremoru (ET), se vyskytuje v končetinách po obou stranách těla, s podobnou základní frekvencí kmitání. To naznačuje, že kontralaterální třesy mohou mít společný zdroj nebo jsou jinak spojené. Ve své studii jsem prozkoumala vazbu mezi třesem levé a pravé ruky. Pomocí 3D-akcelerometrů jsem změřila časový průběh třesu, a použila stacionární i nestacionární (waveletové) výpočetní metody k vyhodnocení bilaterální koherence. Měření na všech třech prostorových osách umožnilo prozkoumat ucelenější sadu kinematických proměnných, než ve většině předešlých studií. Nestacionární analýza usnadnila identifikaci časově transientní koherence, což je scénář, který se v analýze třesu dříve nebral v úvahu. U většiny subjektů s PT a ET byla nalezena statisticky významná bilaterální koherence v kmitočtovém pásmu 1-10 Hz. U obou typů třesu se krátké několika vteřinové úseky se silnou koherencí střídaly s intervaly statisticky nevýznamné koherence. K prozkoumání vlivu balistokardiackého impulsu společného pro obě ruce jsem měřila zrychlení hrudní stěny současně se zrychlením obou rukou a odhadovala částečnou koherenci nezávislou na pohybu hrudníku. Výsledky této analýzy ukazují, že bilaterální koherence u PT na hlavní frekvenci třesu (tj. v rozsahu 6-12 Hz) vyplývá ze spojení oscilace rukou s balistokardiackým silovým působením. Toto zjištění se neomezovalo pouze na klidový třes, ale platilo i pro posturální třes v obou zkoumaných polohách rukou.

Ve druhé části své práce jsem studovala modulární řízení pohybu křídel octomilky obecné Drosophila melanogaster. Modulární ovládání pohybu předpokládá, že komplexního

motorického chování lze dosáhnout kombinací malého počtu jednodušších motorických vzorců. Cílem bylo zjistit, zda lze pohyb křídla při různých letových manévrech rozložit do malého počtu navzájem nezávislých kinematických vzorců. Měřila jsem pohyb křídel upoutaných octomilek během delších intervalů nepřerušovaného letu (~ 60 sekund) pomocí vysokorychlostního počítačového kamerového systému. Za použití nové varianty analýzy nezávislých komponent (ICA), jsem rozložila složený pohyb obou křídel na složky, které mají minimální vzájemnou informaci (což je míra statistické závislosti). Za použití této metody jsem identifikovala čtyři typy kinematických vzorců, které mohou být aktivovány nezávisle na sobě, a vyskytují se jak v izolaci, tak v lineární superpozici. Tři z těchto nalezených základních vzorců lze asociovat s řízením vybočení, náklonu těla, a letového výkonu. Čtvrtý kinematický vzorec se skládá ze změny amplitudy kmitu s periodou 2 cyklů mávnutí křídel, přičemž tento vzorec trvá až několik desítek cyklů. Tento vzorec pohybu je nově identifikován a značí velmi rychlé řízení, na časové škále jediného mávnutí křídel (5 ms); proto jsem tento pohybový vzorec zkoumala podrobněji. U octomilky reagují v rámci jediného mávnutí křídel pouze tzv. kyvadélka (gyroskopický mechanosenzorický orgán). K prozkoumání role kyvadélek při aktivaci tohoto rytmického vzorce pohybu jsem studovala mouchy, u nichž byla obě kyvadélka ablatována.. V souladu s očekáváním měla chybějící zpětná vazba kyvadélek významný vliv: i. periodicita se zvýšila z 2 cyklů na 3-4 cykly, ii. vytvořila se slabá korelace mezi maximálním ventrálním zdvihem křídel a jeho načasováním v daném cyklu mávnutí.

Na závěr bych ráda shrnula, že moje práce předkládá dva základní nálezy týkající se neuro-svalového řízení rytmických pohybů: 1) třes levé a pravé ruky u PT a ET jsou přerušovaně synchronizované. Tato přechodná ale opakovaná synchronicita ukazuje slabé propojení třesu na obou rukách. I když koherence na hlavní třesové frekvenci PT může být vysvětlena simultánním balistokardiackým působením na obě paže, bilaterální koherence pozorována u ET, podobně jako nízkofrekvenční koherence u PT, můžou být spíše založené na přímém propojení mezi neuronálními generátory třesu levé a pravé ruky. Pro stanovení těchto mechanismů je ale zapotřebí provést další studie založené na kombinaci kinematických a elektrofyziologických nahrávek. 2) Komplexní kinematické vzorce pohybu křídel během hmyzího letu jsou generovány jako lineární kombinace několika základních kinematických vzorců, které jsou řízeny nezávisle na sobě. Tento nález přináší silnou podporu pro přítomnost modulárního řízení rytmických pohybů u bezobratlých.

Abstract

Rhythmic motions, regular or irregular, are an integral part of motor behavior both in health and in disease. Better understanding of its neural control mechanisms helps in developing methods for controlling the progression of diseases manifesting as rhythmic motions. I studied two specific aspects of rhythmic motions: bilateral coordination of hand tremors in human subjects and modular control of locomotion in invertebrates.

Many types of tremors, including the physiological tremor (PT) and the essential tremor (ET) occur in limbs on both the sides of the body, with similar fundamental frequency of the oscillation. This raises the possibility that the contralateral tremors may have a common source or are otherwise coupled. However, while significant contralateral interaction is seen in these two types of tremors, only limited evidence of bilateral coherence has been shown in the previous literature. Therefore, in my study I explored the existence of a weak coupling between the left and right oscillators the may lead to intermittent bilateral coherence. I measured triaxial acceleration of the two hands and systematically assessed their bilateral coherence, using both stationary and non-stationary (wavelet-based) analyses methods. Measuring all three axes allowed examination of a more complete set of kinematic variables than in most previous studies. The majority of both PT and ET subjects displayed significant bilateral coherence in the frequency range 1-10 Hz. In both the cases short epochs of several seconds with strong coherence were separated by intervals of insignificant coherence. To probe the contribution of the cardiac impulse that is common to both the hands, I measured the acceleration of the chest wall simultaneously with that of the two hands and estimated their partial coherence subject to the chest motion. Results indicate that in PT, bilateral coherence at the main tremor frequency (i.e. in the range 6-12 Hz) arises from a joint coupling of the hand oscillations to ballistocardiac forcing.

In the second part of my work I studied modular control of locomotion in the invertebrate model organisms for neuromotor control, the fruit fly *Drosophila melanogaster*. Modular motor control implies that a particular group of muscles is simultaneously activated to generate a specific motor pattern. The aim was to investigate if the various flight maneuvers

arise from the activation of a small number of independent neuromuscular control modes. I measured the wing motion of tethered flying fruit flies for long uninterrupted flight durations (~60 seconds) with a high-speed computer vision system. With a novel method based on the least-dependent component analysis I decomposed the joint motion pattern of both wings into components that have the minimal mutual information (a measure of statistical dependence). Using this method I identified four types of kinematic patterns that can be activated mutually independently, and occur both in isolation and in linear superposition. Three of the identified elementary patterns can be associated with body yaw control, body pitch control, and control of flight power. The fourth kinematic pattern consists of an alteration of stroke amplitude with a period of 2 wingbeat cycles, extending for dozens of cycles. This kinematic pattern is novel and interesting, as its features indicate the activity of a control system that operates at the times scale of a single cycle; Hence, I studied it in some details.

In conclusion, my study has put forth two major findings regarding the neuromuscular control of rhythmic motor activities: i. The hand tremor in PT and ET are intermittently synchronized. Such transient but recurring synchrony indicate a weak coupling between the tremors of the two hands. Although the coherence at the main tremor frequency can be explained by the simultaneous cardioballistic forcing, the origin of the low frequency bilateral coherence (i.e. 1-6Hz) needs to be explored. ii. Complex kinematic patterns during insect flight can be generated from linear combinations of elementary kinematic patterns that are controlled mutually independently. This provides strong evidence for the presence of modular motor control of rhythmic motion in invertebrates.

Contents

I. Introduction

1. Literature review: Rhythmic activities and motor control

1.1 Overview **2**

1.2 Genesis and modulation of rhythmic motor patterns **4**
1.2.1 Generation of steady central oscillations
1.2.2 Modulations of central oscillations by peripheral feedback

1.3 Involuntary rhythmic motion: Tremor **10**
1.3.1 Brief overview of the vertebrate neuromotor system
1.3.2 Neurophysiology of physiological tremor
1.3.3 Neurophysiology of essential tremor

1.4 Voluntary rhythmic motion: Wing beat of tethered flying fruit flies **22**
1.4.1 Motor primitives and modularity of motor control
1.4.2 Insect flight: a model system for motor control
1.4.3 Neuromuscular basis of wing motion
1.4.4 Stroke-by-stroke wingbeat control and the role of halteres

1.5 Kinematic data analysis **34**
1.5.1 Important kinematic parameters of hand motion and their significance in characterizing tremors
1.5.2 Important kinematic parameters of the fly wingbeat and their aerodynamic significance

2. Research hypotheses and objectives

2.1 Topics and motivation **43**
2.1.1 Extent of bilateral coupling in physiological and essential tremors
2.1.2 Modular control of complex wing stroke variations in fruit flies

2.2 Hypothesis **44**

2.3 Objectives **45**
2.3.1 Analysis of human hand motion
2.3.2 Analysis of *Drosophila* wing motion

II. Materials and methods

3. Experimental Methods

3.1 Overview **47**

3.2 Measuring hand tremor **48**
3.2.1 Subjects
3.2.2 Experimental procedure and data preprocessing

3.3 Measuring wing kinematics of tethered flying fruit flies **52**
3.3.1 Fly rearing and preparations
3.3.2 Experimental procedure and data preprocessing

4. Computational Methods

4.1 Overview **55**

4.2 Spectral density **56**
4.2.1 Statistical estimators and significance of the estimate
4.2.2 Time scales of variations in stroke parameters and Wiener entropy
4.2.3 Frequency spread of hand tremor and estimation of tremor amplitude

4.3 Coherence **62**
4.3.1 Statistical estimators and significance of the estimate
4.3.2 Bilateral coherence of left and right hand acceleration
4.3.3 Partial coherence between left and right hand acceleration

4.4 Wavelet spectral density **69**
4.4.1 Statistical estimator and significance of the estimate
4.4.2 Identification of intervals of *Drosophila* wing motion with subharmonic ventral amplitude variations

4.5 Wavelet coherence **74**
4.5.1 Statistical estimator and significance of the estimate
4.5.2 Identification of transiently occurring coupling between hand acceleration

4.6 Independent component analysis **79**
4.6.1 The ICA model and the MILCA algorithm
4.6.2 Least-dependent kinematic patterns of *Drosophila* wing motion

III. Results and discussion

5. Intermittent bilateral coherence in physiological and essential tremor

5.1 Overview **88**

5.2 Results **89**

5.2.1 Tremor amplitude and spectral content
5.2.2 Bilateral coherence of wrist kinematics
5.2.3 Intermittent character of bilateral coherence
5.2.4 Dependence of bilateral coherence on the ballistocardiac forcing in healthy subjects

5.3 Discussion **99**

5.3.1 Bilaterally coherent tremor is not limited to the resting hand position
5.3.2 Strong dependence of bilateral coherence on the axis of motion
5.3.3 Ballistocardiac forcing contributes to the bilateral coherence of physiological tremor
5.3.4 Possible mechanisms of the observed bilateral coherence

6. Modular control of wing kinematics of the fruit fly *Drosophila melanogaster*

6.1 Overview **106**

6.2 Results I: Independently controlled wing stroke patterns **107**

6.2.1 Events with distinct time courses are separated into distinct least-dependent components
6.2.2 The least-dependent components are statistically nearly independent
6.2.3 Statistical analysis allows to decompose complex stroke trajectories into elementary kinematic patterns
6.2.4 Classification of frequently obtained least-dependent kinematic patterns

6.3 Results II: Kinematic pattern controlled at the time scale of a single wing stroke **122**

6.3.1 Overall kinematic parameters
6.3.2 Characterizing the recurring single cycle stroke deformations
6.3.3 Effect of haltere ablation on the chosen kinematic pattern

6.4 Discussion **132**

6.4.1 Least-dependent component analysis as a tool for identifying independently controlled kinematic patterns

6.4.2 Classification of the least-dependent kinematic patterns and implications for flight control

6.4.3 Physiologic explanation for the periodic single cycle ventral amplitude jumps

6.4.4 Change in recurrence rate of the ventral amplitude jumps in absence of haltere feedback

IV. Conclusion **144**

V. Summary **145**

VI. List of publications **148**

List of abbreviations

Glossary of selected terms used in chapter 6

Bibliography

I. Introduction

CHAPTER 1

Literature review: Rhythmic activities and motor control

1.1 Overview

Motor control is traditionally classified into discrete movements and rhythmic movements (Schaal et al. 2004; Hogan and Sternad 2007; Degallier and Ijspeert 2010). Discrete movements, such as reaching, grasping etc., are preceded and succeeded by posture[1] and occupy a non-negligible duration containing no posture (Hogan and Sternad 2007). On the other hand, rhythmic movements as a class comprise of a wide variety of actions, ranging from the ongoing periodic ones like the heartbeat to episodic repetitive movements like drumming (Marder and Calabrese 1996; Hogan and Sternad 2007). The primary condition for any movement to be classified as rhythmic is that some aspect of it is repeated (Hogan and Sternad 2007).

Rhythmic motions are particularly interesting as their inherent repetition make it easy to quantify the motion as well as variability under different perturbed conditions. It is the most common mode of locomotion in the animal kingdom and has developed some of the fastest yet precise sensorimotor systems. Being phylogenetically the older motor behavior, it is found ubiquitously in the animal kingdom; providing the opportunity to study the evolution of a given motor pattern with increasing structural complexities (Katz 2016). Hence, understanding the genesis and the underlying dynamics of these rhythmic motor patterns leads to a better understanding of the neural control mechanisms crucial in health and in disease.

[1] A bodily configuration defined by a period of no movement (Hogan and Sternad, 2007)

This chapter provides an overview of the existing literature on motor control of rhythmic movements. In the second section I summarize the various types of neural mechanisms that are known to be involved in the generation and modulation of rhythmic motion in animals. In the third and the fourth sections I discuss the genesis of the involuntary and the voluntary types of rhythmic motor behaviors with reference to the specific systems that I have studied viz. the human hand tremor and the drosophila flight apparatus. In the last section of this chapter I discuss the significance of kinematic data analysis.

1.2 Genesis and modulation of rhythmic motor patterns

Oscillations in motor activity arise from a combination of central and peripheral mechanisms (Marder and Calabrese 1996; Marder and Bucher 2001). The motor control of rhythmic movements usually constitute of generating a stable central oscillation that is then modulated by the activity of peripheral sensory feedback loops (Kiehn 2016) and by fluctuations due to inherent noise in the neuromuscular system (Faisal et al. 2008). Steady central oscillations in motor activities can be generated by a number of mechanisms, discussed in subsection 1.2.1. Generic peripheral mechanisms that transform these steady oscillations into adaptive motor control are discussed in the second subsection.

1.2.1 Generation of steady central oscillations

Central pattern generators

Central pattern generators (CPG) are neural networks that are capable of generating rhythmic outputs even when stimulated with a non-periodic input. The concept of such neural networks was first put forth in the beginning of the 20th century by T. Graham Brown (Brown 1911) to explain the alternate flexion and extension of the leg muscles during vertebrate walking. This came as an alternative to the then prevalent hypothesis of rhythmic motion generation by chain of reflex actions. But, to identify a part of the nervous system that can on its own generate periodic signal it is necessary to isolate the prospective neural circuit from all feedback loops; something that is extremely difficult to achieve *in vivo* in higher animals. Such neural circuits were finally identified in invertebrate model organisms, the Arthropods (Mulloney and Smarandache 2010) decades after its proposition. Two independent research groups working on crayfish (Hughes and Wiersma 1960) and the desert locust (Wilson 1961, 1966; Wilson and Wyman 1965) identified neural circuits those could intrinsically generate the rhythmic activity necessary for the

coordinated movement of the locomotor organs (swimmerets and wings respectively). In vertebrates such CPGs are mostly located in the spinal cord. Descending neural pathways control the pace of such circuits by modulating the concentration of certain neuromodulators that are essential for the CPGs to sustain their rhythmic activity (Grillner et al. 1991; Cazalets et al. 1992; Ryckebusch and Laurent 1993).

Functioning principles of CPGs have been studied for decades in both vertebrate and invertebrate systems; albeit the latter played a pivotal role due to their less complex construct. In both systems, neural CPGs mostly constitute of a network of interneurons that centrally orchestrate the motor neurons. A number of cellular organization models, especially underlying vertebrate locomotion, have been proposed over the years (Guertin 2009). The simplest one called the "half center model" claims that the cyclic contraction-relaxation pattern of each pair of flexor and extensor muscles of a limb is achieved by reciprocally inhibited electrical activity of two distinct modules of the spinal CPGs, with one module („half-center") controlling the flexor muscle and the other the extensors. This claim has recently received experimental support, wherein trans-synaptic labeling of flexor and extensor motor neurons has revealed medio-lateral spatial segregation of the premotor neurons (Tripodi et al. 2011). However, patterns of locomotor activities, such as backwards walking, climbing etc., are often much more complex and cannot be explained by simple alterations of the flexor-extensor activity. Hence, many other models that incorporate these complexities have been proposed (Guertin 2009). The detailed neural organization of the CPGs and their activation patterns however differ in each species and as per the requirement of the concerned rhythmic motion (Katz 2016).

Although motor neurons are often not involved in the intermuscular coordinating rhythm generation, their conditional intrinsic membrane properties never the less shape the final rhythmic output (Dicaprio 1997; Kiehn and Eken 1997; Kiehn et al. 2000). In neonatal rats the NMDA induced rhythmic activity of individual spinal motor neurons synchronize via gap junctions into a coordinated output of the motor neuron pool without any spike activity in the CPG (Tresch and Kiehn 2000). This synchronization was local, i.e. limited to the motor pools of each ventral root. The coordination between the motor pools of different ventral roots along the spine still required the activity of the CPG networks. However, Tresch and his colleagues showed that the frequencies of these rhythmic patterns decrease from the

rostral to the caudal segments in the lumbar region of the spine. Hence, they proposed that the ubiquitous rostrocaudal gradient of rhythmicity seen in spinal CPGs might have resulted in part from properties of motor neuron pools, rather than exclusively from the properties of CPGs. Yet, in some other cases the motor neurons directly participate in the rhythm generating mechanisms of the connected CPG (Staras et al. 1998).

Myogenic rhythm generators

A second mechanism of rhythmic motor pattern generation involves intrinsic periodic contractions of the muscles in the absence of any periodic neural stimulation. In vertebrates such spontaneous rhythmic contractions are found to occur mostly in the smooth muscles, although such phenomena are also seen in skeletal muscle to some extent (Okamura and Ishiwata 1988). An example, seen in all vertebrates, is the contraction of the heart muscles. In this process specialized cardiac muscle cells called the pacemaker cells periodically generate spontaneous electrical impulses (Schuessler et al. 1996); these impulses then propagate through other cardiac muscles making the atria and the ventricles contract rhythmically. The mechanism of spontaneous impulse generation in these kinds of myogenic pacemaker cells is attributed to their unstable resting membrane potentials. Dynamics of the sodium, potassium and calcium ion channels are such that the membrane potentials oscillate between depolarization and repolarization, reaching the depolarization threshold in every cycle. Each time the depolarization threshold is reached the myocytes contract, hence resulting in rhythmic muscle activation. Another essential rhythmic movement with similar generation mechanism is the uterine contractions in mammals (Maul et al. 2003). However, spontaneous oscillations of the skeletal muscles originate from the properties of the contractile proteins, and hence the mechanism is very different from that discussed above. They are stretch activated and do not possess any pacemaker cells. This mechanism is discussed in some details in the next paragraph, for further details at the molecular level refer to (Ishiwata et al. 2011).

Although myogenic heart beat and intestinal pulsation have also been shown to exist in insects (Sláma and Lukáš 2011; Sláma 2012), but unlike vertebrates myogenically generated rhythmic movements are very often an integral part of locomotion in invertebrates. In many flying insects the basic oscillatory motion of the wing is brought about by the contraction of large flight muscles in the thorax that is transmitted to the

surrounding exoskeleton and to the base of the insect wings (Dudley 2002). These flight muscles have been shown to perform oscillatory contractions that are uncoupled from the activation rate of their motor neurons (Dickinson and Tu 1997). The basis of these spontaneous oscillations lies in the properties of the contractile protein system that incurs a delayed change in muscle tension in response to changes in muscle length (Ruegg et al. 1970; Abbott and Cage 1984). Similar fundamental mechanisms are thought to underlie the spontaneous oscillations of the vertebrate skeletal muscles under certain activity regimes (Ruegg et al. 1970).

Other mechanisms of rhythmic motor pattern generation

In addition to the two generic rhythmic pattern generators i.e., the CPGs and the myogenic pacemakers, oscillatory motor patterns may also arise from different specific mechanisms. The simplest ones are where the oscillatory motions arise from just the mechanical forces acting on the limb at the joint. While in more complicated cases, like that of the seemingly simple rhythmic motor act of spontaneous eye blink, only two muscles[2] are thought to be controlled by multiple premotor structures in the brainstem (Bour et al. 2000). Many a times the source of rhythmic movements may not be a single anatomical structure, but a system constituting of body parts, their inter-connections and various sensorimotor loops. Examples of such rhythmic motions are the voluntarily generated ones, like the hand movements of a skilled musician while playing a musical instrument. The geneses of such rhythmic motions are pretty complex, requiring precise timing of several hierarchically organized actions depending on the specific instrument (Zatorre et al. 2007).

All the mechanisms of rhythmic motor pattern generation discussed above, although found in healthy motor systems are also shared by the spontaneous oscillatory motions accompanying movement disorders. While abnormal oscillatory activities in the central nervous system have been associated with some kinds of tremors in the periphery(Elble 1996) e.g. Parkinson's disease tremor and essential tremor, it is not the case for most kinds of tremors. Infact a large group of tremors are thought to originate due to the synchronization of motor units by reflex activation or unstable sensorimotor loops (Deuschl et al. 2001). Genesis and other characterizing properties of the two types of tremors that I

[2] orbicularis oculi and levator palpebrae superioris

have studied, i.e. physiological tremor and essential tremor are discussed in subsections 1.3.1 and 1.3.2 respectively.

1.2.2 Modulations of central oscillations by peripheral feedbacks

The hypothesis of chain of reflex actions generating rhythmic motion prevailed for decades in the literature essentially because it was well recognized that the loss of normal peripheral feedback disrupts rhythmic behavior. Although now this hypothesis has given way to the intrinsic rhythmic pattern generators, the importance of peripheral feedback in orchestrating rhythmic motions remains unchallenged across species. Infact, periodic forcing of the peripheral feedback systems is often seen to entrain the rhythmic pattern generators in invertebrates (Bartussek et al. 2013) as well as in vertebrates (2003). It is seen that in the absence of the mechanosensory feedback from their hind wings the dipteran flies cannot sustain free flight and swirl down to the ground within a few wing beats (Derham 1720). Similar reports of losing balance while trying to walk is reported by patients with sensory peripheral neuropathy, a neurodegenerative disease in which the sensory nerves are damaged (Mold et al. 2004).

This instigates an important question: given the rhythmic pattern generator's intrinsic ability to generate the rhythmic motion, what prevents an organism from sustaining it without sensory feedback? The answer lies in the factors that perturb the state of the system in rhythmic motion. Stable continuous movement in any environment heavily relies on how efficiently the moving system reacts to various perturbations (Dickinson et al. 2000; Hausdorff et al. 2001). A suite of sensorimotor loops measure the magnitudes and dynamics of force and length changes in the musculoskeletal system and actuate specific adaptations for undesired changes (Haridas et al. 2005; Mazzaro et al. 2005; Ristroph et al. 2010, 2013). In case of locomotion, perturbations range from various internal factors like the cardiac activities, sensory feedback delay etc. to environmental factors like varying resistance of the medium or obstacles in the path. Maintaining postural equilibrium in the face of all these perturbations as well as during self-initiated movements involves coordination of sensorimotor strategies to stabilize the body's center of mass (Horak 2006). From walking bipeds to flying insects, at least as many types of stabilizing sensorimotor systems exist in the animal world as the fascinating forms of locomotion (Dickinson et al. 2000).

In all the sensorimotor systems the once responsible for dynamic stabilization heavily rely on mechanosensors. Mechanosensors are cellular structures innervated by sensory neurons that respond to mechanical stress or strain of the concerned structure. The significance of mechanosensory feedback is increased many folds because of their rapid phasic nature that enables them to control a rhythmic motor pattern on a cycle-by-cycle basis (Dickinson et al. 2000). While acting within a single cycle is advantageous for any motor behavior, it is of supreme value in maintaining postural stability at the face of perturbations. Hence, not surprising that in most vertebrates the major contribution towards the sense of balance and spatial orientation is provided by mechanosensory feedback from the somatosensory and the vestibular systems (Peterka 2002). Even in the simpler invertebrate model organisms for neuromotor control, mechanosensory feedbacks play a crucial role in actuating stable locomotion. In fact in *C. elegans* the sinusoidal crawling motion is actuated by passing a chain of myotatic reflex along the body axis; i.e. the stretch receptors of one bending segment activates the motor neurons of the immediately posterior segment (Wen et al. 2012; Schafer 2015). However, in all the other studied organisms the mechanosensory feedback modulates the motor output of rhythm generators (Berger et al. 1984; Dietz et al. 1987; Fayyazuddin and Dickinson 1999; Elson and Berkowitz 2016)by either influencing the rhythm generator itself or by directly modifying the activation patterns of the actuator muscles. As in the case of the dipteran flies, wingbeat synchronous feedback from the mechanosensors on the wing and the modified hind wings act directly on the muscles actuating the wing motion by fine tuning its firing phase (Fayyazuddin and Dickinson 1999). However when these mechanosensors are stimulated by mechanically vibrating the fly body, periodic activation of the same actuator muscles entrains the core rhythm generator of the wing beat by mechanical forcing and modifies the wingbeat frequency (Bartussek et al. 2013). This feedback system is further elaborated in the context of my own study in section 1.4.2.

1.3 Involuntary rhythmic motion: Tremors

Rhythmic motions of the locomotory organs enable the animals to successfully move through its environment, yet when it occurs spontaneously may interfere with the basic functionality of the organ. In humans the most common adult movement disorder is the involuntary shaking of the limbs and other body parts, called the tremors (Louis et al., 1998). Although more evident during diseased states, tremors are also present in neurologically healthy subjects, known as physiological tremor. Tremors are an unavoidable byproduct of the central to peripheral cascade of motor control. Many factors like motor pathways modulated by the upstream oscillatory activities in the motor cortex, synchronized firing of motor units etc., are also characteristics of a healthy neuromuscular system. Physiological tremor as a motor activity is interesting in itself, as it involves certain parts of the central nervous system and pathways that are also found to be active during pathological forms of tremors. Hence, it provides a window to study the healthy state of certain parts of the neuromuscular system that also play a role in the pathological tremorogenesis. This is particularly valuable for human investigations because of the limited direct experimental access to various parts of the central nervous system.

Pathological tremors almost always appear as a symptom of one of the several neurological disorders. Tremulous motions, more often than not, have a multifactorial genesis. The complexity of tremorogenesis is such that even after decades of research, anatomical origins and pathophysiologic mechanisms underlying even the most common types of tremors are still unknown (Elble, 2013b). While some kinds of tremors are thought to arise from a distorted form of the same mechanism that underlies physiological tremor, most of the others such as Parkinsonian tremor, orthostatic tremor etc., are believed to arise from a newly developed diseased state of the motor control system. The present state of tremor pharmacology has been nicely summarized in the recent review by Elble (Elble, 2013b), where one of his key points reads "*There is no form of pathologic tremor for which the anatomic origin and pathophysiology of tremorogenic oscillation are understood enough to*

accurately guide the development of a successful pharmacotherapeutic treatment". Hence, studies of different forms of tremors that shed light on the possible mechanisms of tremor genesis have vital roles to play in the future development of tremor pharmacology.

1.3.1 Brief overview of the vertebrate neuromotor system

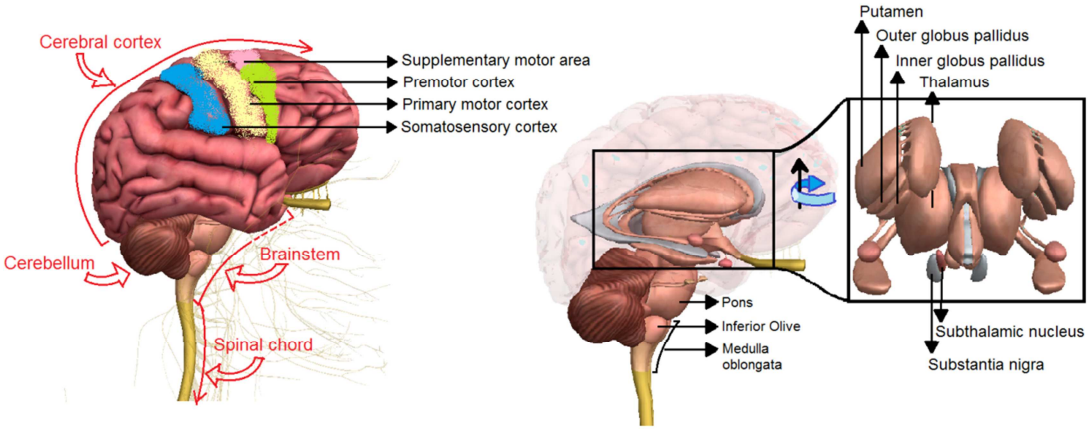

Figure 1.1: Cartoon diagram of the human brain showing the key parts of the motor pathway. Diagrams prepared using free version of the zygotebody web application and are based on the available information in literature (e.g. Jacobson and Marcus, 2008; Pierrot-Desseilligny and Burke, 2005; Rosenbaum, 2010).

In vertebrates the generation of any movement, be it voluntary or involuntary, involves several hierarchical levels of neuromuscular control. The primary motor cortex in the frontal lobe is the prime site involved in the production of movements, while other areas such as the basal ganglia, the cerebellum, etc. are responsible for higher order control of motor function. Figure 1.1 shows the parts of the central nervous system which are known to play key roles in motor pattern generation and control. Involuntary motions such as reflex actions on the other hand can be generated locally, completely controlled by the spinal cord (Fig. 1.2). Reflex actions are the simplest form of motor behavior generated in response to a stimulus. Any kind of voluntary movement or external stimulus elicits mechanical feedbacks from the muscles as well as the skin; which shows up as a series of electromyographic (EMG) bursts of the concerned muscles. In humans the short-latency stretch reflex occurring 20-50 ms after the muscle stretch (Pruszynski et al., 2011) is widely agreed to originate from the monosynaptic activation of the alpha motor neurons by the Ia-group of afferents at the spinal cord (Fig. 1.2). These sensory fibers from the muscle

spindles can detect even very small amplitude oscillations (Hagbarth and Young, 1979). However polysynaptic reflex loops are more common, i.e. in most other cases the afferent-to-efferent connections are via one or more interneurons (as seen in case of Ib afferent in Fig. 1.2). EMG response due to the sensory feedbacks from the skin and/or subcutaneous tissues have longer latencies of 50-105 ms (Corden et al., 2000; Darton et al., 1985; Pruszynski et al., 2011). Unlike the short-latency stretch reflex, these are thought to have more complicated neural pathways (Pruszynski et al., 2011) with possible supraspinal interventions (Kimura et al., 2006; Shemmell et al., 2009). Finally, the ultimate unit of the motor control pathway is the "motor unit". A motor unit comprises of a motor neuron and skeletal muscle fibers innervated by its axon terminals. In vertebrates the strength of a muscle contraction depends on the number of motor units activated[3]. Anatomical details and the functionality of these different components of the motor pathway can be found in neuroscience text books (such as: Jacobson and Marcus, 2008; Pierrot-Desseilligny and Burke, 2005; Rosenbaum, 2010). As my PhD research concerns only tremors, in this thesis I would discuss only those centers of the motor pathway that are known (or thought) to be involved in tremorogenesis.

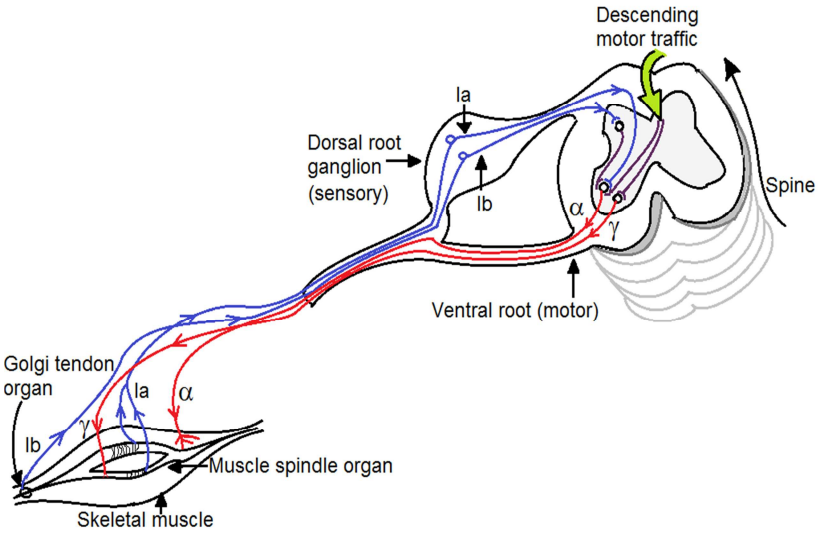

Figure 1.2: Basic circuitry of muscle proprioception in human. Afferent neurons (blue) sense changes of muscle length (Ia) or tension (Ib) and form direct (not via brain) connections with the motor neurons (red) that initiate muscle contraction (α). Supraspinal signals change the loop gain via γ-motor neurons. Diagram modified and redrawn from (Fig. 3.6, Rosenbaum, 2010)

Our understanding of the tremor neurophysiologies, even for the most common and widely studied ones, is far from complete (Elble, 1996; Elble, 2013b; Hallett, 2014). However, decades of scientific research have led to our understanding of specific parts of the

[3] In invertebrates the extent of muscle contraction is regulated by the balance between the excitatory and the inhibitory signals of the innervating motor neurons.

neuromotor system that are involved in tremorogenesis. In the next two subsections I discuss the neurophysiologies of such components in the cases of the two types of tremors that I have studied viz. the physiological and the essential tremor.

1.3.2 Neurophysiology of the physiological tremor

Physiological tremor is believed to have a multifactorial origin with central as well as peripheral sources. (McAuley and Marsden 2000) list a number of early experiments and their proposed mechanisms of oscillatory muscle activities. These proposed mechanisms were broadly classified under the following headings (reordered): i. mechanical resonance, ii. motor unit firing properties, iii. synchronization by reflex loops, iv. synchronization by CNS oscillators, v. intrinsic muscle property (e.g. resonance of contractile system, actomyosin cross-bridge cycling). The present consensus is that the physiological tremor arises from a concoction of all these five mechanisms, with differential contribution of each under different conditions (McAuley and Marsden 2000; Deuschl et al. 2001; Lakie et al. 2012). In the rest of this subsection I will discuss how each of these proposed mechanisms aid to muscle oscillations and may therefore contribute to tremulous motions in neurologically healthy subjects.

Mechanical resonance

The simplest and so far the most widely accepted of all the proposed sources of physiological tremor, is the mechanical resonance of the oscillating limbs. This phenomenon is a result of the basic physics governing the motion of an object about its pivot. For example, in the most simplistic model a hand outstretched from the wrist joint can be considered to act as a torsional pendulum. Such systems tend to oscillate with a natural frequency that in this case varies directly with the muscle tone and inversely with the inertia of the oscillating limb (Lakie et al. 1986). The limb in any posture is supported by tonically active effector muscles; the broadband EMG activities of these muscles always have a component at the natural frequency of the limb that sets it in a resonant oscillation. Understandably this resonance frequency is different for different parts of the body (Deuschl et al. 2001): finger about the metacarpophalangeal joint ~25 HZ, hand about the wrist joint 6-8 Hz, lower arm and hand about the elbow joint 3-4 Hz and the whole arm about the shoulder joint 0.5-2 Hz. As physiological tremor has about the same frequency

range in all the body parts (Morrison and Newell 1999; McAuley and Marsden 2000), it seems that only for the hand-wrist system mechanical resonance can contribute to physiological tremor. For the mechanical resonance of the more proximal body parts to contribute to the physiological tremor the muscle tone has to increase.

In addition to the muscle activities a factor that has been long recognized to impart oscillations via mechanical resonance is the ballistocardiac impulse. Each cycle of ejection of blood into the aorta is associated with a reaction force that acts on the body – the central ballistocardiac impulse. This impulsive force instigates mechanical oscillations in the extremities at their respective natural frequencies (mentioned in previous paragraph) and the effect is seen more strongly when the limb is in rest. Additional peripheral ballistocardiac impulses are also known to arise from blood pressure oscillations in the limbs. In terrestrial conditions measuring the ballistocardiac force is limited to a unidirectional recording of the recoil force of the body along the head-to-toe direction. However, under microgravity conditions (i.e. close to zero gravity) as the subject is decoupled from the environment, measurements using impedance plethysmography[4] reveal that the cardiac impulse generate about $0.04ms^{-2}$ of acceleration along the dorso-ventral axis in addition to about $0.07ms^{-2}$ along the expected vertical axis (i.e. head-to-toe direction) (Prisk et al. 2001). The role of ballistocardiac force in tremor genesis has long been recognized, and a number of older studies (Brumlik 1962; Van Buskirk and Fink 1962; Wachs 1964; Yap and Boshes 1967) even proposed it to be the principal origin of physiological tremor. It has been shown that the vibration of relaxed hands is indeed due mainly to ballistocardiac forces (Yap and Boshes 1967), and that the peripheral blood pressure oscillations have a significant effect on the amplitude of postural PT (Morrison et al. 2013).

Motor unit firing properties

Any movement of the limb is always associated with the activation of the motor units, i.e. the activation of a motor neuron that in turn activates the innervated muscles. Most motor neurons receive input from several sources at the spinal cord (Fig. 1.2) and exhibit a wide range of firing activities with a lower bound in the 6-10 Hz frequency range when active

[4] A non-invasive medical test that reflects blood volume changes by measuring small changes in electrical resistance of the chest, calf or other regions of the body.

(McAuley and Marsden 2000; Farina et al. 2014). However, each muscle is innervated by a pool of motor neurons and the overall activity of this pool (neural drive) controls muscle activation. Hence, to decipher the mechanism of muscle force generation from motor unit firings properties it is necessary to understand the neural drive. In this regard two slightly different schools of thoughts exist (Farina and Negro 2015).

i. Motor unit synchronization: This is the older school of thought based on the observations that discharges of pairs of motor units are not independent but show a degree of correlation. The range of correlations seen between pairs of motor neurons are explained in terms of different possible kinds of synchronization in (McAuley and Marsden 2000). The hypothesis is that the common synaptic input delivered to the motor neuron at the spinal cord instigates correlated discharges of action potentials by the motor neuron pool (McAuley and Marsden 2000; Deuschl et al. 2001; Semmler 2002). Studies have shown that the physiological tremor and the EMG of the effector muscle activities are coherent in the frequency range of 8-12 Hz; even if the firing rates of the individual motor units have completely different fundamental frequencies (Elble and Randall 1976).

ii. Motor neuron pool as a filter tuned on common input: This school of thought is based on the hypothesis that above a certain frequency threshold the motor neuron pool transfers the common synaptic input to the output with high accuracy and cancels all other input components (Farina et al. 2014); The lower bound corresponds to the minimum discharge rate of the motor neurons, which is usually in the 6-10 Hz range (McAuley and Marsden 2000; Farina et al. 2014). As the neural drive to the muscles primarily comprise of the common input signal to the motor neuron pool, high coherence between the activities of pairs of motor units is implied.

(Farina and Negro 2015) provide a comprehensive review on the differences between the two proposed mechanisms by which the motor unit firing properties may encode the common drive.

Motor unit firing properties have always received special attention in studies aimed to understand the neurophysiology of physiological tremor (McAuley and Marsden 2000; Deuschl et al. 2001). However, in the light of recent studies one may have to reevaluate the proposed modes of force generation by the high frequency components of the neural drive. (Negro et al. 2009) showed that during isometric contraction the contractile system of the muscles act as a low-pass filter of the neural drive in a bandwidth mainly below 5–6 Hz. This would imply that the muscle activities needed to generate sufficient forces for physiological tremor [6-12 Hz (Morrison and Newell 2000; Raethjen et al. 2000b)] would be significantly attenuated. However, there are clear evidences of high EEG-EMG coherences during pathologic tremors at frequencies greater than 6 Hz (Grosse et al. 2002; Muthuraman et al. 2013), indicating that the CNS neural activities in this frequency range are reliably transformed into motor unit activities. Negro and colleagues propose that low-frequency oscillatory inputs necessary for force control may be transmitted by a higher-frequency carrier (Farina et al. 2014).

Synchronization by reflex loops

Although the negative feedback functionality of these reflexes aims to dampen unwanted muscle activity, but due to their inherent latency (i.e. time gap between the muscle stretch and the feedback EMG response) a phenomenon called the 'feedback resonance' reinforces rhythmic activities at certain frequencies. For example, the loop time of spinal stretch reflexes at the finger is estimated to be about 50 ms (1978; McAuley and Marsden 2000). If the fingers are subjected to a 10-Hz stretch release cycle, by the time the reflex action tries to contract the stretching muscle it is already in the release phase of the contraction cycle. Hence, a delay of 50 ms would reinforce the tremor rather than oppose it. It is important to note that under normal circumstances (i.e. neurologically healthy individuals) even though the reflexes can support an ongoing tremor oscillation, it does not seem to be strong enough to produce substantial reflex compensation so as to cause tremor on its own (Prochazka and Trend 1988; Rothwell 1998). However, Prochazka and Trend showed that if the loop gain increases by even a small amount (10% for the elbow joint), the stretch reflex alone can give rise to periodic contractions of the effector muscles at frequencies of pathological tremors (i.e. 3-8 Hz) (Prochazka and Trend 1988).

Synchronization by CNS oscillators

Most controversial of all the proposed sources for physiological tremor till date is the presence of a central oscillator for the 8-12 Hz component of the oscillation. Oscillatory neural activities appear at various levels of the central nervous system and at least some of these are believed to propagate on to the kinematics of the extremities (Baker et al. 1999; Raethjen et al. 2002; Jerbi et al. 2007). As clearly demonstrated by human EEG and more detailed electrophysiological measurements on monkeys, the neural activities in the brain are strongly rhythmic in nature (Sanes and Donoghue 1993; Murthy and Fetz 1996; Arce-McShane et al. 2016). Soon after the discovery of the alpha rhythm of the cortical neural activities by Hans Berger, it was proposed to be a source of the physiological tremor based mainly on their frequency overlap (e.g. Schwab and Cobb, 1939). However, shortly followed studies showing that the tremor frequency and intensity remained unaffected by considerable changes in the alpha rhythm of the cortex, hence jeopardizing the proposition (e.g. Lindqvist, 1941). Surprisingly, even after decades of research this controversy still persists, as is demonstrated by these two recent studies (Vernooij et al. 2013; Mehta et al. 2014). The former clearly shows evidences to support that the central oscillators play a prime role in two of the major manifestations of physiological tremor, while the latter advocates for a dominant role of mechanical resonance in physiological tremor. A major factor that has till date aired this controversy of central versus peripheral dominance in physiological tremor genesis is the lack of a definitive central source, while evidences clearly demonstrate a crucial role played by a central drive to the motor units. One of the early evidences in stark support of central oscillators came from Marsden and colleagues who presented the case of a patient showing a clear 9.5 Hz tremor in his both arms, even though his right arm was totally deafferented surgically (Marsden et al. 1967). This indicates that physiological tremor not only exists, but also retains its characteristic frequency in complete absence of sensory feedback from the oscillating limbs. Further evidences come from studies that demonstrate that the synchronized activity of the motor units in the 10Hz frequency range is unaffected by factors that alter the mechanical properties of the limb, such as loading, changes in muscle stiffness or anesthesia (McAuley et al. 1997; Halliday et al. 1999). Some of the most direct evidences to the involvement of brain in physiological tremor genesis come from studies that report changes in tremor parameters in response to perturbations of different motor areas of the brain. Holmes and his colleagues in a series of studies on humans with accidental cerebellar lesions (Holmes 1917) showed that at least in some cases with severe damage the physiological tremor

seemed to be replaced by jerky movements. In a more recent study (Mehta et al. 2014) have shown that transcranial stimulation of the primary motor cortex and the cerebellum have modulating effects on physiological tremor and the effect is dependent on the type of tremor as well as the site of stimulation.

Intrinsic muscle properties

The contractile system of the striated muscles consists of thick filaments (with attached myosin motor proteins) and actin rich thin filaments, which are the key players in muscle force generation. According to the sliding filament theory, muscle contraction (and hence muscle force generation) is brought about by myosin forming a crossbridge with actin and in the process sliding the thick filament in-between two layers of the thin filaments. Hence, the maximum force developed in a skeletal muscle fiber is proportional to the overlap between the thick and the thin filaments (Gordon et al. 1966a, 1966b). This contractile system that enables stable contraction and extension of the skeletal muscle fibers (i.e. myofibrils), under specific conditions results in stretch activated spontaneous length oscillations (Ruegg et al. 1970), as in the case of the flight power muscles in dipteran flies discussed in section 1.4.3. Whether or not such spontaneous muscle oscillations have any significant contribution towards physiological tremor is unknown.

1.3.3 Neurophysiology of Essential tremor

Essential tremor is the most common movement disorder with a worldwide prevalence of 4.6% in the age group above 65 years (Louis and Ferreira, 2010). But despite dedicated efforts we are only beginning to understand its neurophysiology (Louis, 2005) and its very definition is still evolving (Elble, 2013a). Until recently essential tremor was considered to be a benign, familial, monosymptomatic disorder. Recent studies have unleashed a barrage of clinically heterogeneous symptoms related to essential tremor (ET), gradually leading to the belief that the clinical syndrome of essential tremor may actually represent a family of diseases (Elble, 2013a; Hallett, 2014; Louis, 2005). Although traditionally considered to be familial, recent studies reveal that only about 50% of ET patients have a family history of this disease (Whaley et al., 2007). On the other hand, some epidemiological studies have identified putative environmental factors (toxins such as β-carbonyl alkaloids and lead) that increase the risk of developing ET (Louis et al., 2002; Louis et al., 2003).

Essential tremor is characterized by a 4-12 Hz tremor predominantly seen in the upper limbs during postures maintained against gravity (postural tremor; see table 1.3, section 1.5.1) or during motion (action tremor). It is also sometimes seen in upper limbs while at rest (rest tremor). However, ET is also seen in other body parts such as the head (i.e. neck motion), voice, facial musculature, trunk and the lower limbs. Details of its diagnostic criteria can be found in (Louis, 2005). While until recently it was considered benign, it does interfere with daily activities such as writing, pouring, eating, driving etc. (Louis, 2005). As the tremor in ET is usually progressive, it results in increasing severity and interference in day-to-day activities with time. In more advanced cases, the disability is so severe that the patients are no longer able to feed or dress themselves. In an extensive study of community-dwelling ET patients, a large fraction (73%) reported disabilities in various functional domains (Louis et al., 2001). Further details of the clinical presentations and epidemiology of essential tremor can be found in the comprehensive reviews on this topic, such as (Louis, 2005; Louis and Ferreira, 2010).

Like all other types of tremors, the pathophysiology of ET is not well understood. In this case what makes the study of the neural pathways more complicated is its progressive nature. The gradual development of neurological symptoms such as mild gait ataxia and spreading of the tremors from hands to other body parts indicate that the underlying neuropathology spreads to more and more parts of the motor pathway with time. The onset of rest tremor in severe cases may also indicate involvement of basal ganglia in the pathogenesis. There are evidences that suggest that this disease could be neurodegenerative (Louis, 2009). In all, there is a general consensus in the field of movement disorder studies that ET is of central origin (Raethjen and Deuschl, 2012). In the rest of this subsection I will go into some details of the components of the central motor circuit that are believed to be associated with tremorogenesis in ET. For further details please refer to (Elble, 2013a; Hallett, 2014; Hellwig et al., 2001; Louis, 2005; Pinto et al., 2003; Raethjen and Deuschl, 2012).

Cerebellum

Although the cause of oscillation that manifests as the 4-12Hz essential tremor at the periphery is still unknown, the prime involvement of the cerebellum is unequivocally

agreed upon (Pinto et al. 2003; Louis 2005; Elble 2013b; Hallett 2014). At the first look, the fact that cerebellum is involved in the pathogenesis underlying ET is suggested by the symptom of gait ataxia, which is a classic signature of cerebellar dysfunction (Fasano et al. 2010). More direct indications for a critical involvement of the cerebellum in ET come from the fact that cerebellar lesions (Dupuis et al. 1989) or deep brain stimulation of the ventral intermediate (VIM) nucleus abolish tremor. VIM is the cerebellar recipient of the thalamic nucleus. In addition a study of the blood flow PET (positron emission tomography) showed cerebellar hyperactivity (as compared to neurologically healthy subjects) in ET patients even during rest position when the tremor was not visible; this hyperactivity further aggravated and was also seen in the red nucleus region during postural ET (Wills et al. 1994). Recent post mortem studies indicate significant structural changes in the cerebellar region of the ET brain as compared to that of age-matched control subjects (Louis et al. 2007; Louis 2010). The most prominent effect being an approximate 30–40% loss of Purkinje cells. However, it is important to note that all the studied ET patients died at ages older than 70 years, hence it is necessary to account for other aging effects in adding to the pathology of Purkinje cell loss (Elble 2013b).

Thalamus

Like the cerebellum, involvement of the thalamus in generating ET too has ample neurophysiological and clinical evidence. Hua and colleagues identified a group of bursting cells in the VIM nucleus of the thalamus that is active only when there is a visible tremor at the periphery. The neural activities of these cells have a clear dominance at the tremor frequency and are also significantly correlated with the muscle activities of the forearm during postural tremor (Hua 2004). Moreover, lesioning or high-frequency stimulation of the thalamic nuclei (VIM and Vop, i.e. ventral oralis posterior) are till date the most effective treatment provided to arrest the peripheral tremor manifestations in ET patients.

Inferior olive

The involvement of the inferior olive in ET tremorogenesis was originally proposed based on the results of rodent experiments with harmaline-induced tremor. Animals treated with harmaline (fluorescent psychoactive alkaloid of beta-carboline group) are seen to develop an action tremor in the frequency range between 7 and 12 Hz, similar to human essential tremor in many respects (Raethjen and Deuschl 2012). Harmaline is known to act by

increasing the strength of synchronization in the already spontaneously oscillating neural populations of the inferior olivary nucleus (Placantonakis et al. 2004; Raethjen and Deuschl 2012). However, there is no clear evidence to support that the mechanism of harmaline induced tremor in rodents is similar to that underlying human ET; other than the indirect evidence of slightly high beta-carboline level in the blood samples of ET patients as compared to age-matched neurologically healthy subjects (Louis et al. 2002).

The involvement of inferior olive dysfunction in pathophysiology of ET (olivocerebellar model of ET) is debatable. While an early PET study (Hallett and Dubinsky 1993) showed high glucose metabolism rate in the medulla (that harbors inferior olive) of ET patients, contrary results were obtained in a subsequent study (Wills et al. 1994). A detailed postmortem study of the microscopic changes in the inferior olivary nucleus of ET patients compared to age matched control subjects failed to detect any difference (Louis et al. 2013). Hence, the status of the olivocerebellar model of ET can be summarized as in (Louis et al. 2013): "*if the olive is involved in essential tremor, then there is no clearly identifiable structural or metabolic correlate*".

Motor cortex

A number of studies have reported activities in the motor cortex that are correlated with the effector muscles activities during essential tremor (Hellwig et al. 2001; Raethjen et al. 2007; Schnitzler et al. 2009). It is however important to note that both the cerebellum and thalamus that have reciprocal connections with the cortex are known to be involved in the pathophysiology of ET; cortical activities measured using EEG and MEG may therefore also imply tremor correlated changes in deeper brain areas. Till date there has been no direct evidence of the motor cortex generating the 4-12 Hz essential tremor rhythm.

1.4 Voluntary rhythmic motion: Wing beat of tethered flying fruit flies

Body dynamics that enable any animal to efficiently move through its environment are extremely complex. In animals with even the modest neuromuscular systems a number of control mechanisms provide the necessary drive, maneuverability, stability and adaptation to the environment. Although the control mechanisms are markedly different among different species and types of locomotion such as walking, flying and swimming; many dynamic features of the locomotor appendages are surprisingly similar (Dickinson et al. 2000). To begin with, in all animals the basic motion of the locomotor appendage or the body itself that leads to the forward propulsion is rhythmic in nature. This commonality seems to be intuitive, as one would expect that the simplest way to transport any physical being (in the absence of any perturbation) is to device a motor activity for efficient propulsion through the environment and then repeat the same. But interestingly, cross species similarities between the locomotor kinematic patterns extend way beyond just the rhythmicity. For example, the act of switching gaits[5] in order to move most efficiently at different speeds and under different behavioral conditions is a well-recognized trait of terrestrial locomotion, biped and quadruped alike (Goslow et al. 1981; Hong and Brueggemann 2000; Cham and Redfern 2002). Changes in body dynamics that can be considered equivalent to gait changes in terrestrial locomotion are seen also in aquatic animals under similar behavioral conditions; and with slightly loose analogy in flying animals (Dickinson et al. 2000). Similar or scalable kinematic features of the locomotor appendages across species allow specific aspects to be studied in organisms where the concerned feature may be exaggerated due to adaptation. Hence, like in many other fields, studying limb kinematics of model organisms plays a vital role in advancing our knowledge of the neuro-muscular control of locomotion in general.

[5] patterns of movement of the limbs

In my study I analyzed the wing motion of tethered, flying fruit flies. During tethered flight, the motion of the wings is unconstrained, while the body of the fly is fixated. The observed changes in wing kinematics are interpreted as attempted flight maneuvers or responses. This experimental paradigm is especially well suited to study the wing motion under perturbed conditions that hinder free flight, such as when the halteres (a critical flight appendage) are ablated.

1.4.1 Motor primitives and modularity of motor control

The hypothesis that complex motor behaviors can be generated by a small number of relatively simpler movements, called the motor primitives (a.k.a. motor schema, prototypes, control modulus), has grabbed much attention in the last few decades (Ghahramani 2000; Thoroughman and Shadmehr 2000; Hogan and Sternad 2012). Major interest in exploring motor primitives of different kinds of movements lies in the fact that it indicates reduction in the output dimensionality of the motor control system. While this information undoubtedly bears important implications for the neuromotor system concerned, it enormously simplifies the designing principles of the bio-inspired autonomous robots (Schaal 2006).

The term “motor primitives” describe a class of movement units at the behavioral level with no committed hypothesis for its neurophysiological genesis (Flash and Hochner 2005). Motor primitives can be expressed in terms of the kinematic or the dynamic variables of the motion or both. The idea is to understand the organizational principles of animal behavior without going into the nitty-gritty of complicated cascades of neuromuscular activities. For example, Fentress and Stilwell (Fentress and Stilwell 1973) identified 7 movement components, like flurry of forelimbs below face, wetting forepaws with tongue etc., that occur sequentially during the face grooming behavior in mice. In another study on hoverflies Geurten et al. (Geurten et al. 2010) classified 9 prototypical movements of the hoverfly body, such that any segment of free flight consists of a sequence of these typical movements. 8 out of the 9 prototypical movements involve body rotation and/or translation with respect to multiple body axes. In both these studies complex motor activities were perceived to be generated by stitching the motor primitives serially in time. Another way of articulating motor primitives into motor activities is to allow partial or

complete overlap in their time of occurrences. Mataric and colleagues (Mataric et al. 1999; Fod et al. 2002) as well as others (Sanger 2000) working on human hand movements identified motor primitives that could be used as the "basis set" for complicated hand movements. That is, any segment of the hand trajectory during a movement task can be derived from linear combinations of different subsets of the identified set of motor primitives. Similar conclusions have also been drawn from studies with more complicated tasks involving locomotion in humans (Ivanenko 2005).

It is important to keep in mind though, that individual motor primitives may be task or behavior specific i.e. they are not necessarily meant to be used for all behaviors or tasks by the organism. What is important is that these elementary movements can be combined in a well-defined manner to form a more complex movement.

In my study I explored the existence of elementary kinematic patterns in the wing motion of unstimulated tethered (section 3.3.1) flying flies. Although such kinematic patterns also fall under the broad definition of motor primitives, but a different terminology was used to emphasize two aspects: i. each component is not only a particular type of wing stroke deformation, but also its time course of activation. ii. time course of activation of each type of deformation is independent from the others in the identified set.

1.4.2 Insect flight: a model system for motor control

Insect flight provides a powerful model system for neuromotor control (Wilson 1961; Frye and Dickinson 2001; Taylor 2001). Flight puts extreme physiological demands on the organism, which are met by specialized adaptations with sharply defined structure-function relations (Dickinson et al. 2000). This is particularly apparent in flies, in which the generation of power for wing motion and the control of fast modulations of the wing stroke are mediated by two distinct types of muscles (Dickinson and Tu 1997; Bartussek et al. 2013). This ingeneous compartmentalization of the flight muscles allows to separately study the two major aspects of flight control. In one of the fastest motor acts in animal kingdom, flies take just about 70 ms to initiate an escape response at the sight of a looming threat (Bender and Dickinson 2006; Card and Dickinson 2008; Muijres et al. 2014), in which they attain a turning speed of 3800 - 9000$^{\circ}s^{-1}$ and rapidly move away from the threat within 7 ms (Muijres et al. 2014). This whole behavior relies on a number of extremely

sophisticated sensory modalities; the fastest visual system with minimum visual-motor delay, gyroscopic mechanosensory organs for active stability control, fastest sensory-motor loop wherein the sensory feedback directly acts on the actuator muscles. Such exceptionally performing sensory systems make structure-function relationships more obvious and flies alone embody a number of such sensory systems.

Flies are a very different organism than even the simplest of the mammals, needless to say humans. It is therefore amazing that about 60% of human genes have functional orthologs in *Drosophila* and that the processes utilizing these orthologs to organogenesis and neuron development (among others) are conserved to a very high degree (Nichols 2006). More importantly for the motor control studies, flies exhibit a number of complex motor behaviors such as courtship, flight navigation etc., that are of relevance to humans (Greenspan and Dierick 2004). In addition, Drosophila melanogaster being a versatile model organism in bio-medical studies has a strong base of well-studied genetics and state-of-the-art genetic approaches of controlling motor behavior.

In the end, a major technical advantage that makes flies favorite model organisms across fields of studies (Jennings 2011) is that they are easy and inexpensive to rear in the laboratory. They are ubiquitous, have a shorter life cycle and multiply faster, making the studies easily repeatable.

1.4.3 Neuromuscular basis of wing motion

Body structure of the fruit flies, like that of any other insect, is compartmentalized into three interconnected distinct anatomical sections: the head, the thorax and the abdomen (Fig. 1.3A). In the dipteran flies, as *Drosophila melanogaster*, the head is the major cite for sensory systems, information processing and feeding. It comprises of a pair of sensory antennae, compound eyes, ocelli and mouth parts. The thorax mainly houses the appendages that actuate locomotion i.e. 6 pairs of legs, a pair of wings and a pair of modified hind wings. The abdomen contains the other life sustaining systems such as the digestive tract, reproductive organs, osmoregulatory organ, main parts of the circulatory system (conical chamber, heart) etc. The distinctness of dipteran flies is their specialized hind wings. Unlike other flying insects, in dipteran flies the hind wings do not play aerodynamic

roles in flight actuation. Instead they have been modified into club shaped small appendages called halteres that oscillate with the same frequency as the wings but in complete anti-phase. Due to their structure and the oscillatory motion they are subject to the Coriolis force when the fly body rotates, and hence are used as mechanosensory organs to sense the angular velocity of body rotations.

Groups of muscles that control the wing motion and the halteres are all situated in the thorax region of the fly body (Fig. 1.3). In flight fruit flies beat their wings approximately 200 times in one second and the wing kinematics is precisely controlled throughout each stroke. Such a demanding motor task pushes the neuromuscular system to its performance limits, making dedicated structural adjustments for functional benefits. An extreme functional dichotomy is seen within the flight musculature of flies, wherein a group of larger muscles filling the thorax are especially designed to generate higher power per contraction; while about a dozen small muscles at each wing base are designed to be activated with minimum delay at neural commands (Dickinson and Tu 1997; Walker et al. 2014). The former sets of muscles are called the power muscles and are responsible for generating the main oscillatory wing motion. The latter group called the steering muscles, constitute less than 3% of the total mass of the flight muscles (Walker et al. 2014) but are responsible for the most vital part of flight control, i.e. changes in wing kinematics that result in maneuvers. Steering muscles achieve this seemingly difficult task of instantaneously modifying the output of the much larger power muscles by changing the pattern in which the exoskeletons move; which shifts the wing hinge movements between different modes of oscillations (Walker et al. 2014).

The knowledge we have today about the dipteran flight musculature and its functionality comes from studies on different dipteran flies; but the difference in most cases is small enough that the information can be considered general. In this subsection the two distinct groups of flight muscles and their functioning principles are discussed shortly.

Power muscles: anatomy, activation and functionality

Power muscles (Fig. 1.3B, color codes: red, yellow) constitute of two antagonistic sets of muscles. One set comprises of a pair of thick muscles running medially in the rostro-caudal direction along the full length of the thorax, called the dorsal-longitudinal muscles (dlm). The second set comprises of three muscles aligned perpendicular to the long axis of the fly body, on each side of the pair of dlms, called the dorso-ventral muscles (dvm) (Dickinson

and Tu 1997; Schlurmann and Hausen 2007). Each dlm muscle comprises of six muscle fibers stacked on top of one another; the anterior-most dvm muscle contains three muscle fibers and the two posterior ones contain two muscle fibers each. Each power muscle is innervated by characteristic, structurally homogeneous group of motor neurons those share a common bilateral dendritic area in the dorsal part of the wing neuropil (Schlurmann and Hausen 2007). The mesothoracic wing neuropil is the motor center of the flight muscles in the thoracic ganglion (equivalent of the vertebrate spinal cord in insects).

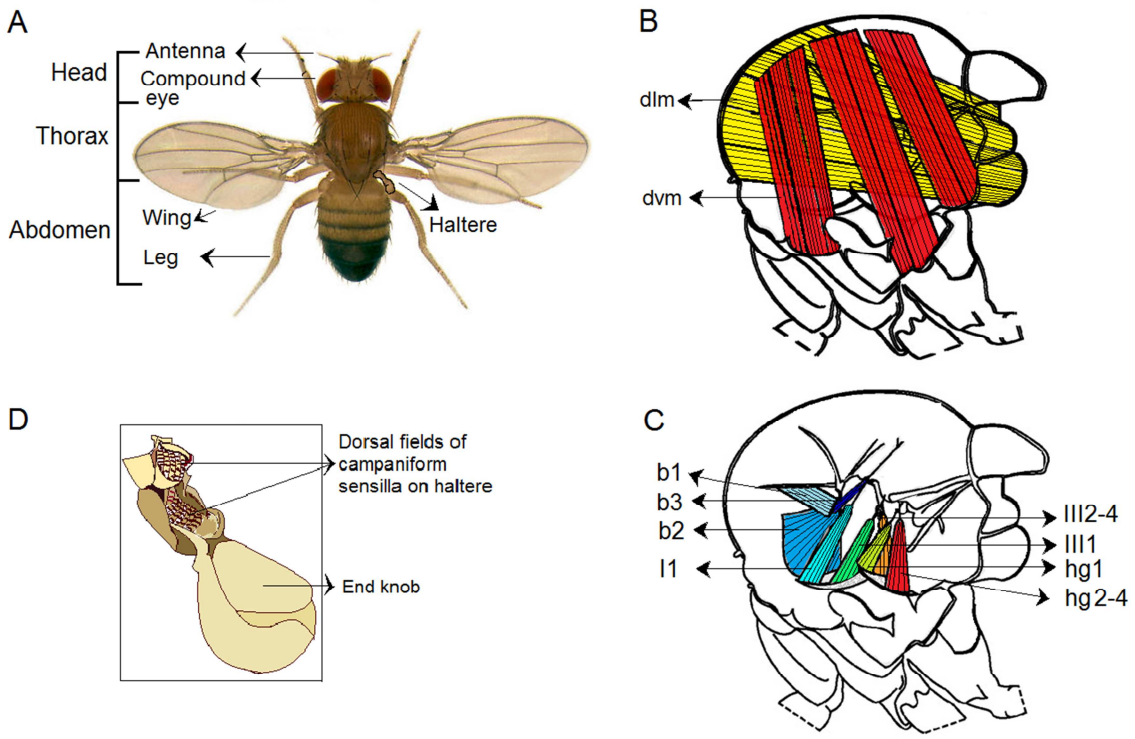

Figure 1.3: Flight apparatus of *Drosophila melanogaster*. A) Fly body showing the main body segments, the locomotor organs and the sensory organs, antennae, compound eyes and the halteres. **B)** Visualization of the flight power muscles (dorsal-longitudinal and dorso-ventral) contained in the thorax. **C)** Visualization of the steering muscles. B-C are redrawn from figure 2A of (Dickinson 2005). **D)** Microscopic structure of the halteres highlighting two major fields of mechanosensors.

The contractions of the power muscles however are myogenic (section 1.2.1), and the main function of their innervating motor neurons is to maintain the cytosolic calcium at certain levels (Dickinson et al. 1998a). Studies have shown that the muscles contract a number of times for each action potential in their motor neuron. Evolutionarily these muscles have developed to have much higher proportion of contractile filaments and mitochondria as compared to the sarcoplasmic reticulum (SR) (Smith 1984). The volume of the contractile

apparatus within a muscle is an indicator of its power generating capacity and that of the SR determines the degree to which a presynaptic motor neuron may control its contractions. Hence, the anatomical characteristic of the power muscles are understandably shifted towards generating higher energy per unit time while compromising direct neural controllability. The muscle contractions are stretch activated and during flight the contraction of each of the antagonistic muscle provides the requisite stretch to activate the other. Contractions of the dlms increase the length of the thorax also generating the mechanical strain that activates the dvm muscles. In the next cycle the dvms contract to increase the width of the thorax, in the process activating the dlms again. This cycle continues as long as the motor neurons activities keep the muscles in an active state. Therefore the frequency of the wingbeat oscillation is governed by the mechanical properties of the thorax such as the muscle stiffness, wing loading etc., and not the rate of motor neuron activity. As these muscles act on the thorax and do not insert at the base of the wings whose motion they actuate, they are called indirect muscles.

The main functionality of the power muscles is to generate necessary mechanical power for sustaining flight. Flies in flight use muscle power for the following tasks (Dickinson and Tu, 1997; Chapter 19, Vigoreaux, 2006): i. to accelerate the wings back and forth during flapping motion, ii. to overcome the drag force of the air on the wings and on the body (separately), iii. to generate the requisite lift force to offset its own weight. Generating enough energy per unit time that can meet the requirements of all the three tasks is extremely demanding and the requirement is greater than that for any other mode of locomotion. To meet this high power demand, these muscles are anatomically designed to generate higher mechanical work for a given muscle volume per unit time. In addition the musculoskeletal system also adapts a number of energetically beneficial mechanisms to minimize the energy cost of flapping flight, such as increasing the efficiency of converting chemical energy into aerodynamic flight forces and so on (Dickinson and Tu, 1997; Chapter 19, Vigoreaux, 2006). Although the rate of motor neuron activities does not directly control the rhythmic contractions of the muscles, it has been shown to play a vital role in tonically controlling the overall power generated per contraction (Dickinson et al. 1998b).

Steering muscles: anatomy, activation and functionality

There are about 22 pairs of steering muscles (Hedenström 2014). Out of these only about a dozen insert directly on the cuticular elements called sclerites at the base of the wing, rest influence the wing motion by altering the resonant properties of the thorax (Dickinson and Tu 1997). The characteristic feature that distinguishes steering from the power muscles is their anatomical design for neural activation with minimum delay. Depolarized motor neurons stimulate the release of calcium ions from the SR to the cytosol by a fast diffusion process. These released calcium ions then lead the chain of bio-molecular interactions that finally end in muscle contraction (Szent-Györgyi 1975). Hence, the steering muscles having a higher cellular content of SR, have shorter action potential to contraction delay.

Almost all the steering muscles are innervated by individual distinct motor neurons. High wingbeat frequency puts a constraint that each motor neuron fires only once during a wingbeat cycle. More than one spike per stroke cycle is rare and occurs only when the flies are faced with extreme flight force requirements, such as during flight initiation (Lehmann and Götz 1996). The activation processes are made more challenging by the requirement of a precise phase of activation in most cases; as studies on drosophila (Heide and Götz 1996) and other dipteran flies (Tu and Dickinson 1996) have shown that muscle activation phase influence their efficacy on the wing kinematics. Unlike the power muscles, steering muscles (other than the first basalare muscle M. b1) are not active throughout the flight. They are activated during specific flight maneuvers or during flight initiation or termination (Dickinson and Tu 1997).

Sclerites	Flight muscles (abbreviations)
Basalar	M. b1, M. b2, M.b3
1st Axillary	M. I1, M. I2
3rd Axillary	M. III1-4
Posterior notal wing process	M. hg1-4

Table 1.1: Overview of the *Drosophila* flight steering musculature. Main sclerites and their associated flight muscles. For diagram refer to figure 1.1.

Acting at the junction of the wings and the animal body, these steering muscles regulate how the mechanical energy of the power muscles is transformed into wing motion by

altering the mechanics of the wing hinge (Dickinson 2005; Walker et al. 2014). To understand the organization of the steering muscles and their functionality it is important to have some knowledge of the complex exoskeleton at the wing base. The wing hinge comprises of a complex lever like structure formed by four axillary sclerites, as shown in figure 1.1D. Out of these the first, third and the fourth have attached steering muscles and are actively controlled. In addition the wing hinge is connected via tendons to the basalar plate which projects into the thorax. In flies the fourth axillary sclerite is commonly called the posterior notal wing process and is fused into the thorax (Walker et al. 2014). The steering muscles controlling each sclerite of the wing hinge is summarized in table 1.1. For further anatomical details of the muscles and their connections to the sclerites please refer to the comprehensive review and report (Miyan and Ewing 1985; Dickinson and Tu 1997).

Recent studies have revealed much about the mechanisms by which these steering muscles move the wing articulation (Walker et al. 2014), yet the understanding is not complete. Here, I briefly mention how some of the main steering muscles of *Drosophila* (Fig.1.3) act on the wing articulation; their effects on the wing kinematics will be mentioned in the last section of this chapter (section 1.5). I focus on only those steering muscles that are relevant in explaining the significance of some of my own results. For corresponding details of other steering muscles please refer to (Dickinson and Tu 1997) or for a more recent and advanced study (but on limited steering muscles) to (Walker et al. 2014).

i. First muscle of the basalare sclerite (M.b1): M.b1 is the only known steering muscle that is activated even during a straight flight. It is typically activated every wingbeat cycle close to when the wing reaches the dorsal extreme of its swing and starts to move towards the ventral direction. When tonically active this muscle is thought to keep away a protruding part of the wing hinge so as to prevent it from abruptly stopping the wing motion near the ventral portion of the stroke. However, during visually induced steering responses the activation of this muscle shifts by 1-2ms within the wing stroke, which changes its dynamic stiffness.

ii. Second muscle of the basalare sclerite (M.b2): This is the largest steering muscle attached to the largest sclerite at the wing base. This muscle is activated only during visually induced turning maneuvers in the wing at the outer side of the turn. The

activation occurs every other wingbeat cycle, close to the end of the ventral-to-dorsal swing of the wing motion (Heide and Götz 1996; Lehmann and Götz 1996). This muscle when active is thought to change the orientation of the basalare sclerite, so as to increase the ventral extent of the wing motion (Walker et al. 2014).

iii. First muscle of the first axillary sclerite (M.I1): This muscle is also active only during visually induced responses, but in the wing at the inner side of the turn. It is activated close to the dorsal-to-ventral swing of the wing motion and is known to pull the first axillary sclerite forward and downward (Heide and Götz 1996; Dickinson and Tu 1997), which has an effect of reducing the ventral extent of the wing motion.

1.4.4 Stroke-by-stroke wingbeat control and the role of halteres

To move through any environment flies not only need to generate sustained power and steer but also constantly correct for the inherent instabilities in flapping wing flight. Studies that couple aerodynamic forces to the rigid-body (passive) dynamics of a flying insect (Sun and Xiong 2005; Zhang and Sun 2009; Faruque and Sean Humbert 2010a, 2010b; Cheng and Deng 2011) show that wing flapping introduces certain diverging oscillating instabilities in the body motion. The oscillating instability in the longitudinal dynamics destabilizes the pitch attitude (Sun and Xiong 2005; Cheng and Deng 2011; Ristroph et al. 2013), while that in the lateral dynamics destabilizes the roll balance (Cheng and Deng 2011). In the absence of any active control mediated by the sensory feedback, in fruit flies these disturbances can grow up to 67% of the initial value in merely 75 ms (i.e. 15 wingbeats, as estimated from table IV of (Cheng and Deng 2011)). Hence to avoid tumbling from the air, flies need to have corrective measures that act at a rate faster than the growth rate of the disturbances. In addition to these intrinsic instabilities, there are also umpteen external factors that the flies need to respond to within a few wingbeat cycles so as to maintain a stable flight or to escape a predator. Ristroph and colleagues have shown that the fruit flies can sense rotational deflections (yaw and pitch) and revert to their original flight attitude and direction in merely 50-60ms (i.e. ~10-15 wingbeat cycles) (Ristroph et al. 2010, 2013). While such corrective maneuvers showcase the agility of insect flight, the precision of wing movement is also crucial; especially because even slight alteration of the wing motion results in large

fluctuations of the aerodynamic forces (Fry et al. 2003, 2005). Hence, it is clear that the flies heavily rely on fast sensorimotor control of the wing motion.

The flight behaviors of flies provide enough indication that control strategies with very fast reaction time play a key role in flight stabilization. All sensory systems of the flies are anatomically and neurologically better optimized than other animals to have reduced latency and increased temporal resolution. But the mechanosensory feedback from the modified hind wings of the dipteran flies, i.e. the halteres are the most efficient of them all. Halteres beat in anti-phase to the wingbeat and are known to detect any rotation of the fly body by sensing the Coriolis force and other inertial forces. While the visual to motor delay is typically 6-8 wingbeat cycles (30ms in *Musca* (Land and Collett 1974), 40ms in *Drosophila* (Heisenberg and Wolf 1988; Hardie and Raghu 2001)), the haltere mechanosensor to wing steering muscle stimulation delay is less than one wingbeat cycle (approximately 3ms in *Calliphora* (Fayyazuddin and Dickinson 1996)). Halteres achieve this response expediency by virtue of low latency spike responses to mechanoreceptors (Fox and Daniel 2008) and direct (monosynaptic) electrical synaptic input to steering motor neurons from haltere afferents (Chan and Dickinson 1996; Fayyazuddin and Dickinson 1996). These allow the halteres to provide wingbeat related feedback to the steering muscles at the time scales of a single stroke cycle (Fayyazuddin and Dickinson 1996), making it the fastest sensorimotor loop.

Since, the 18th century work of Derham (Derham 1720) a number of studies (Dickinson, 1999; Fraenkel and Pringle, 1938; Nalbach, 1993; Pringle, 1948, to name only a few) have explored the pivotal role of halteres in maintaining stability during flight. However, most of these works studied the sensory contribution of the halteres in generating robust response to inflight perturbations. These studies provide a close to complete understanding of the gyroscope like functionality of the halteres; wherein the mechanosensors at the base of the haltere (Gnatzy et al., 1987) detect any torque acting on the fly body and stimulate appropriate motor action to generate precise counter torque. However, out of the 5 identified fields of the campaniform sensilla at the haltere base some fields (like dF1, dF3, and vF1) (Gnatzy et al., 1987) are oriented parallel to its longitudinal axis and monitor the large forces resulting from just the oscillation of the haltere in its stroke plane (Pringle 1948; Nalbach 1993). In dipteran insects this feedback is known to structure the activity of the first basalar muscle (b1) (Chan and Dickinson 1996; Fayyazuddin and Dickinson 1996)

activated in every stroke cycle, throughout the flight (Heide and Götz 1996). Recent simulation studies of insect flight (Chang and Wang 2014) indicate that this fastest sensorimotor loop may play a crucial role in keeping the fly aloft. Ristroph and colleagues (Ristroph et al. 2013) show that a modification of gluing dandelion seed fibers to the fly's lower body to increase the pitch damping restores body pitch stability in haltere immobilized flies. This finding clearly shows that at least one functionality of the haltere sensory system is to actively stabilize the pitch attitude during flight.

1.5 Kinematic data analysis

The ultimate output of all motor control systems is the movement of the concerned organ or the limb; any change in control mechanism therefore manifests as a modification of the limb kinematics. Two possible approaches of studying the organization of the motor control system are: i. at the physiological level by measuring the activity patterns of each muscle or muscle groups and their corresponding effects on the behavior, and ii. at the functional level by studying the kinematic output of the motor control system and the relationship between different behavioral features.

Muscle activities measured simultaneously with limb kinematics allow identification of muscles that bring about specific changes in the motor output. Such studies have led to the conception of modularity of neuromuscular systems where in a group of muscles, called muscle synergies, are always simultaneously activated in connection to specific kinematic changes. Till date many such muscle synergies have been identified and characterized in vertebrates as well as in invertebrate model organisms. For example in bullfrogs specific groups of muscles with extensor action on the hip, knee and the ankle joints of the hind limbs are simultaneously activated (d'Avella and Bizzi 2005) during walking, jumping as well as swimming. It is known that during all the modes of locomotion the hind limbs play a crucial role in generating the forward thrust and hence, the above finding indicates that at least some part of the hind-limb kinematics is shared between the three modes of locomotion. Similarly, biomechanical movement analyses of human gait with the knowledge of underlying electrophysiological activities have also helped in understanding the corresponding neuromuscular control mechanisms (Simonsen 2014).

On the other hand the functional relationship between the limb kinematics and the resulting changes in the behavioral output can be studied by bypassing the anatomical details. This is made possible by the fact that the ultimate interaction of the motor system and the outside world depends on the dynamics of the limb and the corresponding reactions from its environment; which has nothing to do with the neuromuscular origin of the limb motion at

the first place. Such analyses are useful when the goal is to understand the general organization of the control system in terms of its output; for example to address questions like: why is it necessary to change gaits while transitioning from walking to running, how does a fly efficiently steer through the air while quickly changing its direction, and so on. Biomechanical studies of the motor systems are often based on theoretical or phenomenological models of the interactions within the motor system and those with the external surrounding (For example: Bartussek et al., 2013; Bergou et al., 2010; Hogan and Sternad, 2012; West and Scafetta, 2003). Suitably designed dynamically scaled robots have also contributed significantly to our understanding of the biomechanics of various complex motor systems (For example: Dickinson et al., 1999; Wolpert and Flanagan, 2010).

The difference between the two approaches of studying the organization of the neuromotor control lies mainly in the domains in which the results can be justifiably interpreted. To interpret motor behavior from the analyses of muscle activities often becomes too complex even for smaller systems with fewer in-between steps. The prime factors that lead to this increasing complexity are the inherent nonlinearity and the redundancy of the musculoskeletal system. Even in model organisms like the fruit fly, a pattern of muscle activity leads to muscle twitches, which then move the associated sclerite, this movement then finally modifies the wing motion. There is prospective non-linearity at each step, starting from the muscle mechanics to the transfer of the wing hinge motion to the wing motion. On top of it different muscles can have very similar effects on the motor output; for example in the dipteran flight musculature the first and the second basalar muscles (M.b1 and M.b2) both have an effect of increasing the wingbeat amplitude. All these complexities increase manifold with increasing diversity of muscle types and increasing complexity of the musculoskeletal system in higher animals. For these similar reasons it is almost impossible to infer about the underlying muscle activity patterns purely based on the results of the kinematic analysis of the motor behavior.

1.5.1 Important kinematic parameters of hand motion and their significance in characterizing tremors

Amplitude, frequency (table 1.2) and the condition under which the tremor is activated (tables 1.2 and 1.3) are the key features in the clinical diagnosis of the tremor types (Deuschl et al., 2001; Hess and Pullman, 2012). Hence, assessment of the motion of different body parts such as head, trunk, hands, arms, etc is a part of the general as well as disease specific tremor rating scales (see review (Elble et al., 2013)). However, as tremors are broadband oscillations and often corrupted with slow drifts and other artifacts the tremor amplitude is not obtained directly from the peak-to-peak distance of the acceleration data. Instead the more common practice is to obtain the amplitude from the power spectral density estimate (see section 4.2.3) within a frequency band about the main tremor frequency (Timmer et al., 1996). This provides a more meaningful estimate of the extent of hand motion that can be attributed to a specific type of tremor.

Table 1.2: Tremor etiology and occurrences of the most common types of tremor.

Etiology	Rest Tremor	Action tremor		Frequency
		Postural tremor	Kinetic tremor	
Parkinsonism[1]	often present	sometimes noted	rarely noted	3-6 Hz
Essential tremor[1]	sometimes noted	always present	always present	4-12 Hz
Enhanced physiological tremor	-	always present	often present	6-12 Hz
Orthostatic tremor	-	always present	-	>13 Hz
Dystonic tremor	rarely noted	usually noted	usually noted	< 7 Hz

[1](Hess and Pullman, 2012),

All the tremor rating scales are to a large extent subjective to the examiner and difficult to standardize across subjects. For example in the Fahn-Tolosa-Marin tremor rating scale, tremor severity is judged partly based on visible assessment of the tremor amplitude. In this 5-point scale a score from 0-4 is assigned to the tremor arising in each body part as: none (0), slight (1), moderate (2), marked (3), and severe (4); severe being defined as a tremor with amplitude > 4cm. Also, even the best clinical scale is not sensitive enough to

allow detection of minimal abnormality or subtle changes in the progression of the disease (Hess and Pullman, 2012). Hence, the present state of tremor evaluation can benefit largely from an objective and accurate measure of tremor.

Table 1.3: Tremor categorizations based on its condition of occurrences. For further sub and super categories see (Hess and Pullman, 2012).

Category	Definition
Rest	Tremor arising in a body part that is not in voluntary motion and is supported against gravity.
Action	Tremor arising in a body part with voluntary muscle contraction.
Postural	It is subtype of action tremor in which the tremor arises in a body part that is maintained in a posture against gravity.
Kinetic	It is a subtype of action tremor in which the tremor arises in a body part that is in motion.
Intension	Tremor with increased severity during the initial and and/or pre-terminal phase of a targeted movement. It is a variant of kinetic tremor.
Task-specific	Tremors arising during specific tasks such as writing, speaking. Also a variant of kinetic tremor.

Kinematic analyses provide the simplest extensions of the existing tremor assessment tests that can make these tests more precise and objective. A good example is the analysis of the spiral drawing (Pullman, 1998), a standard clinical test for detecting movement disorders. In this extended assessment the hand drawn Archimedean spiral aquired in a virtual triaxial setup (X,Y, pressure) on a digitized tablet is characterized by mathematically estimating the parameters such as smoothness of the lines, tightness etc. Using these parameter values together with the kinematic measures such as the peak frequency and power along the three axes, the computer was trained to rate spirals in the same manner as expert Clinicians.

Tremor coherence

A very important characteristic of the tremors arising in different body parts is the extent of their mutual synchronization; both in the case of patients as well as healthy subjects. In principle, finding of coherence between kinematics of the tremors implies that at least one of the following mechanisms participates in the genesis of the respective tremors:

i. A common neural generator (be it one central generator or two coupled unilateral generators, as shown in (Muthuraman et al., 2013) for the orthostatic tremor).

ii. A common pathway of motor control; i.e. neural signals originating at two distinct sources interfere in the pathways leading to the effector muscles. For example, the synchronization of the psychogenic tremors is known to actuate via the common pathways that underlie bimanual interference during voluntary movements (Hallett, 2010; Klapp, 1979).

iii. A common mechanical forcing, such as the common ballistocardiac drive that leads to coherent oscillations of the limb extremities in the resting posture (Marsden et al., 1969a).

There are several lines of evidence suggesting that a coupling on the neural level (i.e., mechanisms i or ii) may play a role in physiological tremor of the two hands. (Morrison and Newell, 1999) showed that the splinting of joints in one upper limb significantly changes the frequency profile and the pattern of intra-limb coupling of PT in both the limbs. As no significant correlation between the hand tremor and the torso motion is evident during the specific postural task, as shown in (Morrison and Newell 1996), simple mechanical linkage does not seem to be the primary pathway of bilateral interaction (Morrison and Newell, 1999). It was proposed that a large proportion of the bilateral tremor comes from a common central mechanism. The lack of bilateral coherence was explained by distinct modifications of this common input in the left and the right side before reaching the effector muscles. Recent studies based on the muscle EMG (Boonstra et al., 2008; Kavanagh et al., 2013) also suggest a role of the motor control system in the bilateral interaction of PT. (Kavanagh et al., 2013) showed that fatigue inducing contractions in the extensor muscles of one hand increased the muscle activity and tremor in the contralateral limb.

Other than important implications regarding the genesis of the specific tremor, the extent of synchronization can also play a significant role in differential diagnosis of tremors. Differential diagnosis of tremors, while of prime importance for therapeutic measures, can sometimes become a challenging task for clinicians (Louis, 2005). While tremor frequency plays some role, the tremor amplitude usually does not help much in differentiating tremors; mainly because it varies widely even in the same kind of tremor. For example in

cases of mild essential tremor (ET) the tremor amplitude is comparable to that of enhanced physiological tremor (EPT) (Louis, 2005). In this case the differential diagnosis is made even more complicated by the fact that in some young patients the usual 4-6 Hz frequency range of ET shifts to 10-12 Hz, which coincides with that of enhanced PT (Louis, 2005). Hence often additional tests are required to identify the type of pathological tremor.

Of all the tremor types that may occur bilaterally, orthostatic tremor (Lauk et al., 1999) and psychogenic tremor (McAuley and Rothwell, 2004) have been shown to have high bilateral coherence. A standard test used to differentiate psychogenic tremor from other organic tremors, such as Parkisonian tremor, essential tremor, dystonic tremor etc., is the coherence entrainment test (McAuley and Rothwell, 2004). This test is based on the inherent tendency of the voluntary periodic motion on one side of the body to synchronize with that on the other side. While it is extremely difficult for subjects with unilateral psychogenic tremor to maintain a different tapping frequency in the opposite hand, patients with organic tremors can easily perform finger tapping while maintaining a different tremor frequency in the other hand. However, for other tremor types, only limited evidence of bilateral coherence has been shown in the previous literature. In Parkinson disease tremor, (Moore et al., 2000) reported brief intervals of bilaterally coherent oscillation in hand kinematics, while studies assessing muscle activity (Lauk et al., 1999; Raethjen et al., 2000a) did not find any bilateral coherence. In essential tremor (ET), (Hellwig et al., 2003) found transiently occurring bilateral coherence of the wrist extensor muscle activities, while (McAuley and Rothwell, 2004) reported occasional kinematic bilateral coherence that was not accompanied by EMG coherence. In postural physiological tremor (PT), no bilateral coherence has been reported in either kinematic or EMG studies (Marsden et al., 1969b; Morrison and Newell, 2000; Timmer et al., 2000). However, highly prevalent bilateral coherence of finger motion was found in the resting tremor of healthy subjects (Marsden et al., 1969a), and was attributed to the mechanical effects of ballistocardiac forcing.

1.5.2 Important kinematic parameters of the wingbeat and their aerodynamic significance

Active control of flight is all about modulation of wing tip trajectory to modify aerodynamic forces. A wingbeat cycle of insects with flapping wing flight is commonly divided into four phases (Zanker 1990a):

i. Upstroke: during this phase the wings are pulled at a very high speed from ventral towards the dorsal part of the body (Fig.1.4A). The wing's leading edge (black dot on the wing chord, Fig. 1.4A, B) surges firmly in the direction of the abdomen, while the trailing edge is dragged along. In a straight flight the wing angle ($\alpha(t)$ in Fig. 1.4B) remains relatively constant during this excursion (Balint and Dickinson 2004; Bergou et al. 2010).

ii. Dorsal reversal: during this phase the wing reverses the direction of its translation from upstroke to downstroke (Fig. 1.4A). In fruit flies the leading edge of the wings (costal veins) approach towards each other, make a contact with an increasing area of overlap until they start peeling off and moving away from each other. This is called the clap-and-fling maneuver of the wings due to the similarity of the acts and is accompanied by a rotation of the wing about its longitudinal axis. This maneuver plays a pivotal aerodynamic role in generating the necessary life force to keep the fly aloft. The relative phase of the wing flip to the wing reversal also has significant effects on this aerodynamics (Dickinson et al. 1999).

iii. Downstroke: In this phase the wing sweeps from the posterior dorsal position to the anterior ventral position with a velocity slower than that of the upstroke. Again in this phase the wing angle remains relatively constant, but the magnitude may differ from that of the upstroke (Bergou et al. 2010). The changes in the stroke deviation ($\theta(t)$ Fig. 1.4B) and the wing tip velocity (i.e. rate of change of $\phi(t)$, Fig. 1.4B) during this phase are found to be correlated with the changes in the magnitude as well as the inclination of the total flight force (Balint and Dickinson 2004).

iv. Ventral reversal: At the end of the downstroke the wing changes the direction of its translation and starts moving towards the posterior dorsal position. This phase is accompanied with an extremely fast flipping of the wing from pronation to supination (angular velocity upwards of 10^5 degrees/s (Zanker 1990a)). The relative phase of the rapid wing supination w.r.t. the ventral reversal plays a very important role in determining the lift force generated by each wing (Dickinson et al. 1993, 1999).

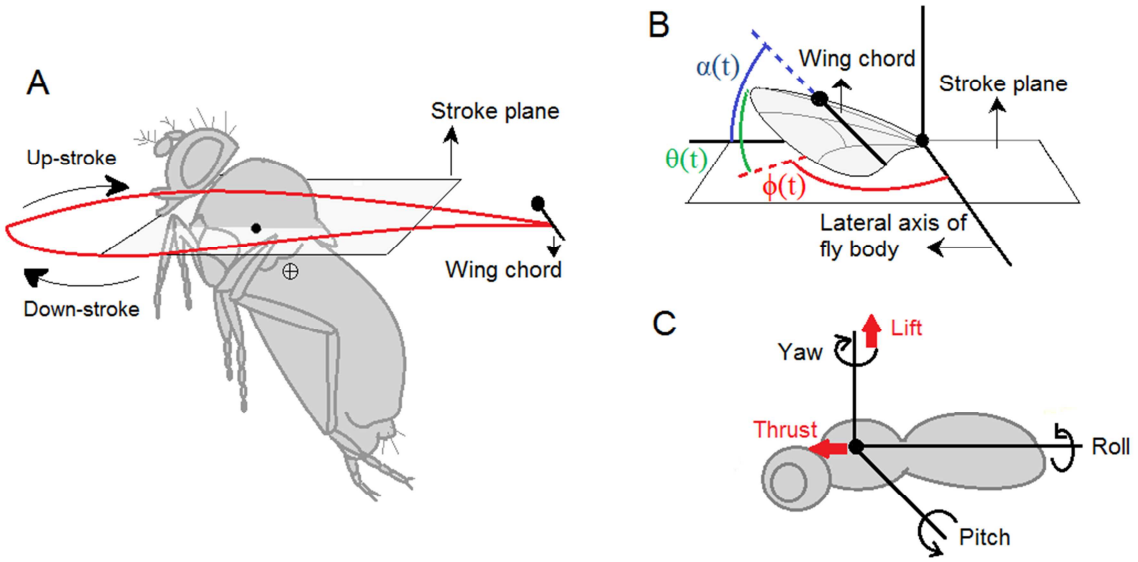

Figure 1.4: Wing stroke and related kinematic parameters. A) Typical wing tip trajectory (red curve) during a flapping stroke of the fruit fly *Drosophila melanogaster*, superimposed on a side view (sagittal section) cartoon of the fly body. Black dot marks the position of the wing base (wing not shown). Circle with cross marks the center of mass of the fly body (Redrawn and modified from figure 1 of Lehmann and Pick, 2007). **B)** Commonly measured angular parameters of the wing stroke, ϕ(t): stroke angle, θ(t): stroke deviation from the mean stroke plane and α(t): wing (pitch) angle. C) Nomenclature of the possible motions along the three principal axes of the fly body. Rotations about the longitudinal, transverse and the vertical axes of the fly body: roll, pitch and yaw respectively. Translations along the same respective axes: thrust, side slip and lift.

The full repertoire of flight maneuvers are generated by suitably modifying these four phases of the wing stroke. For example flies modify stroke amplitude, i.e. the planar angle of the arc in the stroke plane described by the wing leading edge, to control the overall flight power (Lehmann and Dickinson 1998; Taylor 2001). Yaw torque is known to be generated by bilaterally asymmetric changes in stroke plane angle (Fig. 1.4) and the mid-stroke angle of attack (Fig. 1.4) (Fry et al. 2003; Bergou et al. 2010), while a symmetric change in the mean wing translational velocity or in the timing of wing rotation alters the lift force (Lehmann and Dickinson 1998; Dickinson et al. 1999). A change in pitch torque can be achieved by a bilaterally symmetric change in mean stroke position (Zanker 1990b; Truong et al. 2014) or in the ratio of down- and upstroke duration (Fry et al. 2005). For a more comprehensive review of the correspondences between the wing kinematics of flies and their aerodynamic consequences, please refer to (Taylor 2001).

In recent years, flight control in flies has been extensively investigated using integrative approaches. In particular, the quantitative correspondence between the kinematic patterns of wing motion and the resulting aerodynamic forces has been clearly established using dynamically scaled robotic models (Dickinson et al. 1999; Sane and Dickinson 2001; Fry et al. 2005). This knowledge provides a functional interpretation of observed variations in the fly's wing kinematics. Detailed measurement and analysis of wing kinematics therefore has the potential to reveal the functional organization of the flight control apparatus.

CHAPTER 2

Research hypotheses and objectives

2.1 Topics and motivation

2.1.1 Extent of bilateral coupling in physiological and essential tremor

Physiological and essential tremors mostly occur in limbs on both the sides of the body, with similar fundamental frequency of the oscillations. This raises the possibility that the contralateral tremors may have a common source or are otherwise coupled. To confirm such coupling, however, it is necessary to systematically assess the dependence of the two tremor oscillations. A finding of significant coherence between the tremors in opposite limbs points towards a common mechanism of tremor genesis (see section 1.5.1). In addition, the understanding of bilateral tremor coherence is also important for differential diagnosis of tremor diseases. A recent review by Elble (Elble 2013a) points out towards the cardinal need of improving our understanding of tremor genesis in order to make the therapeutic measures more accurate and definitively effective.

2.1.2 Modular control of complex wing stroke variations in fruit flies

Motor primitives (ref: section 1.4.1) that can be linearly combined to obtain complex motor activities have been reported in vertebrates. However, as the control system underlying voluntary motion is very complicated in humans, most of the studies were done on animals like frogs, cats, dogs etc. Even in these simpler vertebrates, motor primitives that occur in series (i.e. their occurrences do not coincide in time, for example walking, running, hopping) were mainly studied. In the first part of my study I aimed to find if this mode of motor control is also present in the fruit flies, *Drosophila melanogaster*. If present, this would provide a simpler system to understand the basic organization principles of motor primitives occurring in parallel (i.e. their occurrences can coincide in time) and can motivate studies in higher organisms.

2.2 Hypotheses

Hypothesis I: Couplings between the left and the right hand oscillations in PT and ET are weak and posture dependent

Till date bilateral coherence has been studied for almost all the tremors that appear bilaterally. While highly prevalent bilateral coherence was found in orthostatic tremor (Lauk et al. 1999) and psychogenic tremor (McAuley and Rothwell 2004; Raethjen et al. 2004), only limited evidence of bilateral coherence has been reported for the other types of tremor (see section 1.5.1). However, as discussed in section 1.5.1, bilateral interaction of tremor has been reported for both physiological and essential tremor. But, the exact nature and source of this coupling is not yet clear. Motivated by previous findings in literature, it was hypothesized that a weak coupling between the left and right oscillators in ET and in PT may lead to bilateral coherence that is transient or intermittent, and could sensitively depend on the posture and the evaluated kinematic parameters.

Hypothesis II: Fly wing motion is composed of mutually independent elementary kinematic patterns

Complex changes in the wing kinematics are observed in flies when confronted with stimuli that simultaneously activate multiple sensory modalities. In case of simultaneous visual and olfactory stimuli, changes in wing kinematics are instantaneous combinations of their individual motor outputs, i.e. increases in flight power and a simultaneous yaw turn. This provides evidence for the involvement of independent sensorimotor pathways in these two modalities. Instantaneous superposition of motor output has also been shown to occur for simultaneous presentation of visual and haltere stimuli. Motivated by these existing experimental evidences it was hypothesized that if the flight maneuvers of the fruit flies arise from the activation of a small number of independent neuromuscular control modes it should be apparent from the kinematics of the wing motion. Assuming that each control mode when active manifests into a specific kinematic pattern, the wing motion must be a combination of these independently controlled kinematic patterns.

2.3 Objectives

2.3.1 Analysis of human hand tremor

The objectives of the first part of my research in which I analyze the triaxial hand accelerations during rest and postural tasks in healthy subjects and essential tremor patients are the following:

- Estimate magnitude squared coherence (MSC) between the left and the right hand tremors.
- Use non-stationary analysis to find the changes (if any) in bilateral coherence between the tremors during the measured duration.
- Judge the extent to which the cardiac impulse (sec. 1.3.2) plays a role in synchronizing the tremors of the two hands.

2.3.2 Analysis of *Drosophila* wing motion

The objectives of the second part of my research in which I analyze the wing kinematics of tethered flying fruit flies during unstimulated flight are the following:

- Measure wing motion of tethered fruit flies in the flight arena, uninterrupted for long durations (i.e. ~10 000 wingbeat cycles) with a sampling frequency high enough to record the subtle changes in the stroke angle of the wing.
- Develop a suitable computational method to obtain the kinematic patterns that occur mutually independently in the measured wing kinematics.
- Interpret the significance and possible aerodynamic consequences of such kinematic patterns.

II. Materials and methods

CHAPTER 3

Experimental Methods

3.1 Overview

Experiments were performed to measure kinematic data that quantify the studied rhythmic motions, viz. *Drosophila* wingbeat and the human hand tremor.

Section 3.2 describes the subject demography of the studied groups of healthy subjects and essential tremor patients, experimental paradigm used to measure the hand motions and the data preprocessing. The hand motion data for 30 healthy subjects and 35 patients diagnosed with essential tremor, analyzed in this thesis, were provided to us by our collaborators in Dept. of Neurology and Centre of Clinical Neuroscience, First Faculty of Medicine, Prague. For a later part of my study discussed in section 5.2.4 new measurements were done on another group of 12 healthy subjects in the same lab.

Section 3.3 describes the details of the flies used, the rearing procedures followed, pre-experiment preparations, the experimental paradigm used to measure the fly wingbeat and the data preprocessing. The wingbeat data analyzed in this thesis (10 fruit flies) were taken from the database created by our collaborators in Fry Lab, Institute of Neuroinformatics, ETH Zurich and University of Zurich, Switzerland. The wingbeat data analyzed in section 6.3 were measured by me and a colleague Dr. Jan Bartussek in Kodrík Lab, Biology Centre of the ASČR, Institute of Entomology, České Budějovice.

3.2 Measuring hand tremor

In the first part of my study I analyzed 3D hand acceleration measurements of healthy subjects and essential tremor patients. The first subsection contains information about both the groups of subjects and in the second subsection I explain the experimental paradigm and the details of data acquisition.

3.2.1 Subjects

The tremor time series analyzed in this study were obtained from three groups of subjects. The first two groups, of 30 healthy subjects and of 34 patients diagnosed with essential tremor, were recorded as part of the study of (Šprdlík et al. 2011) (in which coherence was not assessed). The 34 ET patients in the first group were diagnosed according to the criterion stated in (Deuschl et al. 1998). This group had, age range: 19–81 yr (mean±std: 56.7±17.4 yr), disease duration: 24.3±16 yr, Fahn-Tolosa-Marín tremor rating scale score (Jankovic and Tolosa 2007): 27.0±13.4, score range 9–67. The second group consisted of 30 healthy subjects, age 53.8±17.4 yr (range 19–81 yr).

A third group of 12 healthy subjects (age 34±8 yr, range 26-51 yr, 8 females and 4 males) were measured to perform control analyses and to study the effect of balistocardiac forcing on bilateral coherence.

Healthy subjects in both the second and the third groups did not have any previous record or family history of movement disorders. The study was approved by the research ethics committee at First Faculty of Medicine, Charles University in Prague, and all participants provided signed, informed consent before entering the study.

3.2.2 Experimental procedure and data preprocessing

Positions studied

To measure the hand motion of the third group of subjects I used the same measurement procedure as was used for the first two groups in (Šprdlík et al. 2011). The hand tremor was recorded in three positions (Fig.3.1). The first, in which the hands hung freely from the wrist, was used to measure the rest tremor. The other two positions - with hands extended, and with the arms extended towards a horizontal target - were used to study postural tremor (Šprdlík et al. 2011, or Fig.3.1). In all the positions the subjects were seated comfortably in a sturdy armchair, and were instructed to lean their back into the backrest.

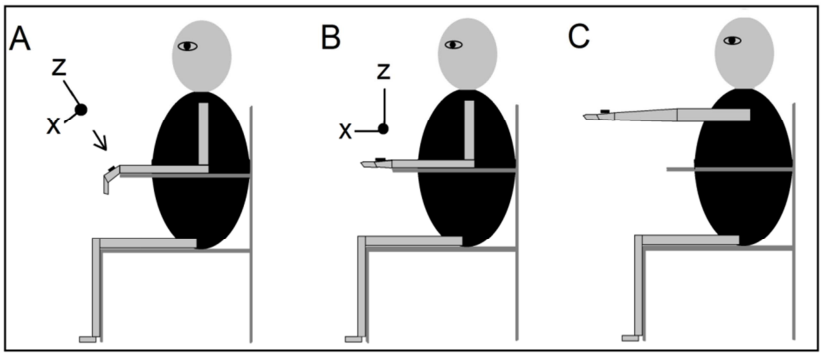

Figure 3.1: Cartoons of positions in which the hand acceleration was measured. A) Position 1: forearms leaned on the armrests and hands hanging freely down. B) Position 2: forearms leaned on the armrests and hands extended forward horizontally. C) Position 3: arms held forward horizontally towards a horizontal target placed in front of the subject at the height of shoulders, hands pronated. X, Y and Z indicate the orientation of the acceleration components measured by the triaxial accelerometers placed on the hand dorsa.

In control experiments designed to assess any role of direct mechanical coupling between the two hands via the wooden armchair, two left hands (or two right hands) belonging to distinct subjects were recorded. The first subject sat in the armchair and placed one hand on the armrest, while the second subject sat in an adjacent chair and placed one hand on the second armrest of the first armchair.

Measurement units and their placements

Integrated inertial measurement units MTx by Xsens were used to measure the acceleration of both the hands in the studied subjects. These units comprise of an accelerometer that measures 3D linear acceleration in $\mathrm{m/s^{-2}}$, a rate gyroscope that measures 3D rate of turn in $\mathrm{rad/s^{-1}}$ and a magnetometer that measures the 3D magnetic field (a.u., normalized to earth

magnetic field). All these parameters are measured in the sensor fixed coordinate system. For my studies I analyzed only the linear acceleration. The first row of table 3.1 gives the specifications of the accelerometers in these measurement units. The hand acceleration measurements were transmitted by cables to a personal computer via USB-RS232 and acquired using custom built software. The time axes of the MTx sensors of the two hands were synchronized using a custom-built hardware device. To confirm that no artifact was introduced by this device, for the third group the Xbus kit by Xsens was thus used. The Xbus kit allowed synchronous sampling from all 3 measurement units (one on each hand and one on chest). The Xbus output was transmitted wirelessly to the personal computer and acquired using the MT manager software. The specifications of the accelerometers in these units are given in the second row of table 3.1.

The measurement units were placed on subjects' hand dorsa over third and fourth metacarpal bones using neoprene bands with hook-and-loop fasteners. In addition, one unit was firmly attached to the chest (5cm to the left of the sternum) and used to record the chest wall acceleration. Two sets of 20s measurements were performed in each hand position, separated by a 10s interval of rest to avoid muscle fatigue. In all cases the recording of each test was started by manually pressing keys on the PC keyboard.

Table 3.1: Specifications of the accelerometers in the measurements units

Measurement units	**Full scale**	**Sampling frequency**	**Weight**	**Dimension** (W x L x H)
MTx -28A##G##	$\pm 17\ \mathrm{m/s^{-2}}$	100 Hz	30g	38 x 53 x 21 mm
MTx - 49A##G##	$\pm 50\ \mathrm{m/s^{-2}}$	100 Hz	30g	38 x 53 x 21 mm

Data preprocessing

Minor data preprocessing was done before performing the coherence analysis. First, any slow drift present in the measured hand acceleration was removed by subtracting the best linear fit from all the three components. Then the two sets of measurements, each 20s, were combined to produce one 40s long time series. By increasing the data length in this way I increased the significance level of all the estimates while avoiding the effects of muscle fatigue.

3.3 Measuring wing kinematics of tethered flying fruit flies

For the second part of my study the wing angular positions of flying fruit flies (thorax held at a position by a tether) were measured using a high speed camera. In the first subsection I go through the details of the flies and their preparation for the experiment. In the second subsection I explain the experimental procedure, data acquisition and preprocessing.

3.3.1 Fly rearing and preparations

Fly type and rearing

The fruit flies (*Drosophila melanogaster* Meigen) measured for the studies discussed in chapter 6 were obtained from the laboratory stock of Prof. Steven N. Fry, Institute of Neuroinformatics, ETH Zurich and University of Zurich, Switzerland. These flies descended from a wild-caught population of 200 mated females. Flies for the studies mentioned in section 6.3 were kindly provided by Prof. Dalibor Kodrík , Biology Centre of the ASČR, Institute of Entomology, České Budějovice, from their laboratory stock of canton-S flies. In both the batch of flies a standard breeding procedure was applied (25 females and 10 males, 12:12 hour light/dark cycle, standard nutritive medium). The experiments were performed during the first 6 hours of subjective day with 5-10 days old female flies.

Haltere ablation

In the batch of flies provided by Kodrík lab two sub-groups were maintained separately, one untreated and the other with both their halteres (section 1.4.3) ablated. To generate the group of haltere ablated flies, I selected 5 to 10 days old healthy (i.e. readily flying inside the rearing jar) female fruit flies and anesthetized them using CO_2. Each fly was then placed under a microscope with 10X magnification and both its halteres were surgically removed using a pair of pointed tweezers. Special care was taken not to injure the abdomen or the wings in this process. These treated flies were then given at least 12 Hrs to recover before

they were measured in the digital wingbeat analyzer and only flies flying uninterrupted for several minutes were measured.

Tethering

Each fly (both untreated and haltere ablated) was first immobilized in a refrigerator (4˚C) and transferred onto a custom built thermo-electrically cooled manipulation stage. The stage was kept as dry as possible and maintained at a temperature close to 4˚C by controlling the flow of water under it. The immobilized fly was then placed on a semi-spherical joint that allowed a precise adjustment of the fly body orientation. With a small drop of UV glue the fly's thorax was glued to the tether, using a UV light gun (ELC305, Electro-Lite Corp., Bethel, CT, U.S.A.). No fly was cooled for more than 10 minutes and every fly was allowed to recover for at least 30 minutes before measurements were conducted.

3.3.2 Experimental procedure and data preprocessing

Placing the fly in the digital wingbeat analyzer

The fly was then positioned in the digital wingbeat analyzer such that the wing stroke plane agreed with the camera plane as best as possible. However, unlike the wild type flies reared in Steven Lab INI Zurich, Canton S flies were slightly smaller in size and their stroke plane was such that the projection of the wings were often occluded by the projection of the tether during the dorsal reversal. These missing data points during the dorsal reversal phase of the wingbeat were later interpolated from the data points of the rest of the stroke. Before starting the measurements, the flies were allowed to rest on a piece of wet tissue for at least 30 minutes. The flight was then initiated by applying a puff of air on the fly. For each fly, several measurements of 1 minute length was performed, alternating with pauses of 1 minute. The number of recordings per fly varied from 3 to 5.

Measuring Drosophila wing motion in the digital wingbeat analyzer

For details of the data recording and its preprocessing please see section 2.1. Briefly, to measure the wing kinematics of tethered flying flies, a computer vision system with real-time analysis functionality (digital wingbeat analyzer—DWBA, SciTracks, Switzerland) was used. The system is based on a high-speed camera (Photonfocus, Switzerland) connected to a frame grabber card in a personal computer. The angular positions of the leading and trailing wing edges were tracked to obtain a robust estimate of the wing stroke position (i.e.

stroke angle). Using the DWBA, a sampling frequency of 3125 Hz was achieved for each wing, which at a wingbeat frequency of around 200 Hz corresponds to about 15 stroke position data points per wing stroke (spatial resolution 1°).

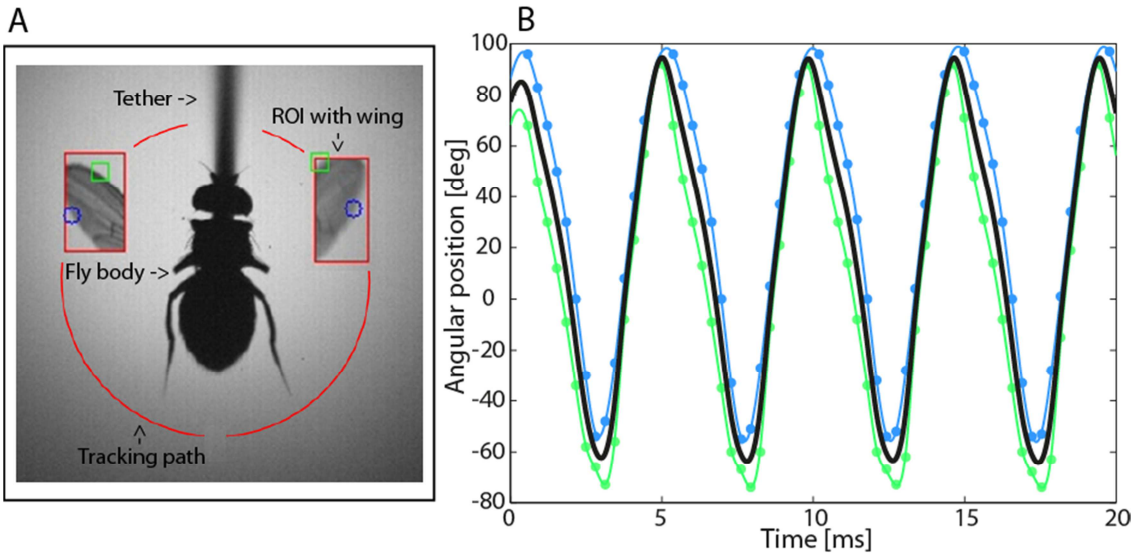

Figure 3.2: Wing tracking and data post-processing. A) Visualization of digital wingbeat analyzer (DWBA) functionality. Two consecutive frames of the dynamically updated region of interest (ROI, left and right wing), are shown overlaid on the mean image of the fly body and the tether. The DWBA detects and records (Graetzel et al. 2006) the leading (green squares) and trailing (blue dots) wing edge positions on a predefined tracking path (red circular lines). B) Data preprocessing. Recorded positions of the leading and trailing wing edge (green/blue dots) of a single wing are interpolated using B-splines (green/blue trace). The wing chord position (black trace) is obtained as the low-pass filtered mean of the interpolated positions of the two edges. For details see main text.

Data preprocessing

A suitable smoothing B-spline interpolation algorithm (Craven and Wahba 1978), (Matlab mex implementation by W. Dickson, parameter noise variance set to 3) was used to up-sample the leading and trailing wing edge data to a new sampling frequency of 50,000Hz. The center wing position was then calculated as the low-passed mean of leading and trailing wing edge positions (Matlab zero-phase digital filtering, 3rd order Butterworth filter with cut off frequency 1500Hz). For an example, refer to Fig.3.2.

Defining time series for analysis of the wing stroke

Most of the flight maneuvers are brought about by subtle changes in the wing motion (Fry et al., 2003; Muijres et al., 2014). To separately study the stoke modifications at individual phases of the stroke cycle I isolated the stroke angle at each given phase in a separate time series. I divided each stroke cycle from each wing into 8 temporally equidistant phase

points (Fig.3.3A) and the stroke angle at each of these phase points from consecutive stroke cycles constitute a time series. Hence, the time courses of the wing angular position at the selected 8 phase points were separated in 8 distinct time series (Fig.3.3B). A set of 16 time series (8 from each wing) thus, contain phase dependent information of the simultaneous cycle-by-cycle stroke deformations of the two wings. I considered only 8 phase points per wing as further increasing this number (within the limit of experimental sampling rate of ~15 per cycle) did not yield any new feature in the results, but considerably increased the computation time.

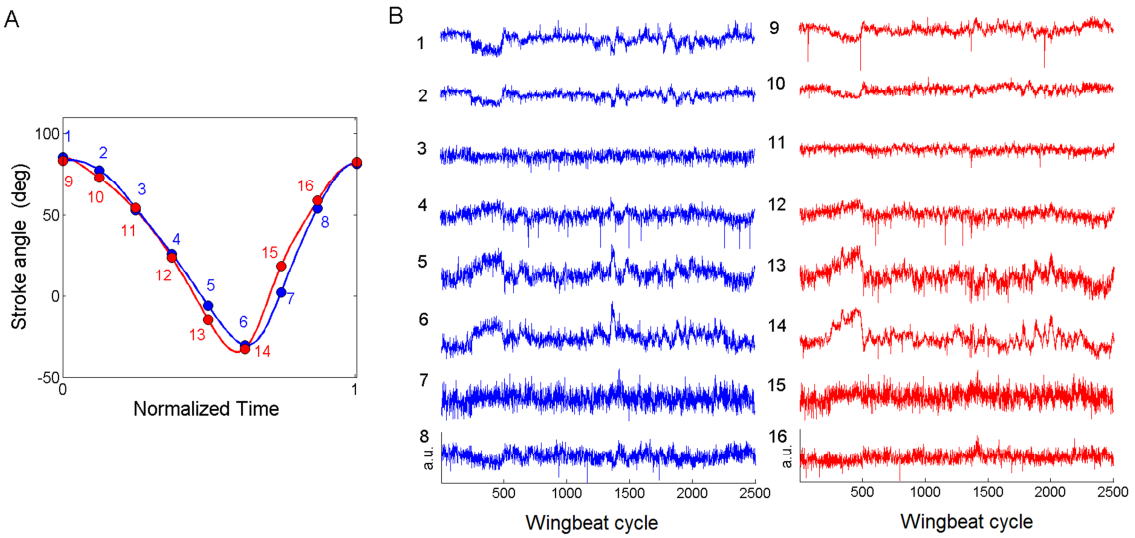

Figure 3.3: Definition of phase points and an example of their time course. A) One cycle of the stroke trajectory of left wing (blue) and right wing (red). The cycle is divided into 8 phase points sampled at equal time intervals; the angular positions of the two wings at these 8 phase points of the two wings define 16 time series. **B)** Time course of the 16 phase points during a flight segment of 2500 wing stroke cycles.

It is important to note that the procedure for constructing the 8 signals x_i results in the loss of information about the duration of each cycle. The signals x_i therefore reflect only variations in the waveform (shape) of the wing stroke, but not changes in the stroke duration / wingbeat frequency. In this analysis, I assess separately if the obtained least-dependent components of the stroke waveform are correlated (or uncorrelated) with the stroke period.

CHAPTER 4

Computational Methods

4.1 Overview

All the computational methods used during my research fall under the general category of time series analysis. A time series is a set of measured values x_t of any parameter x at time points t. Most of the time series that I have studied have periodic variations, as they represent rhythmic motion. Periodic signals are frequently characterized by the frequency domain parameters, like the spectral density, cross-spectral density and the coherence. The analyses methods discussed in the first and second subsections, namely the spectral density estimate and the coherence analysis, belong to the general category of stationary time series analysis. A stationary time series is the realization of a process whose statistical properties do not change with time, i.e. it can be described by the same probability distribution at each point of time. The processes which do not satisfy this property are called non-stationary processes and so are the corresponding time series. The analyses methods discussed in the third and fourth subsections, namely the wavelet spectral density and the wavelet coherence analysis, are methods used to study non-stationarity in time series. Other than these, an advanced statistical method for blind source separation was also used, namely independent component analysis. This method is discussed in the last subsection.

4.2 Spectral density

Spectral density function provides the fraction of the total variance of a signal in each frequency band. Transforming the representation of a variable from a time function (i.e. a time series) to a frequency function (i.e. spectral density) facilitates the identification of the dominant temporal structures in the time course of the variable. In any analysis involving periodic signals, like those representing rhythmic motion, it is essential to know its frequency spread. While, this is essential for periodic signals, even for non-periodic signals the frequency distribution provides information about the different time scales in the dynamics of the system generating those signals.

4.2.1 Statistical estimators and significance of the estimate

The periodogram is the simplest estimator of the spectral density. For a time series $\{X_t\}$ it is given by,

$$P(\omega_k) = \left| \frac{1}{\sqrt{N}} \sum_{t=0}^{N-1} \exp(i\omega_k t) X_t \right|^2 \quad ; \quad \omega_k = \frac{2\pi k}{N\Delta t}, \quad k = 0,1,\cdots N-1 \tag{4.1}$$

Where N is the number of time points measured, Δt is the sampling period and ω_k is the discrete frequency value. However, the spectral density estimated by the periodogram is not a good estimation of the true spectral density, especially for continuous spectra (Priestley, 2001, chapter 6). The inherent inconsistencies of the periodogram estimator are circumvented by estimating the spectral density using weighted integral of the periodograms as,

$$h(\omega) = \int_{-\pi}^{\pi} \mathrm{P}(\theta)\mathrm{W}(\omega - \theta)d\theta, \tag{4.2}$$

where, $\mathrm{P}(\theta)$ is the standard periodogram (Eq. 4.1) and $\mathrm{W}(\theta) = \frac{1}{2\pi}\sum_{s=-(N-1)}^{N-1} \lambda(s)e^{-is\theta}$ is the weight function obtained from the Fourier transform of the window function $\lambda(s)$.

Over decades a number of window functions with different properties have been defined (Brockwell and Davis 1991; Priestley 2001). In my study I used hamming window that is given by:

$$\lambda(s) = \begin{cases} 0.54 + 0.46\cos(\pi s/M), & |s| \leq \mathrm{M} \\ 0, & |s| > \mathrm{M} \end{cases} \tag{4.3}$$

The window function starts at 0.08, smoothly rises to 1 in the middle of the segment, and again smoothly goes down to 0.08 at the end. For details of the hamming window and other window functions used for spectral density estimates see (Brockwell and Davis 1991; Priestley 2001). A specific method of spectral density estimation that uses modified periodogram estimate is the Welch's method. In this method the entire time series is split into overlapping segments and their modified periodogram estimates are averaged to obtain the overall spectral density of the whole time series.

Even though using the window functions make the periodogram a consistent estimator of the spectral density function, the "goodness" of the estimator has to be judged by its asymptotic bias and variance. Bias of a statistical estimator is the difference between its expectation value and the true value of the parameter being estimated; while the variance is the spread of the estimated value of the parameter about the expectation value of the estimator. Although, the weighted averaged periodogram is an asymptotically unbiased estimator (i.e. when $\mathrm{N}\to\infty$), estimates for finite length data have significant biases (Priestley 2001). Such biases can be avoided to a large extent by using a window function $\lambda(s)$ that does not have sharp edges, for example the hamming window. In cases where the window function has discontinuities, for example in truncated periodogram, the bias error due to the periodogram estimation increases and needs to be corrected for. A well-studied method of bias correction in such cases is the "tapering" method. In this method the observed set of data $\{X_t\}$ is multiplied by an appropriate function h_t called a "taper" to

modify the data in a way so as to smooth out the discontinuities. An example of a taper function that was used in my study is the cosine taper, given by:

$$h_t = \frac{1}{2}\{1 - \cos(2\pi t/N)\}, \qquad t = 1, \cdots, N. \tag{4.4}$$

This function is also called the Hanning taper as it is closely related to the Tukey-Hanning window function (Priestley 2001). In fact any window function can be used as a tapper function by extending the window length to `the full length of the data set and shifting the function so that it attains its maximum midway through the data set.

It is however important to mention that the reliability and resolvability of the spectral estimate cannot be improved simultaneously (Grenander 1951). I.e. reducing the bias (increased resolvability) of the spectral estimate at a given frequency will invariably increase its variance (reduce reliability) at that frequency and vice-versa. The periodogram estimator is asymptotically unbiased, but its variance is the maximum at each frequency. While the weighted average periodogram reduces the variance at each frequency as compared to the periodogram, nevertheless it increases the bias. The asymptotic bias and variance values for different window functions have been tabulated in table 6.1 of (Priestley 2001). High bandwidth window functions constitute low variance estimators of spectral density (Grenander 1951). When data tapering is used in addition to windowing, the variance of the estimator is seen to increase as compared to when only untapered data is used. This is because tapering in a way reduces the effective total length of the data.

Below are the applications of spectral density estimate in the context of my studies of the rhythmic wing motion of fruit flies and the periodic hand motion of tremor.

4.2.2 Time scales of variations in stroke parameters and Wiener entropy

To study the timescales of variations at specific phases of the drosophila wingbeat, defined in section 3.3.2, during flight segments and its corresponding set of linearly transformed components (see section 4.6.2 and also chapter 6) I estimated Welch spectra using the MATLAB library function “pwelch” (version:7.11.0.584 (R2010b)) with 1024 window length and 50% segment overlap. Figure 4.1 shows the welch spectra of the 8 phase point signals shown in figure 3.2 (numbers designating each phase point is shown again in Fig. 4.1

for ease of referencing). Simple visual inspection of these time series (Fig. 3.2) reveals that the cycle-to-cycle changes in wing angles near the stroke reversals (i.e. phase points 1, 2, 5 and 6) have prominent features in the time scales of 10-100 wingbeat cycles; while those close to the mid-strokes (especially 3 and 7) are essentially featureless. A quantitative assessment of these features can be obtained from their spectral distributions (Fig. 4.1). Welch spectral density of phase points 1 and 6 (in case of this specific example) have a distinct characteristic, flat for high frequencies and gradually increasing at lower frequencies starting around 0.25 cycle^{-1}. This indicates that signals 1 and 6 are dominated by variations that last for 4 wingbeat cycles or longer. The spectral densities of the mid-stroke phase points 3 and 7 have distinctly different characteristics; signal 3 is mostly flat for frequencies higher than 0.3 cycle^{-1} and increase very little for lower frequencies; while the spectral density of signal 7 has even flatter topology. This indicates that the signals are essentially devoid of any features, other than the ones lasting for hundreds of wingbeat cycles. In terms of insect flight, such long lasting wing stroke variations may represent some gradual drifts during free flight, but not behaviorally interesting flight maneuver.

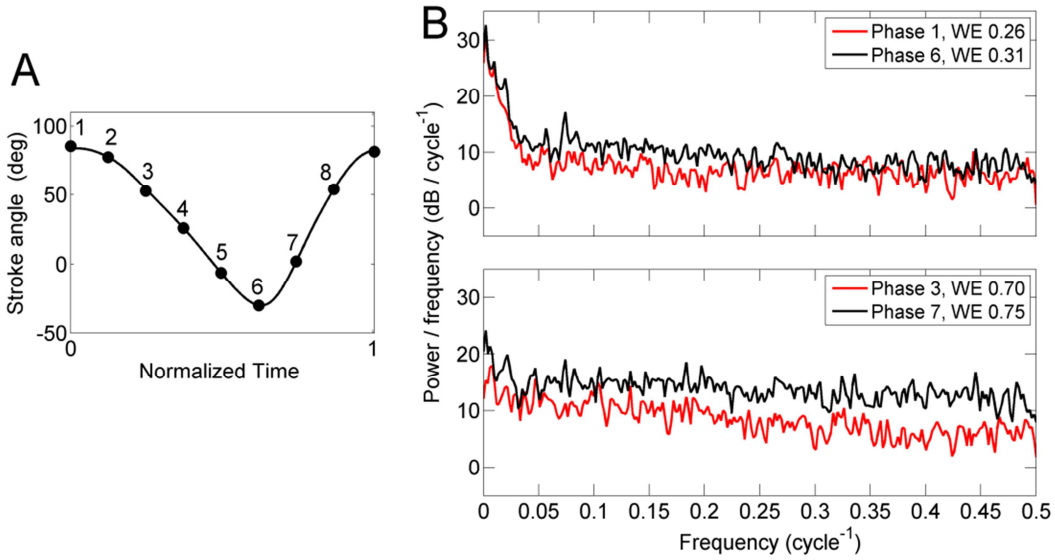

Figure 4.1: Frequency distributions of wing angle variations at specific phase points over the course of a flight segment. **A)** Stroke trajectory depicting the 8 phase points. **B)** Welch spectral densities of the wing angle variations over 2500 wingbeat cycles at specific phase points. Inset shows the respective WE values.

An important aspect in the analyses of *Drosophila* wing kinematics, for that matter in any signal processing, was to distinguish noise from the signal. For the reason stated above, a

time series devoid of any sustained temporal feature was considered to be noise. Distinguishing such time series from the ones with events of temporal variations is easier using frequency domain estimates, as the former is expected to have a flatter spectral distribution. Hence I used an estimate of the flatness of the spectral density function, called the Wiener entropy, to quantify the extent of temporal structure in a given time series. Wiener entropy (WE) is defined as the ratio of the geometric mean to the arithmetic mean of the spectral density. It ranges from 0 for sinusoidal waveforms to 1 for white noise. For the time series shown in Fig.3.2B, WE vary between 0.26 for phase point 1 and 0.75 for phase point 7. The welch spectral density plots of these signals are shown in Fig. 4.1 with their respective WE values. Low values of WE imply the presence of temporal features, as is also visually evident in Fig3.2B. For WE higher than 0.9, the spectrum is visually indistinguishable from a flat one. Examples of such noise like time series and their respective spectral density functions have been shown in Fig. 4.9, where this estimate has been used to classify time series as "noise like".

4.2.3 Frequency spread of hand tremor and estimation of tremor amplitude

A key feature that characterizes different types of tremor is the tremor frequency (section 1.5, table 1.2). Hence, the first step in any tremor analysis is to estimate the frequency content of the measured kinematic data. I used weighted periodogram method to estimate the spectral density of each component (a_x, a_y, a_z) of the linear hand acceleration measured in specific static postures (see section 3.2.2). Preprocessed time series (as mentioned in section 3.2.2) of each component of hand acceleration was divided into n_d disjoint segments of 1.28 sec (128 data points). The periodograms of these individual segments were then averaged to obtain the spectral distribution of the acceleration component for each subject in a given posture. Bias error introduced due to this splitting was corrected using the cosine tapper. The type 0 analysis of the freely available tool box NeuroSpec, version 2.0 downloaded from www.neurospec.com was used to estimate the weighted periodograms. Details of the estimation procedure can be found in (Halliday et al. 1995).

Estimation of tremor amplitude

The average hand displacements along individual axes were computed from the corresponding acceleration measurements. The spectral power of hand displacement at

each frequency was obtained by dividing the acceleration spectral power at that frequency by the fourth power of the frequency in radians. Average hand displacement was then calculated as the square root of the total spectral power of the hand displacement in the 2-15 Hz frequency range.

When evaluating the tremor amplitude directly from the measured acceleration, the gravitational artifact (Elble 2005) may lead to an error of order 10%. This error may be eliminated as in (Šprdlík et al. 2011) by decomposing the measured hand acceleration into gravitational artifact and inertial acceleration, based on an explicit reconstruction of the hand orientation. In the present study, I did not carry out this decomposition, and used the original recorded acceleration as the basis of all calculations. In addition to having a relatively low magnitude, the gravitational artifact is expected to have the same bilateral coherence (or lack of) as the inertial acceleration, as the time course of the oscillatory gravitational artifact follows the wrist motion (Elble 2005).

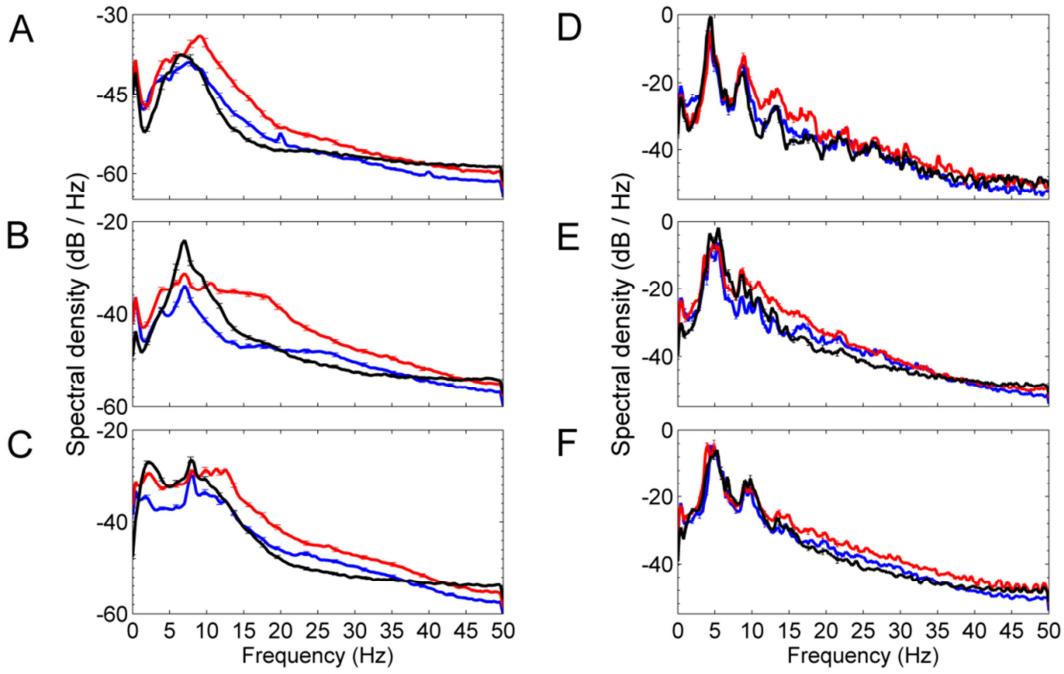

Figure 4.2: Average power spectra of hand accelerations. A-C) Spectra of x (blue), y (red) and z (black) components of hand acceleration measured in position 1 (A), 2 (B) and 3 (C) from 30 healthy subjects. **D-F)** Corresponding plots (as in A-C) for measurements from 34 ET patients.

4.3 Coherence

Coherence is the most commonly used statistic that quantifies the linear dependence between two time series as a function of frequency. For example, if two time series have multiple frequency components and only one of these components are linearly related (due to a common source or a common influence), then their extent of interdependence is best identified by coherence analysis.

4.3.1 Statistical estimators and significance of the estimate

An estimator that provides a measure of the relationship between two time series as a function of frequency is their cross-spectral density. Similar to the periodogram estimation of the auto-spectral density (Eq. 4.1), the cross-spectral density of two time series X(t) and Y(t) can be obtained as:

$$P_{XY}(\omega_k) = \frac{1}{N}\left(\sum_{t=0}^{N-1}\exp(i\omega_k t)X_t\right)\overline{\left(\sum_{t=0}^{N-1}\exp(i\omega_k t)Y_t\right)}; \quad \omega_k = \frac{2\pi k}{N\Delta t}, \ k = 0,1,\cdots N-1 \tag{4.5}$$

Where the bar represents complex conjugate operation, N is the number of time points measured, Δt is the sampling period and ω_k is the discrete frequency value. Like the periodogram, the cross-spectral density also needs to be smoothed (Eq. 4.2) to obtain a reliable estimate of the joint spectral distribution of two time series. This estimate is, however, sensitive to the spectral power of the individual signals at each frequency. I.e. Even if linear relationships of equal strength exist between the two signals at their principal frequency and a frequency where both the signals have low variance, the former will appear to be much stronger than the latter. Figure 4.3 shows two surrogate time series obtained by adding a common 30 Hz (middle row of Fig. 4.3A) time series to two sample hand acceleration time series (top and bottom row of Fig. 4.3A). The common signal was chosen to be of 30Hz as this frequency is far outside the main frequency band of the chosen hand acceleration time series (Fig. 4.3B). The cross-spectral density of the two surrogate time

series (estimated using hamming window with a time spread of 128 data points) shows three peaks (Fig. 4.3C), at 2Hz, 6Hz and 30Hz, indicating some level of mutual dependence at these frequencies. Even though the coupling between the surrogates at 30 Hz is by design at least as strong as the inherent ones at 2 and 6Hz, the cross-spectral density is much smaller at the former frequency. Hence, to obtain an unbiased estimate of the linear dependence, the cross-spectral density is normalized by the individual auto-spectral densities. The corresponding statistic called the magnitude squared coherence is thus estimated as (Bendat and Piersol 1986; Halliday et al. 1995):

$$\gamma_{XY}^2(\omega_k) = \frac{|S_{XY}(\omega_k)|^2}{S_{XX}(\omega_k) S_{YY}(\omega_k)}, \tag{4.6}$$

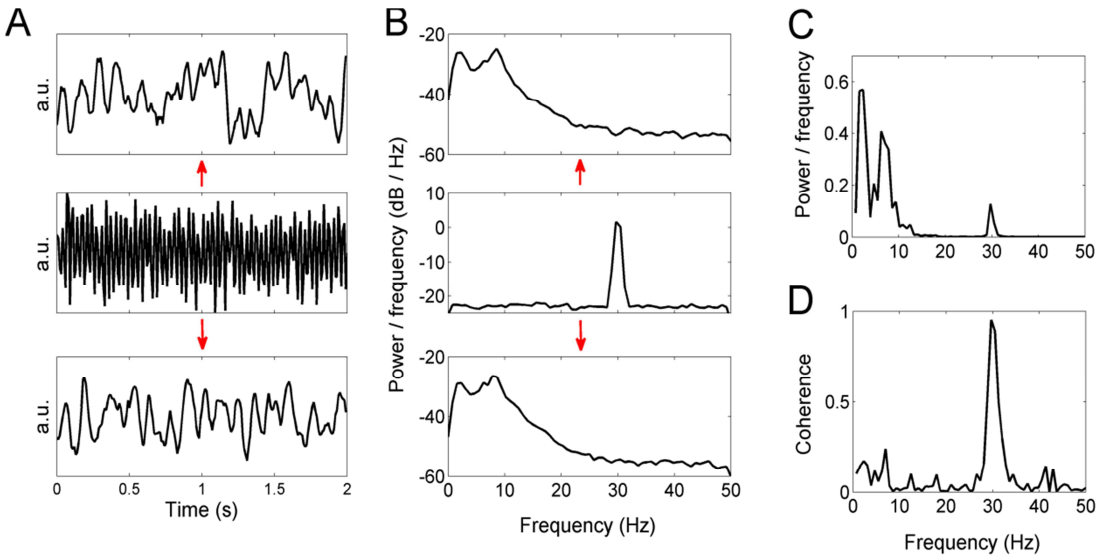

Figure 4.3: Auto-spectral density, cross-spectral density and coherence. A) Time courses of two sample time series (top and bottom sub-panels) and a surrogate time series constituting of a 30Hz sine wave and additive gaussian noise (middle sub-panel). **B)** Power spectral density of the corresponding time series shown in A. **C)** Cross-spectrum of the two sample time series (top and bottom sub-panels of A) with the surrogate time series (middle sub-panel) added to both. **D)** Coherence spectrum of the two sample time series (top and bottom sub-panels of A) with the surrogate time series (middle sub-panel) added to both.

Where, $S_{XY}(.)$ denotes smoothed cross-spectrum of the two time series and$S_{XX}(.)$, $S_{YY}(.)$ their smoothed auto-spectra. It is important to note that if the spectral densities are not smoothed, the coherence function is unity at all frequencies irrespective of the actual linear dependence between the two time series (Chapter 9, Priestley, 2001). From figure 4.3, it can

be seen that unlike the cross-spectrum (Fig. 4.3C) the coherence spectrum (Fig. 4.3D) convincingly brings out the strong linear dependence between the surrogates at 30Hz.

Estimation of confidence interval using surrogate data analysis

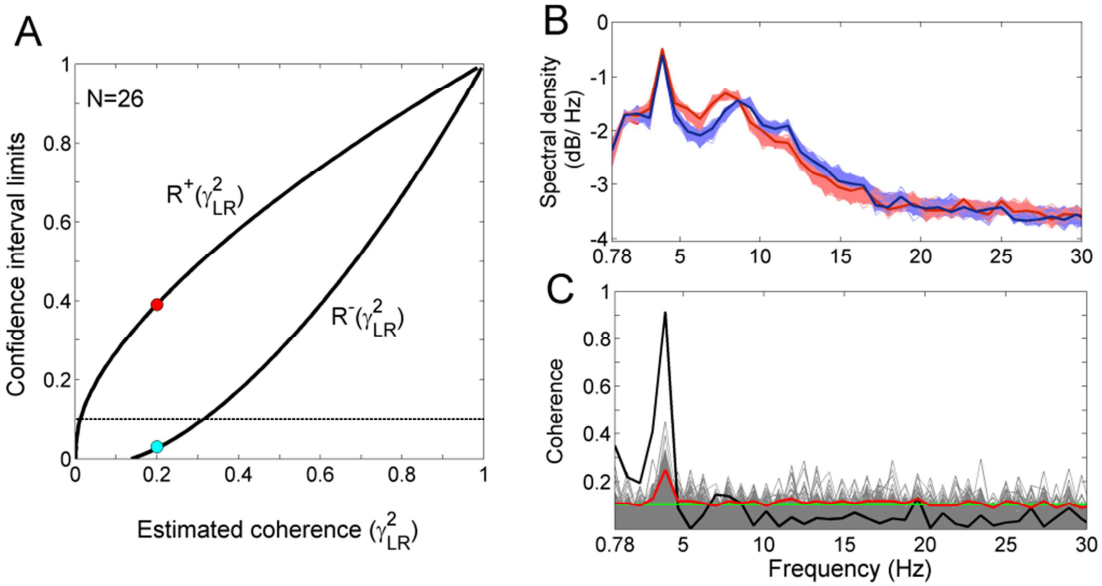

Figure 4.4: Confidence intervals and bias error. A) The solid black lines show the upper and lower limit of the 0.95 confidence interval of true coherence, given the estimated coherence value shown on the x-axis. Computed as in (Wang et al. 2004) for N=26. Dashed black line shows the coherence threshold E_I given by Eq. 4.7. **B)** Power spectral density of two sample time series (left (blue) and right (red) hand acceleration component measured from an ET patient) superposed on the power spectral densities of the 500 corresponding surrogate time series are plotted in faded blue and faded red. **C)** The black line shows the coherence spectrum of the measured acceleration (in B); gray lines show the coherence spectra of the 500 pairs of surrogate time series. The red line shows the 0.95 confidence threshold estimated from the surrogate coherence spectra. The green line shows the coherence threshold E_I from Eq. 4.7 (N=26).

To judge the significance of the estimated coherence value, it is customary to test it against the null hypothesis of zero coherence. I.e. given the parameters of coherence estimation (such as the number of disjoint segments etc.) what is the probability of obtaining a coherence value as high as that estimated, if the true coherence is zero? There are different methods of theoretically obtaining this probability, taking varied levels of details into account (Bendat and Piersol 1986; Halliday et al. 1995; Brillinger 2001; Priestley 2001). However, none of these methods take into account the frequency specific bias effects arising due to the finite length of the time series. Hence, to evaluate the bias in coherence estimation that can arise from sharp spectral peaks (for ET in my case) (Fig. 4.4B), I used surrogate data generated from the measured acceleration time series. The surrogate time

series have randomized Fourier phases, but preserve the power spectrum and the distribution of data values.

To obtain the surrogate data, I used the IAAFT algorithm introduced in (Schreiber and Schmitz, 1996). To begin, the original time series with N data points is randomly permuted to obtain a "seed" surrogate series that preserves the distribution of sample values but flattens the power spectrum. Two iterative steps are then repeated until the power spectrum of the starting time series is matched with the desired accuracy. In the first iterative step, the Fourier transform is computed, the magnitude of the Fourier coefficients is replaced by the magnitude of Fourier coefficients in the original time series, and the resulting Fourier series is back transformed. The time series so obtained has the same power spectrum as the original time series, but the phases are randomized. The second iterative step restores the original distribution of sample values. To do so, the time series produced by the first iterative step is rank ordered, and each sample value is replaced by the corresponding sample value in the rank-ordered original series. The resulting time series thus has the same set of sample values as the original time series. The power spectrum is perturbed by this operation, but the discrepancy can be reduced by repeating the two iterative steps. After the i-th iteration, the discrepancy in power spectrum is evaluated as

$$\Delta = \sum_{k=0}^{N-1} \left(\hat{S}_k^{(i)} - \hat{S}_k \right)^2 \Big/ \sum_{k=0}^{N-1} \hat{S}_k^2 \tag{4.7}$$

where $\hat{S}_k$ and $\hat{S}_k^{(i)}$ denote the smoothed power spectrum of the original and iterated time series, respectively. In our implementation, the algorithm was iterated until Δ smaller than 10^{-4} was reached, with smoothing window size of 21 points.

Fig. 4.4B,C shows an example of how the significance of a coherence peak is assessed using the surrogate data. In this example, the power spectra (solid lines in Fig. 4.4B) of the recorded acceleration time series from both hands have a sharp peak near 4 Hz. The coherence spectrum of the recorded series (black line in Fig. 4.4C) shows a pronounced peak near 4 Hz. To assess its statistical significance, I generated 500 pairs of surrogate time series and computed their coherence spectra. Each surrogate pair was generated starting from the measured left and right hand accelerations by the IAAFT algorithm as described above, with different random permutations in the initial step. The power spectra of all the

surrogates are plotted as faded lines in Fig. 4.4B, confirming their closeness to the original power spectra. The coherence spectra computed from the 500 surrogate pairs are shown as gray lines in Fig. 4.4C. The red line corresponds to the 95% percentile of these coherence values; this gives the coherence threshold for rejecting the null hypothesis of zero coherence at the 0.05 significance level. The magnitude of the peak in the coherence spectrum of the recorded series (0.9) exceeds the surrogate-derived threshold (0.25), and the coherence at 4 Hz in this example is thus statistically significant.

4.3.2 Bilateral coherence of left and right hand acceleration

To assess the linear dependence between the accelerations of the two hands I studied their coherence spectrum. The statistical significance of the estimated coherence value (Eq. 4.6) was assessed by comparing it to a threshold value, which was obtained using the following criteria. The most commonly used (Lauk et al. 1999; Timmer et al. 2000b) coherence threshold to reject the null hypothesis of zero coherence is given by (Halliday et al. 1995):

$$E_{\mathrm{I}} = 1-(1-0.95)^{1/(N-1)}, \tag{4.8}$$

and corresponds to the value below which 95% of the distribution of coherence estimates will lie when the true coherence is zero. In our case E_I varies from 0.09 (for N=32) to 0.11 (for N=26). Instead of E_{I}, however, I used a more stringent threshold, corresponding to the criterion defined in (Wang et al. 2004). It is based on evaluating the 95% confidence range of the expected true coherence values, given the estimated coherence value γ^2_{LR}. Fig. 4.4A shows the upper limits $R^+\left(\gamma^2_{\mathrm{LR}}\right)$ and the lower limits $R^-\left(\gamma^2_{\mathrm{LR}}\right)$ of this range, calculated for $\mathrm{N}=26$ as in (Wang et al. 2004). For example, a coherence value of 0.2 obtained using Eq. 4.6 would imply a true coherence magnitude in the range 0.03-0.4 with 95% confidence (Fig. 4.4A). If only γ^2_{LR} but not $R^-\left(\gamma^2_{\mathrm{LR}}\right)$ is above the threshold E_{I}, then according to (Wang et al. 2004) the two signals are not statistically independent, but their linear dependence is not sufficiently confirmed. Only the estimated coherence values that are above 0.3 satisfy the condition of $R^-\left(\gamma^2_{\mathrm{LR}}\right) > E_{\mathrm{I}}$ for $\mathrm{N}=26$ (hence will also satisfy this condition for $\mathrm{N}>26$, see Fig. 3 in (Wang et al. 2004)). The threshold E_{I} was therefore by the higher threshold of 0.3.

When the two time series have sharp spectral peaks at overlapping frequencies (which is typically the case in ET), the errors in the estimation of spectral densities in Eq. 4.6 may additionally bias the distribution of coherence estimates (Bendat and Piersol 1986; Faes et al. 2004). I used the method of surrogate data analysis to evaluate this bias. For each pair of recorded acceleration time series, a set of 500 pairs of mutually independent surrogate time series were constructed that preserved the power spectrum of the recorded series (see previous subsection). The distribution of coherence values in this set was computed and the 95% percentile level extracted. For surrogate data sets constructed from ET recordings, this coherence level reached as high as 0.39 near the main tremor frequency, while for the PT-based surrogate data it generally remained consistent with Eq. 4.8.

Based on these considerations, I chose the following thresholds that must be exceeded to declare statistically significant coherence: 0.3 for the physiological tremor recordings and 0.4 for the ET recordings. These thresholds are stricter than the most commonly used threshold for rejecting zero coherence, given by Eq. 4.8. The higher thresholds used in this study minimize the chance of false positives, but may underestimate the prevalence of coherence at frequencies outside the main tremor frequency band.

4.3.3 Partial coherence between left and right hand acceleration

The partial coherence (Bendat and Piersol 1986; Halliday et al. 1995) is a statistic used to assess how much of a linear dependence between two signals can be explained by their shared dependence with a third signal. Low values of partial coherence imply that the coherent component between the first two signals can be predicted based on the knowledge of the third signal.

To assess the linear relationship between the left and right hand tremors in absence of any contributions of the balistocardiac oscillations and torso movements, I estimated their partial coherence under the imposed condition of no chest motion as (Bendat and Piersol 1986; Halliday et al. 1995):

$$\gamma^2_{XY.Z}(f) = \frac{|S_{XY.Z}(f)|^2}{S_{XX.Z}(f)S_{YY.Z}(f)} \tag{4.8}$$

The indices X, Y and Z indicate the left hand, right hand, and chest wall acceleration, respectively. The index after the dot (".") denotes the time series whose influence on the other two time series has been subtracted. It can be seen that the expressions for the ordinary coherence (Eq. 4.6) and the partial coherence (Eq. 4.8) are same except that the auto and cross-power spectrum (i.e. $S_{XX}(f)$ and $S_{XY}(f)$ respectively) in the former are replaced by the corresponding conditioned (or partial) spectral density functions ($S_{XX.Z}(f)$ and $S_{XY.Z}(f)$) in the later. The conditioned spectral density functions are estimated from the ordinary spectral density functions as (Bendat and Piersol 1986),

$$S_{XY.Z}(f) = S_{XY}(f) - \left(\frac{S_{XZ}(f)}{S_{ZZ}(f)}\right) S_{YZ}(f) \tag{4.9}$$

Using the expression of equation 4.9 in equation 4.8 one obtains,

$$\gamma^2_{ij.k} = \frac{\left|S_{YX}(f)S_{ZZ}(f) - S_{YZ}(f)S_{ZX}(f)\right|^2}{\left(S_{YY}(f)S_{ZZ}(f) - \left|S_{YZ}(f)\right|^2\right)\left(S_{XX}(f)S_{ZZ}(f) - \left|S_{XZ}(f)\right|^2\right)} \tag{4.10}$$

(Bendat and Piersol 1986; Albo et al. 2004). Eq. 4.10 was used to estimate the partial coherence between each component of the left and right hand acceleration subtracting the influence of the chest motion. The spectral density functions were estimated using the type 0 analysis of the NeuroSpec 2.0 toolbox. Like the ordinary coherence estimate, partial coherence values also range from 0 to 1. Zero partial coherence at a particular frequency implies that either there is no linear relationship between the two hands at that frequency or the existing relation can be completely attributed to the chest motion.

The coherence threshold of Eq. 4.8 can be generalized to the case of partial coherence by replacing N by $N - r$, where r is the number of predictors under consideration (Halliday et al. 1995). As in our case, N=26-32 and r=1, these two thresholds are practically identical (and equal to 0.09-0.11). A more stringent threshold of 0.3 (see previous subsection) was used to reject the null hypothesis of zero partial coherence in PT recordings.

4.4 Wavelet spectral density

The spectral density estimation, as discussed in section 4.2, provides information only about the time averaged frequency content of a time series while the time evolution of the frequency components remains obscured. This is because in Fourier transform the time series is convolved with an infinite sinusoidal wave $\kappa = e^{-i\omega_0 t}$ that is not localized in time. Windowed Fourier transform overcomes this limitation by using a modified kernel, $\kappa = g(t-\tau)e^{-i\omega_0 t}$ where $g(t-\tau)$ is an envelope function that localizes the sinusoidal wave around the time point. However, this transform too suffers the limitation of having a constant time and frequency resolution throughout the time-frequency space. Hence a window function that better resolves temporally transient events performs poorly in separating time-overlapped frequency components, and vice-versa. To this end, a method that has been successfully used to identify both the time of occurrence and the magnitude of transiently appearing frequency components is the wavelet transform. In this transform the time-frequency resolution is varied in such a way that the frequency resolution is higher in the low frequency range and the time resolution is higher in the high frequency range (Daubechies 1992; Torrence and Compo 1998a; Mallat 1999). There are two classes of wavelet transforms; the continuous wavelet transform (CWT) and the discrete wavelet transform (DWT). The DWT is used commonly for generating a compact representation of data as it is particularly useful for noise reduction and data compression. I chose to work with CWT as it is better for feature extraction. In the rest of this section I will first mention the statistical estimator of the continuous wavelet spectral density and the estimation errors that it entails, followed by the numerical method I used to determine the significance of the estimate. In the end I discuss how this method was used to identify transiently occurring frequency components in the ventral amplitude time series of the fly wing motion. Throughout this thesis wavelet transform always implies CWT.

4.4.1 Statistical estimator and significance of the estimate

In wavelet analysis the time series is convolved with a set of functions known as daughter wavelets $\psi^{a,b}$, obtained by scaling and translating in time a temporally localized kernel called the mother wavelet ψ_0. Hence the daughter wavelets are defined as,

$\psi^{a,b} = a^{1/2}\psi_0\left(\frac{\eta - b}{a}\right)$, Where a=dimensionless scaling factor, b=translation in time. (4.11)

One of the simplest and widely used wavelet is the complex Morlet wavelet. The complex Morlet wavelet is a plane wave modulated by a gaussian envelope:

$$\psi_0(\eta) = \frac{1}{\sqrt{\pi F_b}} e^{2\pi i F_c \eta} e^{-\eta^2/2} \quad (4.12)$$

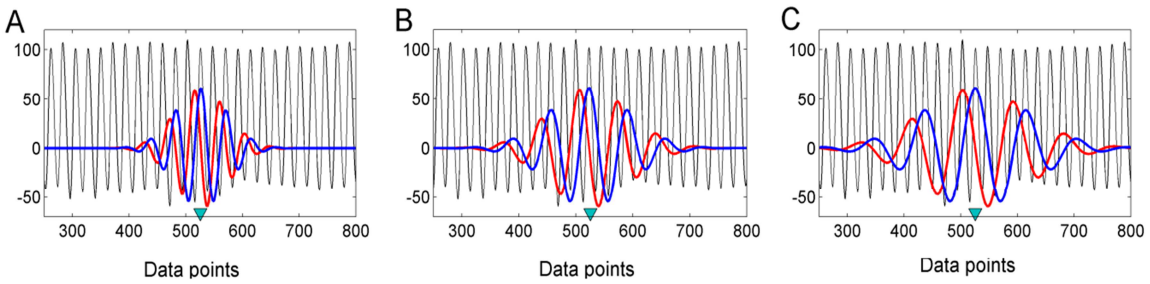

Figure 4.5: Morlet wavelet transform. Real (blue) and imaginary (red) parts of complex Morlet wavelet with pseudo frequency of 100 Hz (A), 66Hz (C) and 50Hz (E) superposed on a periodic time series of 200Hz. All three wavelets are centered at the same time point marked by a cyan arrow on the x-axis.

Where F_c is the central frequency of the mother wavelet and F_b is the band width parameter. It can be seen that scaling (Eq. 4.11) the mother wavelet (Eq. 4.12) dilates the central frequency F_c; hence each daughter wavelet with a separate scaling factor 'a' has a different central-frequency. This frequency is denoted as the pseudo-frequency of the daughter wavelet. Figure 4.5 shows the real (blue) and imaginary (red) parts of three daughter-Morlet wavelets with different scaling factors superposed on a periodic signal. The scaling factors of the daughter-wavelets shown in subplots A, B and C are such that their pseudo-frequencies are 1/2, 1/3 and 1/4th of the natural frequency of the periodic signal, respectively. All the three daughter wavelets shown are localized at the same time point, marked by the cyan arrow on the x-axis in each case. Convolution of the daughter wavelet in equation 4.12 with the wingbeat time series gives the wavelet coefficient at the time point b for the respective scale a, i.e.

$$W[f(a,b)] = \int_{-\infty}^{\infty} f(t) \frac{1}{\sqrt{a}} \psi_0 \left(\frac{t-b}{a} \right) dt \qquad (4.13)$$

Estimation of the confidence interval by surrogate data analysis

To determine the significance of the wavelet coefficients, first it is necessary to choose an expected background spectrum. In my case I used wavelet spectra to obtain transiently occurring periodic variations in the ventral amplitude time series of the fly wing motion. For a fly flying on tether, there is no predisposed temporal structure of the ventral amplitude variations and hence I chose the expected background time series to be a white noise, i.e. without any temporal structure. For each segment of the time series analyzed, the background white noise was obtained by randomly reshuffling the time axis. Depending on the length of the analyzed time series, as many white noise time series were generated as required to get a total length of 10^6 time points. The background time series of 10^6 time points was analyzed using the same daughter wavelets as the original time series. These 10^6 wavelet coefficients for each daughter wavelet provide a complete distribution of the coefficient values for random variations at that scaling factor. From this distribution, the magnitude corresponding to (1- α) percentile is selected as the threshold for hypothesis testing of no periodic variation, at α significance level. Hence, if the magnitude of the wavelet coefficient at a given time point is higher than this threshold, it can be inferred with (1- α) % confidence that the periodic variation encompassing that time point has not occurred by chance. The theoretical basis underlying this numerical method of determining the significance level of the estimated wavelet coefficients can be found in (Torrence and Compo 1998a).

4.4.2 Identification of intervals of *Drosophila* wing motion with subharmonic ventral amplitude variations

Power spectra of the ventral amplitude time course in many flight tests show a broad but distinct peak in the frequency range 0.25 to 0.35 $cycle^{-1}$, while in some other cases there is considerable increase in power from 0.4 to 0.5 $cycle^{-1}$. The former indicates the presence of transient 3-4 cycle periodic variations and the later the presence of transient 2 cycle periodic variations in the time course. To study the pattern of occurrences of these sub-harmonic variations in the ventral amplitude time series of the two wings, I used complex

Morlet wavelet transform to identify transiently occurring episodes of 0.5, 0.33 and 0.25 pseudo-frequencies (corresponding to 2, 3 and 4 wingbeat cycles respectively). For this estimation I used the standard library function for continuous wavelet transform (i.e. cwt) available in MATLAB 7.11, R2010b, with parameter values F_b=3 and F_c=1 for the mother wavelet (Eq. 4.12). Also, since only the high frequency variations are of interest, the ventral amplitude time series was high pass filtered with a lower cutoff frequency of 0.02 $cycle^{-1}$ (filter: idealfilter from MATLAB 7.11, R2010b). The Morlet wavelet coefficients of a segment of ventral amplitude time series for each of these three scaling factors are shown in figure 4.6 A, C and E. High values of the coefficients at any time point imply variations with the pseudo frequency of the corresponding daughter wavelet at that time point. The significance of the coefficient values was judged using surrogate data analysis, as described in the last part of the previous subsection. For the first two scaling factors (i.e. the ones corresponding to pseudo-frequencies 0.5 and 0.33) the threshold coefficient value was obtained for 0.01 significance level (i.e. α value). Hence, if the magnitude of the wavelet coefficients for these two scaling factors at a given time point is higher than the threshold, it can be inferred with 99% confidence that the 2 or the 3 cycle periodic variation has not occurred by chance. In case of the third daughter wavelet (i.e. the ones with pseudo-frequency 0.25), the threshold had to be increased in order to circumvent the broader peaks (result of decreasing time resolution) occurring due to abrupt changes in the time series. In this case the threshold coefficient value was obtained for 0.001 significance level. The red dashed lines in Fig. 4.6 A, C and E mark the threshold for each scaling factor obtained for the analyzed segment of the ventral amplitude. To further ensure that we extract intervals with persistent periodic variation and not random fluctuations, we considered only those intervals as events that last longer than 3 times the characteristic periodicity. I.e. the 2 cycle periodic events must last for at least 7 strokes, 3 cycle periodic events at least for 10 strokes and 4 cycle periodic events for at least 13 strokes. Green and red arrows in Fig. 4.6 A, C and E indicate the beginning and the end of the events which are finally extracted using the above algorithm and saved in the database for further analyses. The corresponding segments of the ventral amplitude time course are shown in Fig. 4.6 B, D and F. Red circles marking the ventral amplitude of the individual strokes are joined by black dashed line so as to enhance the visualization of the intermittent periodic variations in each case. The intervals of ventral amplitude time course selected as events by the algorithm (bound by the green and red arrows in subplots A, B and C) are highlighted using gray background.

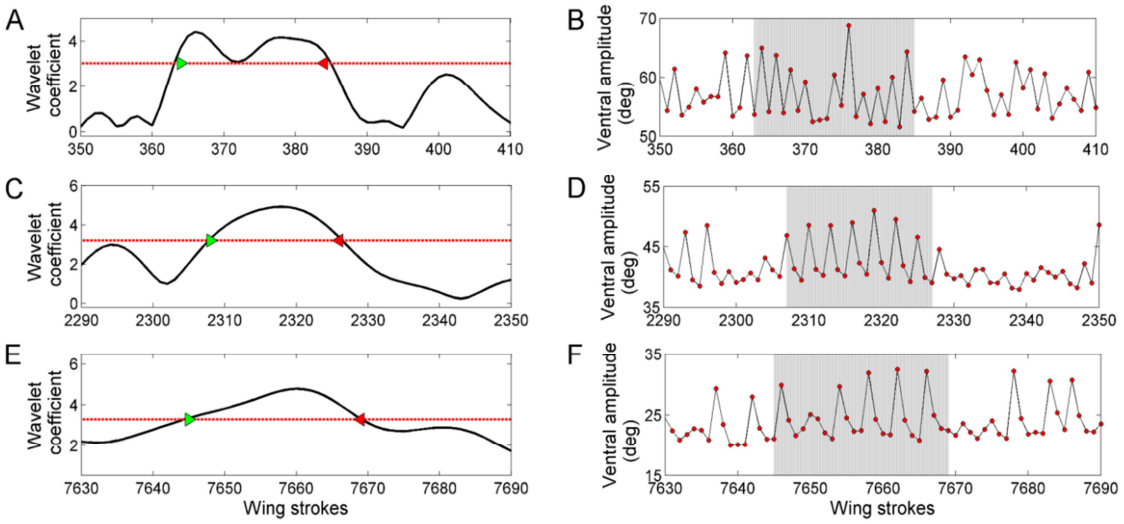

Figure 4.6: Morlet wavelet transform of ventral amplitude time series and extraction of intervals with transiently occurring periodic variations. (A, C, E) Magnitude of the complex Morlet wavelet coefficient of ventral amplitude time series, at scale values with pseudo-frequency of 0.5 cycle^{-1} (A), 0.36 cycle^{-1} (C) and 0.25 cycle^{-1} (D) (black solid line). Red dashed line shows the threshold coefficient value above which the periodic variation can be considered to have not occurred by chance (see main text for details). Green arrow marks the beginning and red arrow the end of an event of the periodic variation. **(B, D, F)** Ventral amplitude time courses during the specific intervals shown in the left panels. Red dots indicate individual strokes. The events marked by the green and red arrows in the left set of panels (i.e. A, C and E) are highlighted by a grey background in the corresponding right panels (i.e. B, D and F).

4.5 Wavelet coherence

Wavelet coherence estimate is the non-stationary analogue of the Fourier transform based coherence estimate. The basic method of time-frequency binning underlying wavelet transform enables wavelet coherence analysis to identify intermittent linear couplings between two time series. In this subsection I will first discuss the estimation of wavelet coherence

4.5.1 Statistical estimator and significance of the estimate

Like its Fourier transform analogue, wavelet coherence is also estimated from the wavelet cross-spectra of the two time series in concern. Like the Fourier cross spectrum the magnitude of the wavelet cross spectrum gives an estimate of the joint power of the two time series at a particular frequency, and in addition it also provides the distribution of this power in time. While the phase of the wavelet cross-spectrum quantifies the relative phase of a given frequency component (corresponding to the wavelet scales) of the two time series at each time point (b). Magnitude of the cross wavelet spectrum normalized by the wavelet spectrum of the two time series gives the wavelet coherence. Again like its Fourier counterpart (Eq. 4.6) wavelet coherence gives a measure of the linear dependence between the two time series at each scale and each time point.

For the wavelet cross-spectral and coherence analyses I used the Wavelet coherence MATLAB package from www.glaciology.net/wavelet-coherence, with a complex Morlet wavelet (Grinsted et al. 2004). The wavelet coherence in this toolbox is estimated as,

$$\gamma_{ij}^2(a,b) = \frac{\left|S\left(a^{-1}\mathrm{W}_{ij}(a,b)\right)\right|^2}{S\left(a^{-1}\left|\mathrm{W}_i(a,b)\right|^2\right).S\left(a^{-1}\left|\mathrm{W}_j(a,b)\right|^2\right)} \tag{4.14}$$

Here, S is a smoothing operator acting both along the scale (a) and the time (b) variable (Torrence and Compo 1998b). Along the time axis the smoothing was done using a scale

dependent low pass filter and that along the scale axis was done using a box car function of width 0.6. Further details regarding the smoothing operator can be found in the original article related to this package (Grinsted et al. 2004). Figure 4.7 B,D show the magnitude of the wavelet cross-spectrum and the wavelet coherence of two time series. Note that the wavelet cross-spectrum has highest magnitudes in the frequency range 4-10 Hz, indicating this frequency range is dominant in both the analyzed time series; as is also shown by their individual spectral density plots (Fig.4.7A). Interesting information regarding the two time series brought out only by this non-stationary analysis is: while the frequency components close to 8Hz are a consistent component of the two time series, the ones close to 4Hz appear only transiently. Interestingly the interaction between the two time series seems to be restricted only in the latter (2-4Hz) frequency range, as seen from the wavelet coherence spectrum (Fig.4.7D). While the extent of mutual interaction between the time series is also implied by the significant coherence peak at 3.1Hz (Fig.4.7C), but only the wavelet coherence spectrum reveals that this interaction appears only transiently.

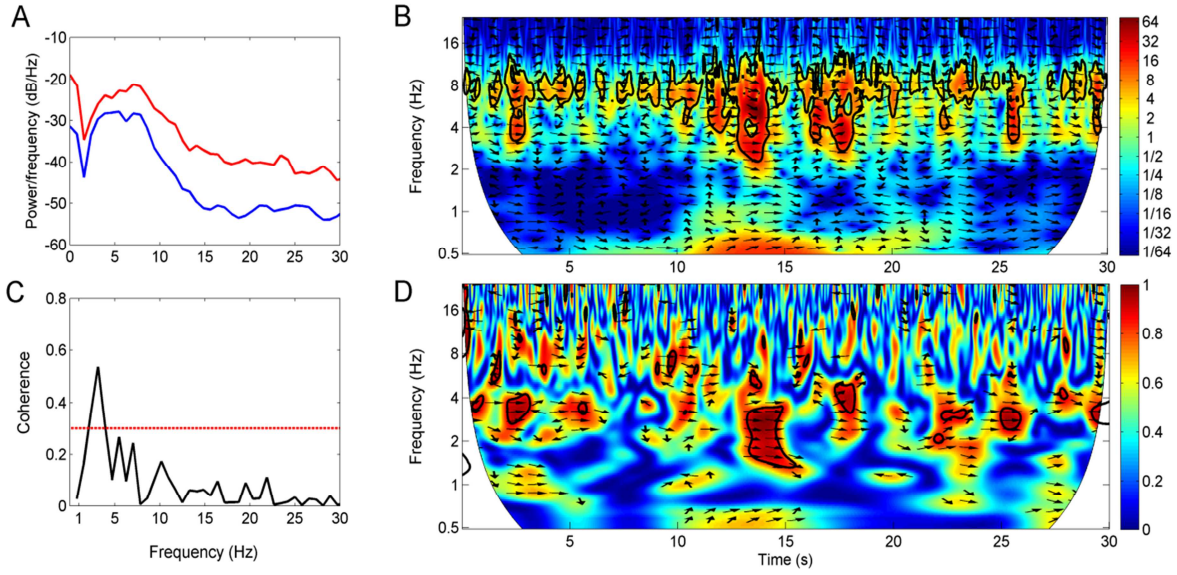

Figure 4.7: Correspondence of Fourier transform and wavelet transform based cross-spectral density and coherence estimations of two sample time series. A) Welch power spectra of the two time series. **B)** Wavelet cross-spectrum. **C)** Coherence spectrum. **D)** Wavelet coherence. Black arrows in both B and D panels show the relative phases of the two time series at the respective scale factors and time points. Right arrow indicates an in-phase interaction while left arrow indicates a phase lag of 180˚ of the second signal w.r.t the first. Other arrow directions are calibrated accordingly with the intermediate phase angles.

Estimation of the confidence interval by surrogate data analysis

The statistical significance of both the wavelet cross spectra and the wavelet coherence estimates was assessed using the method of surrogate data, as in the case of their stationary counterparts discussed above in section 4.3.1. Pairs of mutually independent time series with the same power spectral densities as the analyzed pair of time series was used to provide the expected background of the estimates. For this part I had to modify the package designed for wavelet coherence estimate by (Grinsted et al. 2004), so that when evaluating the zero coherence for the null hypothesis mutually independent surrogate time series of the two hands were used, instead of the red noise used by default in this package. This modification was necessary because the wavelet coherence package was developed for studying the linear relationship between non-periodic geological time series (like Arctic oscillation index and the Baltic maximum sea ice extent). But the time series that I studied are periodic oscillations, far from red noise in their spectral properties. Also the studied pair of time series almost always have largely overlapping frequency ranges, hence at the scales corresponding to these common frequencies it is more probable to find phase locked intervals purely by chance. This makes it important to use a scale dependent coherence threshold.

I generated 300 mutually independent pairs of surrogate time series (typically 4000 to 5000 time points) having the same amplitude distribution and power spectral density as the hand acceleration components (IAAFT algorithm, as described in Sec. 4.3.1). Wavelet coherence spectra of these surrogates were then calculated to obtain a distribution of the coherence estimates for zero true coherence at each scale. The 0.05 significance level of the statistical test was then set at the 95 percentile of the coherence distribution at each scale. In both the panels in Fig.4.7 the black contours mark the regions with values above 0.05 significance level, and the arrows show the relative phase between the two signals at the designated scale and time point.

4.5.2 Identification of transiently occurring coupling between hand acceleration

For all recordings with significant magnitude squared coherence (MSC) (Eq. 4.6) between the left and right hand acceleration components, wavelet coherence was analyzed. To

extract the time intervals of significant coherence, the following procedure (illustrated with the help of an example in Fig.4.8) was used:

i. For each significant coherence peak (as defined in section 4.3.2) in the MSC spectrum, the corresponding wavelet scale and its time-frequency spread was estimated. For the daughter Morlet wavelets used for coherence estimation in this study the time frequency widths at scale factor "a" are $1.11\,a^{-1}$ and $0.74\,a$ respectively (Addison 2002). Figure 4.8A shows the MSC function of the z-components of the left and right hand accelerations of an ET patient. In this example, the significant coherence peak is at 4Hz. The frequency band highlighted in grey marks the 2.3-5Hz frequency spread of the daughter wavelet with pseudo-frequency of 4Hz.

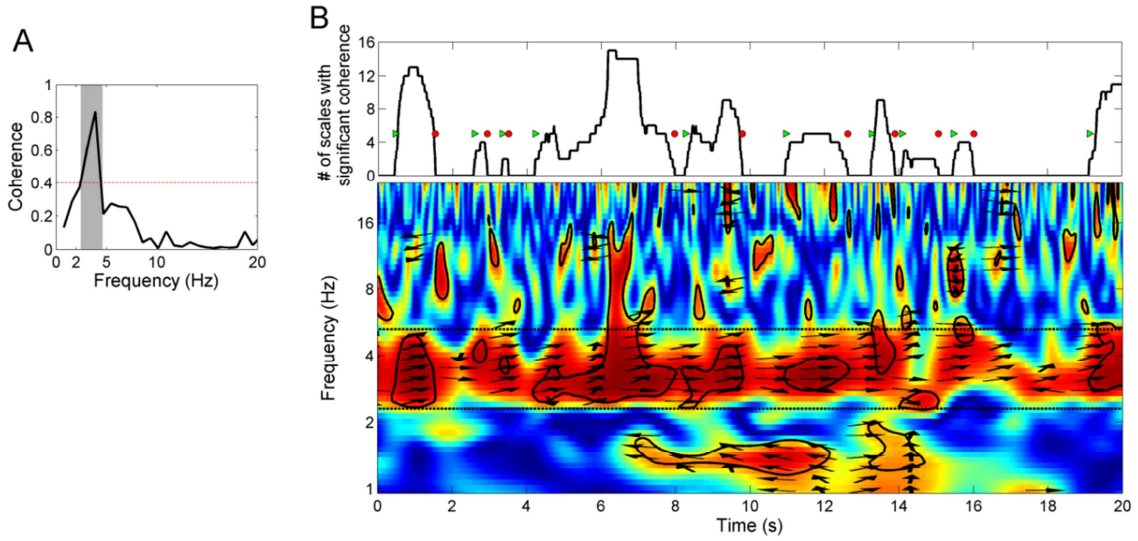

Figure 4.8: Extracting intermittent events of bilateral coupling of hand acceleration. A) Magnitude squared coherence plot of the left and right hand accelerations (z-component) of an ET patient. **B) Upper panel:** Graph of the number of scales (within the frequency band marked by dashed lines in the lower panel) with significant wavelet coherence at each time point. **Lower panel:** Wavelet coherence plot of the left and the right hand acceleration components. Black contours mark the regions of 95% confidence interval for the rejection of the null hypothesis of zero wavelet coherence, and the arrows indicate the relative phase between the two signals at the designated time-frequency point. Black dashed lines mark the frequency width of the daughter Morlet wavelet with pseudo-frequency same as the coherent frequency of the two signals.

ii. The wavelet scales corresponding to the frequency spread of the daughter wavelet (marked by black dashed lines in the bottom panel of Fig.4.8B) were scanned for intervals of significant (see previous section) wavelet coherence. The graph in the upper panel of Fig.4.8B shows the number of scales in this band with significant

wavelet coherence at each time point. The beginning and the end (green arrows and red dots, Fig 4.8B upper panel) of these intervals were extracted.

iii. If the duration of the interval exceeded the time width of the daughter wavelet (~0.2s in this example) and the coherence extended over a scale range exceeding 50% of the frequency width of the wavelet, the interval was counted as a coherence event.

However, it is important to note that short coherence events may arise as false positives: as the significance level for rejecting null coherence at each time-frequency point is finite, there is a finite probability of finding coherence events in a pair of non-coherent signals. To characterize the durations of such "false events", I used the algorithm described above to extract the intervals of significant coherence in pairs of statistically independent surrogate signals. For each measured pair of hand acceleration time series, 50 surrogate pairs were generated, and the scales corresponding to the coherent frequencies of the original signal pair were scanned for the false events. The median durations of these events ranged from 0.4 sec (for surrogates corresponding to position P3 in ET subjects) to 1.1 sec (for surrogates corresponding to position P2 in PT subjects). The 95th percentile durations (i.e., durations reached by only 5% of false events) ranged from 2.2 sec to 3.1 sec.

4.6 Independent component analysis

Independent component analysis (ICA) is a computational tool that transforms a set of interrelated signals into a set of their component signals that are mutually statistically independent (Hyvarinen et al. 2001). Before going into further details of the mathematical model and the algorithms used to implement it, it is important to understand the concept of statistical independence and its difference from uncorrelatedness. Two random variables (or signals) x_1 and x_2 are said to be statistically independent if the knowledge of x_1 does not provide any information about x_2 and vice-versa. In statistical terms, the probability of occurrence of a given value of x_1 remains the same irrespective of whether the value of x_2 is known or is unknown. I.e. the conditional probability $P(x_1|x_2)$ is same as the marginal probability $P(x_1)$. Hence, the joint probability density of these two signals:

$$P(x_1, x_2) = P(x_1|x_2)\mathrm{P}(x_2) = P(x_1)\mathrm{P}(x_2) \quad (4.15)$$

Therefore, one can define independent variables (or signals) as the set of variables whose joint probability density is factorizable into their marginal probability density functions, i.e.:

$$P(x_1, x_2 \cdots x_n) = P(x_1)P(x_2)\cdots P(x_n) \quad (4.16)$$

On the other hand, two random variables are said to be uncorrelated when their covariance is zero. i.e., $E\{(x_1 - E\{x_1\})(x_2 - E\{x_2\})\} = 0$;

$$\Rightarrow E\{x_1x_2\} - E\{x_1\}E\{x_2\} = 0, \quad (4.17)$$

Where $E\{.\}$ is the expectation operator. It can be shown easily that while condition presented in Eq. 4.15 automatically implies Eq. 4.17, the converse is not true.

4.6.1 The ICA Model and the MILCA algorithm

The classical, linear ICA model formulates n observed signals $x_{1,}x_2 \cdots x_n$ in terms of n statistically independent component signals $s_{1,}s_2 \cdots s_n$ as,

$$x_i = a_{i1}s_1 + a_{i2}s_2 + \cdots a_{in}s_n; \quad \text{i. e.}\, \mathbf{X} = \mathrm{A}\mathbf{S} \quad (4.18)$$

Where, $\mathbf{X} = [x_1, x_2 \cdots x_n]$ is a multidimensional variable with each element being an observed signal; $\mathbf{S} = [s_1, s_2 \cdots s_n]$ is another multidimensional variable whose elements are mutually statistically independent and **A** is an n x n matrix of real coefficients called the mixing matrix. ICA utilizes higher-order statistical methods to find the appropriate mixing matrix A, because with second-order methods (i.e. the ones involving covariance matrix) one can at the most obtain linear independence i.e. uncorrelatedness. Higher –order methods are the ones which use information on the distribution of x_i s' contained in their higher moments like skewness (3rd moment), kurtosis (4th moment) etc. Use of higher order statistics for the analysis implicates that ICA would be blind in distinguishing independent components (i.e. s_j s') if they have gaussian probability density. This is because variables with gaussian probability density combine to generate yet another gaussian variable and since all gaussian variables have same higher-order moments, the estimation function remains invariant under this summation.

Methods of independent component estimation can be coarsely described as a two-step process: a) formulation of an objective function, whose maximization or minimization enables the estimation of the independent components and b) devising a suitable algorithm to optimize the objective function. Statistical properties of the ICA method depends on the objective function while algorithmic properties like convergence speed, memory requirements etc. depends on the optimization algorithm. A large number of objective functions and optimization algorithms have been developed, almost all of which have been discussed in details in (Hyvarinen et al. 2001). Some of the most commonly used methods of implementing ICA are: FastICA (Hyvarinen 1999; Hyvärinen and Oja 2000), Infomax (Bell and Sejnowski 1995) and JADE.

However, For the ICA-model to be successfully implemented the following identifiability conditions need to be satisfied (Hyvarinen et al. 2001).

i. Analyzed multidimensional variable **X** must be realizable as a linear combination of signals from statistically independent sources.
ii. Signals from all the statistically independent sources, with possible exception of one, must be non-Gaussian.
iii. Number of observed linear mixtures must be at least as large as the expected number of mutually independent source signals.

For many systems, however, it is difficult to ascertain that all the above conditions are satisfied; as in the case of the transformation of neuromuscular activities into the wing kinematics in fruit flies. While none of the above conditions could be guaranteed, in this case the first condition was the most difficult to ascertain a priori. Given the physiology of the flight apparatus, even if the neuromuscular control units are activated mutually independently they may get nonlinearly coupled while acting via sclerites. Hence, I chose to work with a variant of the ICA model that does not rely on the conditions listed above.

Least-dependent component analysis (LCA) is one such method. In this model the idea is to search for the linear transformation of the input signals x_i s' such that the transformed signals z_i s' are mutually independent to the largest possible degree. I.e.

$$z_i = w_{i1}x_1 + w_{i2}x_2 + \cdots w_{in}x_n;\ \ \mathbf{Z} = \mathbf{WX} \tag{4.19}$$

These z_i s' are called the least dependent components (LDC). While it is always possible to find a linear transformation resulting in uncorrelated transformed signals (e.g., the Karhunen-Loeve transform in principal component analysis), the LCA model goes further and attempts to achieve full statistical independence. The coefficients of the optimal linear transformation define the separating matrix **W**. For each component z_i, the coefficients $[w_{i1}w_{i2}\cdots w_{in}]$ define the corresponding separating vector. In the special case when the input signals are a linear combination of fully statistically independent sources, LCA and ICA give identical results, i.e., the least dependent components are then equivalent to independent components.

Mutual information as cost function and the MILCA algorithm

In least-dependent component analysis a reliable estimator of mutual dependence of variables is crucial, because it is needed as a cost function for optimization. Mutual information is the most direct statistic that quantifies the dependence between two random variables. It is defined as the reduction in the uncertainty of one due to the knowledge of the other. It is a more complete measure of independence than the Pearson correlation coefficient because it quantifies the entire dependence structure, both its linear and non-linear parts. Two random variables are fully statistically independent if and only if their mutual information is zero. The mutual information of two random variables Q and R can be calculated as

$$\mathrm{I}(Q,R) = \mathrm{H}(Q) + \mathrm{H}(R) - \mathrm{H}(Q,R) \tag{4.20}$$

Where $\mathrm{H}(Q)$ and $\mathrm{H}(R)$ are the marginal entropies and $\mathrm{H}(Q,R)$ is the joint entropy[6]. For a multivariate signal one can extend this definition, to define the joint mutual information as:

$$\mathrm{I}(z_1, z_2 \cdots z_n) = \sum_{i=1}^{n} \mathrm{H}(z_i) - \mathrm{H}(z_1, z_2 \cdots z_n) \tag{4.21}$$

Reliable estimation of entropy from a finite number of samples of the random variables is a non-trivial task (Victor 2002). When calculating combinations of entropies (such as in Eq. 4.20, 4.21) that can have a total value close to zero, it is particularly important to eliminate any biases in entropy estimation. Kraskov et al. developed a reliable mutual information estimator (Kraskov et al. 2004) based on a previously known binless strategy for entropy estimation.

Mutual information estimator is the basis for the MILCA algorithm (mutual information based least dependent component analysis (Stögbauer et al. 2004)) which I used in my study. In searching for the least dependent components, the MILCA algorithm iteratively remixes the input signals, converging to linear combinations with minimal joint mutual information (Eq. 4.21). MILCA starts by transforming the set of input signals $\mathbf{X} = [x_1 x_2 \cdots x_n]$ to a set of mutually uncorrelated signals $\mathbf{Y} = [y_1 y_2 \cdots y_n]$:

$$\mathbf{Y} = \mathbf{W_0 X} \text{ such that } Cov(y_i, y_j) = \begin{cases} 0 & \text{if } i = j \\ 1 & \text{if } i \neq j \end{cases} \tag{4.22}$$

This transformation is achieved by suitable rescaling of the principal components of **X**, and is called whitening. $\mathbf{W_0}$ is the whitening matrix. Thus, the first step extracts linearly independent (i.e., uncorrelated) components of **X**.

The second step minimizes non-linear dependencies pairwise within the whitened multivariate signal **Y**. The whitened signals are remixed by rotating each pair (y_i, y_j) in its own plane and finding the angle $\varphi_{i,j}$ at which the mutual information (Eq. 4.20) of the rotated signals is minimized.

The result is

$$(y_1 \cdots y'_i \cdots y'_j \cdots y_n) = \mathbf{R}_{ij}(\varphi_{i,j})\,(y_1 \cdots y_i \cdots y_j \cdots y_n) \tag{4.23}$$

[6] The (differential) entropy of a variable Q with probability density $\mathrm{P}(Q)$ is defined as: $H(Q) = -\int_{-\infty}^{\infty} \mathrm{P}(Q) \log_b \mathrm{P}(Q) dQ$. The probability density has to be estimated from the available samples of the variable. To define the joint entropy $\mathrm{H}(Q,R)$ of two variables, the joint probability density $\mathrm{P}(Q,R)$ is used.

where $\mathbf{R}_{ij}(\varphi_{i,j})$ is a $n \times n$ rotation vector acting only in the 2×2 subspace (y_i, y_j). The product of such pairwise rotations for all pairs generates the $n \times n$ rotation matrix: $\mathbf{R} = \prod_{i,j} \mathbf{R}_{ij}(\varphi_{i,j})$.

The transformation $\mathbf{Z} = \mathbf{RY}$ defines a candidate set of components. The joint mutual information (Eq.4.21) of the components z_i s' is then evaluated, and pairwise remixing of the components is repeated until the joint mutual information converges to a minimum value.

The overall transformation from the set **X** of signals to the set **Z** of least-dependent components is given by

$$\mathbf{Z} = \tilde{\mathbf{R}}\mathbf{Y} = \tilde{\mathbf{R}}\mathbf{W_0}\mathbf{X} = \mathbf{WX}, \tag{4.24}$$

where $\tilde{\mathbf{R}}$ is the total rotation matrix after the iterative remixing, and $\mathbf{W} = \tilde{\mathbf{R}}\mathbf{W_0}$ is the separating matrix. I used the Matlab implementation of MILCA downloaded from

www.ucl.ac.uk/ion/departments/sobell/Research/RLemon/MILCA/MILCA.

Parameters were set as follows: distance to the 12th neighbor and rectangular 2D neighborhood for entropy estimation; first two Fourier components in the fitting of mutual information vs. rotation angle curve.

4.6.2 Least-dependent kinematic pattern of *Drosophila* wing motion

To extract the least-dependent component variations of wing stroke trajectory I used least-dependent component analysis (LCA). For the purpose of this analysis I first extract a new set of signals from the measured wing stroke data, as described in section 3.3.2. Briefly, a wing stroke defined from one dorsal reversal to the other was subdivided into 8 temporally equidistant phase points. Stroke positions at each of these phases in consecutive wing beat cycles defined a time series, 16 such time series (8 from each wing) were obtained from each flight test (figure 3.2). These set of 16 time series were then divided into segments of 2500 wingbeat cycles and each such segment defined a 16×2500 dimensional input signal **X** for LCA analysis. When choosing the segment length, the following two aspects were considered. Long-duration segments are more likely to contain multiple occurrences of distinct kinematic changes, which is a requirement for successful statistical analysis. On the other hand, for long segments the signal may violate conditions of wide-sense stationarity, a

pre-requisite of LCA analysis. Considering this tradeoff, I found the duration of 2500 wingbeat cycles to be approximately optimal and used this segment length throughout the analysis. Figure 3.2 shows an example of the 16 time series analyzed using LCA.

Using this input signal in equation 4.19 the least-dependent components z_i s' obtained are each a series of 2500 sample points, with one sample per stroke cycle. Figure 4.9 shows the least-dependent components obtained from MILCA analysis of the set of 16 signals shown in Fig.3.2. The value of z_i in a given cycle gives the weight of a particular stroke deformation mode in the overall wing stroke trajectory. For example, the ramp like increase in the value of the 9th least-dependent component between 0 to 500 wingbeat cycles in Fig.4.9A indicates an increased fraction of the stroke deformation mode represented by this LDC.

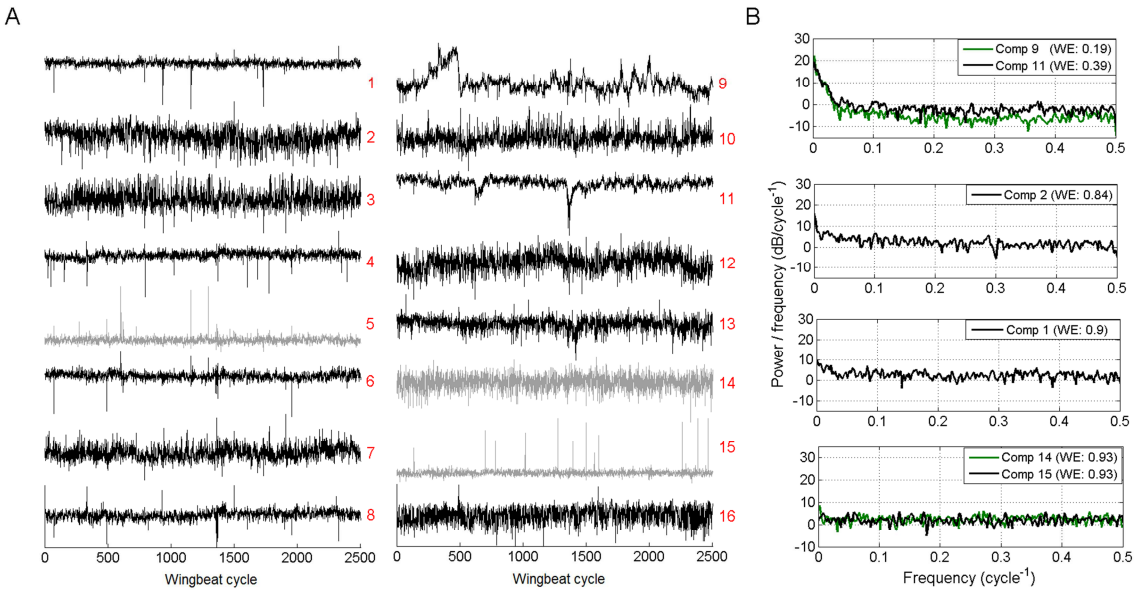

Figure 4.9: Least-dependent components and their temporal features. A) Least-dependent components estimated from the 16 signals shown in Fig.3.2B. Components with noise-like flat power spectra (Wiener entropy > 0.9) are plotted in gray. **B)** Welch power spectra and the Wiener entropy (WE) values of selected components shown in A.

The stroke deformation modes are defined by the coefficients of their corresponding separating vector (i.e. individual rows of the separating matrix **W**). For some components direct examination of the separating vector is sufficient to understand the corresponding stroke deformation mode. For example, components of type IV (see section 6.2.4) are obtained as the difference of the wing position signals x_1 and x_9 ; the corresponding stroke deformation mode therefore consists of an antisymmetric change of the wing position at dorsal stroke reversal for the two wings. In general, however, it is more convenient to

construct a graphical representation of the stroke deformation mode defined by the separating vector of a given component.

To do so, consider the inverse of Eq. 4.19,

$$\mathbf{X} = \mathbf{W^{-1}Z} \tag{4.25}$$

The mixing matrix $\mathbf{W^{-1}}$ defines the transformation from least-dependent components to original signals. When the full set of components $\mathbf{Z} = [z_1\ z_2 \cdots z_{16}]^{\mathrm{T}}$ is used in Eq. 4.25, the 16 signals $\mathbf{X}$ are faithfully reconstructed. Equation 4.25 can be expanded as

$$\mathbf{X} = \mathbf{W}^{-1}\langle\mathbf{Z}\rangle + \mathbf{W}^{-1}\left(\mathbf{Z} - \langle\mathbf{Z}\rangle\right) = \langle\mathbf{X}\rangle + \mathbf{W}^{-1}\hat{\mathbf{Z}}, \tag{4.26}$$

where $\langle . \rangle$ denotes the average over all wing strokes. The vector $\hat{\mathbf{Z}} = \mathbf{Z} - \langle\mathbf{Z}\rangle$ contains the deviations of the weights from their respective mean values. The wing stroke is thus represented as the sum of the baseline wing stroke $\langle\mathbf{X}\rangle$ (i.e., the mean stroke, averaged over the entire flight segment) and the wing stroke deformation $\mathbf{W^{-1}\hat{Z}}$**.** To construct the stroke deformation mode corresponding purely to the i-th component, the stroke deformations due to other components were suppressed– i.e., in the second term of Eq.4.26, I replaced all coefficients in $\mathbf{W}^{-1}$, except in its i$^{\text{th}}$ column, by zeros. From such partial reconstruction I obtained an array of phase points called the reconstructed stroke cycle, which when plotted together with the baseline wing stroke gives a visualization of the stroke deformation. In Fig. 4.10, I show an example of three reconstructed stroke cycles, with only one stroke deformation mode included. Comparing this to the baseline wing stroke shown in gray, it is seen that in this example, the stroke deformation mode is mainly an anti-symmetric change in ventral amplitudes (i.e., wing positions at ventral stroke reversal).

Each stroke deformation mode is thus a specific form of deviation from the baseline wing stroke. Deviation of any element of $\hat{z}_i$ from 0 implies that the stroke deformation mode represented by the i$^{\text{th}}$ LDC is active at that stroke cycle. Thus each LDC specifies the time course of activation of the stroke deformation mode it encodes. Together, the activation time course and the stroke deformation mode constitute a least-dependent kinematic pattern.

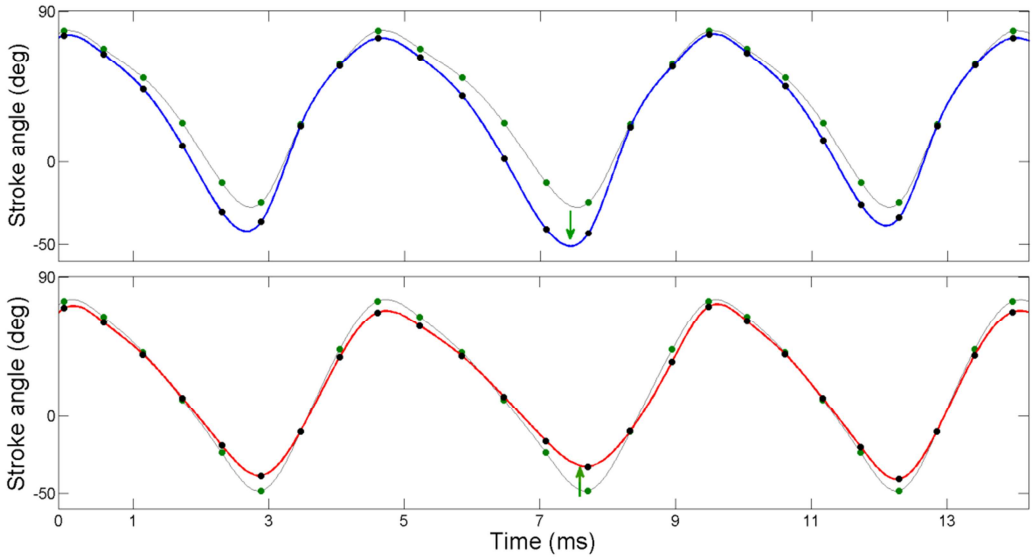

Figure 4.10: Reconstructed wing stroke, with deviation from baseline stroke due to a selected kinematic pattern. (Upper panel: left wing, lower panel: right wing). The green dots and the interpolated gray lines show the baseline stroke trajectory. The black dots (interpolated with blue and red line) are phase points reconstructed from only one selected component (see main text). The 8 reconstructed phase points for each wing are converted to time points, based on the recorded wing stroke duration. This stroke deformation mode is seen to consist of an increase in left ventral amplitude with simultaneous decrease in right ventral amplitude.

III. Results and discussion

CHAPTER 5

Intermittent bilateral coherence in physiological and essential tremor

5.1 Overview

This study was designed to explore the first topic of my thesis, i.e. the extent of bilateral coupling of the physiological and essential tremor. I evaluated the bilateral coherence of hand kinematics in the two most commonly occurring tremor types - physiological and essential tremor (Louis et al. 1998). I systematically assessed the time averaged bilateral coherence as well as its detailed temporal structure. I found frequently occurring bilateral coherence in the resting hand position as well as in two active postures for both PT and ET, contrary to some previous reports (e.g. Marsden et al. 1969a; Morrison and Newell 1999).

I first computed the coherence spectra of the 3D accelerometer signals that were recorded from healthy and from ET patients for a previously published study (Šprdlík et al. 2011). To confirm these findings, I repeated the analyses on a fresh set of hand motion data measured using a modified recording device from an additional group of healthy subjects (for details see section 3.3). Control experiments were also designed to exclude the role of direct mechanical coupling between the hands and to access the role of the common cardiac impulse to the two hands on their bilateral coherence. The results of this study are presented in 4 subsections of section 5.2. In section 5.3 I discuss these results.

5.2 Results

5.2.1 Tremor amplitude and spectral content

The power spectral density of the acceleration and the tremor displacement amplitude were evaluated for each recorded time series. In the healthy subjects group, typically a pronounced peak located within the range 6-12 Hz was found in the power spectrum for all the three hand positions. In addition, in the case of position 3 (Fig. 3.1) a considerable increase in low frequency vibrations (<5 Hz) was evident for all three acceleration components. The precise location of the main spectral peak varied among the subjects; hence the power spectrum averaged over all 30 healthy subjects (Fig. 4.2 A) shows a broad and relatively flat peak. In contrast, for ET subject the power spectrum typically showed a sharp peak located at 4 to 6 Hz, and in addition one or more peaks corresponding to higher harmonics. Consequently, the power spectrum averaged over all 34 ET patients showed a pronounced multiple peak structure, for all three studied hand positions (Fig. 4.2 D-F).

Table 5.1: Average amplitudes and the 90% range of hand displacements in PT and ET, evaluated separately for each hand position and each spatial axis.

Component of hand displacement	**Position 1**	**Position 2**	**Position 3**
	Healthy subjects: mean amplitude (90% range) in mm		
X	0.052 (0.022–0.116)	0.069 (0.044-0.118)	0.198 (0.121-0.326)
Y	0.058 (0.026–0.111)	0.101 (0.057-0.157)	0.342 (0.221-0.488)
Z	0.038 (0.021-0.065)	0.074 (0.045-0.130)	0.437 (0.305-0.600)
	ET patients: mean amplitude (90% range) in mm		
X	0.270 (0.025-1.035)	0.406 (0.047-1.958)	0.550 (0.126-1.936)
Y	0.238 (0.026-0.950)	0.545 (0.065-2.262)	0.757 (0.221-2.730)
Z	0.307 (0.021-1.267)	0.567 (0.046-3.065)	0.745 (0.305-2.199)

Table 5.1 gives the mean tremor amplitudes (computed as described in Sec. 4.2.3), as well as the range of amplitudes that covers 90% of the subjects. It is seen that in a given hand position, the amplitude of motion is usually comparable for all three spatial axes. The average tremor amplitude in ET patients was found to be 4- to 8-fold higher than in healthy subjects for the resting position as well as for the first posture (Table 5.1, first two data columns). In the second posture, the amplitude was approximately 2-fold higher for ET patients (Table 5.1, third data column).

5.2.2 Bilateral coherence of wrist kinematics

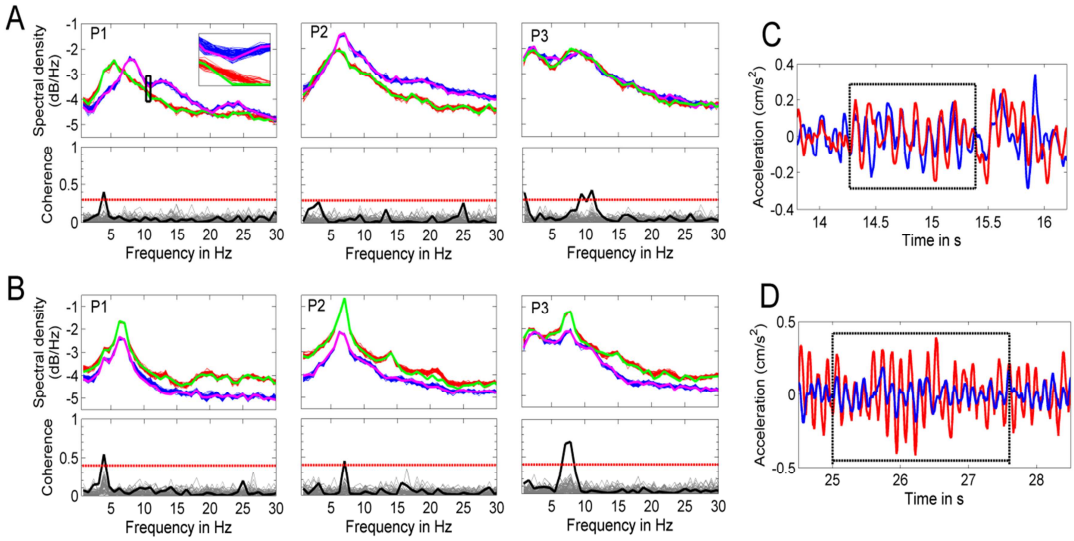

Figure 5.1: Examples of significant bilateral coherence of hand motion in physiological and essential tremor. A) Upper subpanels: Power spectra for the z-component of acceleration of the left (magenta) and right (green) hand in a healthy subject and their respective 100 surrogate time series (left: blue; right: red). Magnified snippet (rectangle) shown in the inset for better visualization (upper subpanel, column 1). Columns correspond to the measurements from the three hand positions. Lower subpanels: Coherence function between the left and right hand acceleration (black) and their surrogates (gray). Red line shows the coherence threshold for rejecting the null hypothesis of no coherence (for details refer to the text). **B)** Similar plots as in A, but for an ET patient. **C)** An interval of the left (blue) and right (red) acceleration demonstrating an event of synchronization (rectangle) contributing to the coherence peak in the left subpanel of A. **D)** An interval of the left (blue) and right (red) acceleration demonstrating an event of synchronization (rectangle) contributing to the coherence peak in the right subpanel of B.

The simultaneous accelerometric recording from both hands allowed us to evaluate the bilateral coherence of wrist motion. For each subject and each measured hand position, I computed the spectral coherence between the acceleration signals from the left and

right hand, separately for each spatial axis (see section 4.3.2). I then determined if the coherence magnitude exceeded the threshold value 0.3 in case of healthy subjects and 0.4 in case of ET patients. In the examples below, the plot shows, for each coherence spectrum of the recorded accelerations, also the coherence spectra of 100 pairs of the corresponding surrogate time series. The surrogates are constructed to have a power spectrum matching the recorded time series, but to be mutually statistically independent. As seen in the example figures, the peaks in the coherence spectra of the surrogates do not exceed the chosen thresholds of statistical significance, thus confirming that the thresholds are adequate.

Fig.5.1A (lower subpanels) shows an example of the coherence spectra for motion along the Z axis (perpendicular to the palm of the hand) in a healthy subject. In this case, statistically significant coherence peaks are obtained in the resting hand position (Fig.5.1A, left column) as well as in the postural position 3 (Fig.5.1A, right column). Fig.5.1B shows an analogous example from a subject diagnosed with ET. As seen from comparison to the power spectral densities (shown in upper subpanels), high coherence peaks are obtained at frequency matching the main tremor frequency in position 2 and 3, while coherence in position 1 occurs at a lower frequency. Figure 5.1C,D shows the time course (within a selected interval) of the left and right hand acceleration in position 1 for the healthy subject and in position 3 for the ET patient. In both these examples, the bilateral coherence can be readily discerned by eye in the acceleration time series (black rectangle).

To summarize such evaluations across all subjects in a given group, we extracted the amplitude (i.e., the coherence value) and the position (i.e., the frequency) of each statistically significant peak in the coherence spectrum. For each position and spatial axis, the coherence peaks from all subjects are then plotted as points in one summary graph - Fig.5.2A-C summarizes the coherence peaks obtained in the group of 30 healthy subjects, while Fig.5.2D-F was obtained from the group of 34 subjects with diagnosed ET. The rows correspond to the 3 studied positions and the columns correspond to the 3 spatial axes. The number of subjects with at least one peak of height above the respective coherence thresholds (i.e. 0.3 for healthy subjects and 0.4 for ET patients) is listed in the legend of each panel.

In the resting position, significant bilateral coherence was obtained in nearly all subjects from both groups. As seen in Fig.5.2A, D, coherence was most commonly found for motion in the X direction (i.e., the proximal-distal axis of the hand), but 50-60% of

subjects also showed coherence of motion in the Y (transversal) and Z (dorsal-ventral) directions. 90%, resp. 92% of subjects in each group showed significant coherence in the resting position for at least one axis of motion (Table 5.2). Both for healthy subjects and for ET patients, the coherence peaks are predominantly located within the frequency range 1 Hz to 10 Hz.

Compared to the resting tremor, a much lower prevalence of bilateral coherence was found in position 2 (hands extended) for healthy subjects. As seen in Fig.5.2B, only 4 (i.e.,13%), resp. 7 (i.e., 23%) among 30 healthy subjects showed significant coherence of motion in the Z, and Y direction respectively. For motion along the X axis, however, the majority (19, i.e. 61%) of subjects showed significant coherence peaks. For position 3 (arms extended) (Fig.5.2C), about half of the healthy subjects showed significant coherence of motion along each of the three spatial axes. The coherence peaks were located in the broad range 1 Hz – 12 Hz. and their peak coherence value rarely exceeded 0.5.

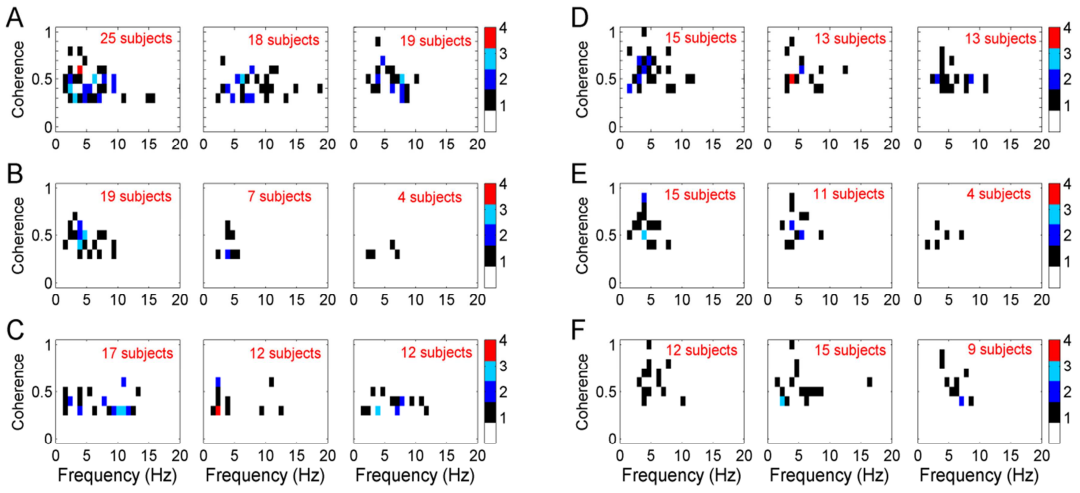

Figure 5.2: Summary of significant peaks in the bilateral coherence spectrum. For each frequency and coherence magnitude bin, the number of peaks obtained in the corresponding subject group is given (see color scale shown at right). **A-C)** show peaks from 30 healthy subjects, with hands in position 1 (panel A), 2 (panel B) and 3 (panel C). The left, middle, and right subpanels correspond to x, y, and z components of acceleration. **D-F)** show peaks from 34 ET patients.

High coherence values were reached more often in ET patients. Thus in the 3rd hand position, 25% of ET patients showed a coherence value exceeding 0.7, while none of the healthy subjects reached such high coherence[1] (Fig.5.2 C,F). In both postures, and for all three motion axes, the peaks of particularly high coherence (above 0.7) were restricted to the frequency range 3 to 5 Hz, which coincides (see Fig.4.2 D-F) with the main

frequency band of the ET. In such cases the coherent component carries a major part of the total tremor power, and consequently the bilateral coherence is readily apparent upon examination of the acceleration recordings (example in Fig.5.1D). We verified using surrogate data (see section 4.3) that all coherence peaks exceeding the threshold 0.4 are statistically significant, even when they occur at the frequency matching the main tremor frequency.

For both healthy subjects and ET patients, I quantified how strongly the bilaterally coherent content contributes to the total motion of the hands, as follows. For a given coherence peak, we first evaluated the power of the coherent part of motion by integrating the spectral cross-power within the half-width of the peak. We then computed its ratio to the power of total motion (evaluated as the geometric mean of the spectral powers, integrated within the range 2 Hz to 15 Hz, of the two motion series). For the coherence peaks that have overlap with the principal peak in the power spectral density, we typically found ratios between 51% and 87% (e.g., 51% for the example in the right panel of Fig.5.1B), showing that the coherent component makes a major contribution. For the coherence peaks at lower frequencies, we found values in the range 4-24% (e.g., 24% for the example shown in figure 5.1A), indicating a minor but still significant contribution to the total hand motion.

Hand position	**Healthy subjects (Total: 30)**	**Essential tremor patients (Total: 35)**
	Number of subjects with bilateral coherence >0.3	**Number of subjects with bilateral coherence >0.4**
	Z-component	
1	19	13
2	4	4
3	12	9
	At least one spatial component	
1	29	19
2	22	17
3	24	20

Table 5.2. Numbers of subjects with significant bilateral coherence of the indicated components of hand acceleration.

To assess if bilateral coherence was primarily associated with lower or higher amplitudes of tremor, we examined the relation between the coherence peak magnitudes (Fig.5.2; only the highest peak from each subject was retained) and the tremor displacement amplitudes (obtained as in section 4.2.3), A positive correlation was identified for ET patients in the resting hand position: the Pearson correlation

coefficient was 0.53 (with t-test based p-value of 0.03) for motion in x-direction, and 0.69 (p-value 0.009) for motion in y-direction. No statistically significant relation between coherence magnitude and tremor amplitude was found for other position / motion axis combinations in either ET patients or healthy subjects.

5.2.3 Intermittent character of bilateral coherence

To examine the temporal distribution of bilateral coherence within the recorded 20 sec intervals, we used wavelet-based computational methods, which allow a systematic non-stationary analysis. The wavelet coherence function (see section 4.5.2) was evaluated for recordings that showed significant peaks in the coherence spectrum.

For both healthy subjects and ET patients, I found that the bilateral coherence is distributed highly non-uniformly in time. Typically, patches of high coherence lasting for several seconds are separated by time intervals with low coherence. Examples from a healthy subject and an ET patient are shown in Fig.5.3. In the wavelet coherence plots (panels A, C), the coherence value is color-coded, while the y-axis corresponds to the wavelet scale converted to frequency. The black contours mark the regions in which the coherence values exceed the 95% confidence level for rejecting null coherence. The arrows indicate the relative phase of the two signals at particular time points: right arrow means 0˚ phase shift, left arrow 180˚, and downwards arrow a 90˚ phase lead of the left hand w.r.t the right. In the PT example (Fig.5.3A), isolated patches of significant coherence at frequencies 4-6 Hz appear at time 4 to 6 sec and 8 to 10 sec. These short intervals of very high coherence generate the significant peak near 5 Hz in the coherence spectrum (Fig.5.3B). In the ET example (Fig.5.3C), the patches of high coherence at 3-5 Hz are frequent, while only short intervals of very low coherence occur (7-8 sec). Correspondingly, the peak near 4 Hz in the coherence spectrum (Fig.5.3D) has very high amplitude (0.9).

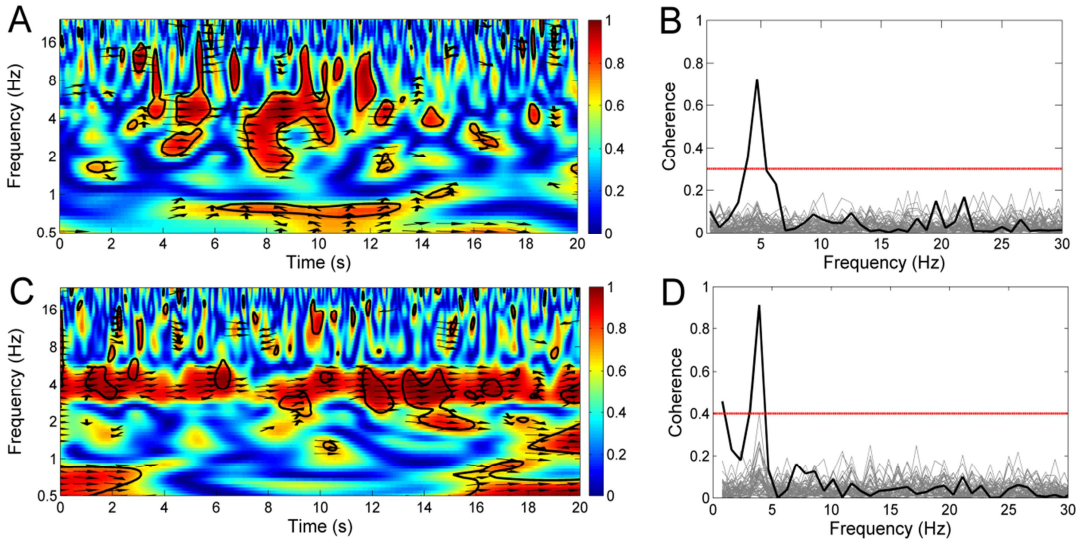

Figure 5.3: Transiently occurring bilateral coherence of hand acceleration. A-B: Rest tremor in a healthy subject in hand position 1 (z-component). **A)** Wavelet coherence of the left and right hand acceleration components. Coherence (color axis) and the corresponding frequencies are plotted in log scale of base 2. Regions enclosed in black contours mark the peaks for which the null hypothesis of no coherence can be rejected with confidence level of 0.95 and the black arrows show the instantaneous relative phase between the particular frequency components (right arrow: in phase, left arrow: anti-phase, down arrow: left hand leading right hand by 90°). **B)** Coherence spectra of the left and the right hand acceleration components (black line) and the corresponding 100 surrogate time series (gray lines). Red line shows the coherence threshold for rejecting the null hypothesis. **C-D:** As in A-B, but from ET subject in hand position 2 (z-component).

Based on the wavelet coherence plots, I identified numerous intervals of transient coherence typically lasting several seconds, for both PT and ET subjects, in all three studied positions. Examples of these events of significant coherence are given in Fig.5.4; the lower subpanels show the acceleration time courses from both hands, and the upper subpanels plot the wavelet coherence within the relevant frequency band. While the left and right hand oscillations are in-phase in most cases, anti-phase coherence (Fig.5.4G) and an approximately 90° phase shift (Fig.5.4E) are seen in examples shown from ET patients in non-resting hand positions. It is also seen that while in some examples (panels A, D), high coherence coincided with intervals of increased tremor amplitude, this was not the case in general (panels C, F).

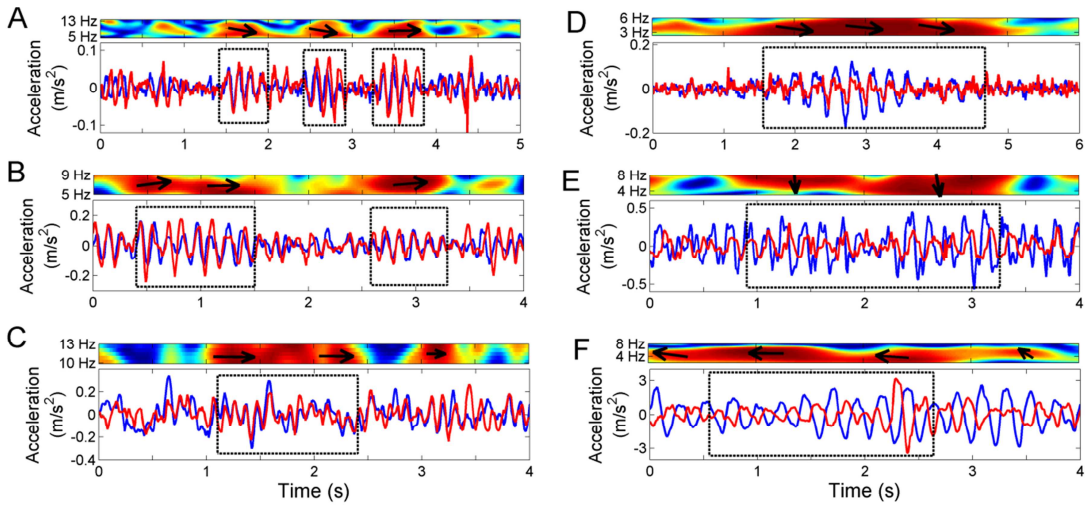

Figure 5.4: Examples of intermittent synchronization of hand acceleration and the corresponding wavelet coherence plots. A-C) Lower subpanels: Time course of left (blue) and right (red) hand acceleration (z-component) of healthy subjects with hands in position 1 (panel A), position 2 (panel B) and position 3 (panel C). **Upper subpanels:** Wavelet coherence spectra for a selected range of pseudo-frequencies at the time interval shown in the corresponding lower panels. The color scale is the same as in Fig.5.3A and C. **D-F)** Similar plots as in A-C with examples from ET patients.

Table 5.3: Prevalence of coherence events (in recorded data) that are longer than the 95th percentile duration of events in surrogate data.

Group of subjects	% of the number of coherence events			% of total event duration		
	P1	P2	P3	P1	P2	P3
PT	28	19	13	67	47	39
ET	30	37	24	77	71	70

I systematically extracted the transient bilateral coherence events in all subjects, as described in section 4.5.2. In Table 5.3, I report the prevalence of coherence events of significant length. As short intervals of statistically significant coherence can arise even in non-coherent signals, I first determined the 95th percentile of the duration of such "false events", by analyzing surrogate signal pairs (Sec. 4.5.2). This 95th percentile duration was found to range between 2.2 and 3.1 sec (depending on hand position and subject group). The coherence events that are found in the original recorded signals and that exceed this duration ("long events") have a smaller than 5% probability to arise as false positives. These "long events" were prominent in both PT and ET recordings: they make up to 37% of all detected coherence events, as opposed to the 5% expected by chance. When expressed in terms of total duration, these long events account for up to 77% of the total duration of all detected events (Table 5.3). Remarkably, these

percentages do not differ between PT and ET for the resting hand position, but are much larger (1.8×) in ET than in PT for the positions P2 and P3. Thus for postural tremor, long episodes of intermittent coherence are more dominant in ET than in PT.

5.2.4 Dependence of bilateral coherence on the ballistocardiac forcing in healthy subjects

To evaluate the possibility that the observed bilateral coherence originates from ballistocardiac forcing, I analyzed joint accelerometric recordings of hand motion and of chest wall motion, measured in 12 healthy subjects (Ref. section 3.2.2). While some instances of bilateral coherence (see example in Fig.5.5A, peak near 7 Hz) were associated with significant chest vs. left hand and chest vs. right hand coherence, other bilateral coherence peaks (Fig.5.5A, near 4 Hz) were not. To analyze this coupling systematically we computed the partial coherence (section 4.3.3) between the hand signals, conditioned on the chest signal. Bilateral coherence that is not accompanied by significant partial coherence (Fig.5.5A at 7 Hz) may be fully attributed to the dependence of the hand signals with the chest signal. Conversely, the bilaterally coherent part of hand motion has no linear relation to the chest signal when partial coherence matches the bilateral coherence (Fig.5.5A at 3 Hz).

I evaluated the partial coherence for all cases of significant bilateral coherence found in the group of 12 healthy subjects. The results are summarized in Fig.5.5B. The histogram shows, for each frequency bin, the number of occurrences of significant bilateral coherence and of significant partial coherence, combined from all three hand positions and all three spatial components. It is seen that at frequencies above 8 Hz, significant bilateral coherence is typically not accompanied by significant partial coherence (the ratio of the number of occurrences of partial vs. bilateral coherence is 6/47 = 12%). In contrast, at the frequency range 1-8 Hz, partial coherence frequently persists (51%). A similar conclusion is reached when the resting hand position is excluded from the dataset (the ratio becomes 13% above 8 Hz and 69% at 1-8 Hz). This indicates that in the lower frequency range, bilateral coherence is typically independent of ballistocardiac forcing. At frequencies above 8 Hz, including the range 8-12 Hz corresponding to the main frequency band of PT, bilaterally coherent hand motion is usually coupled to cardiac activity.

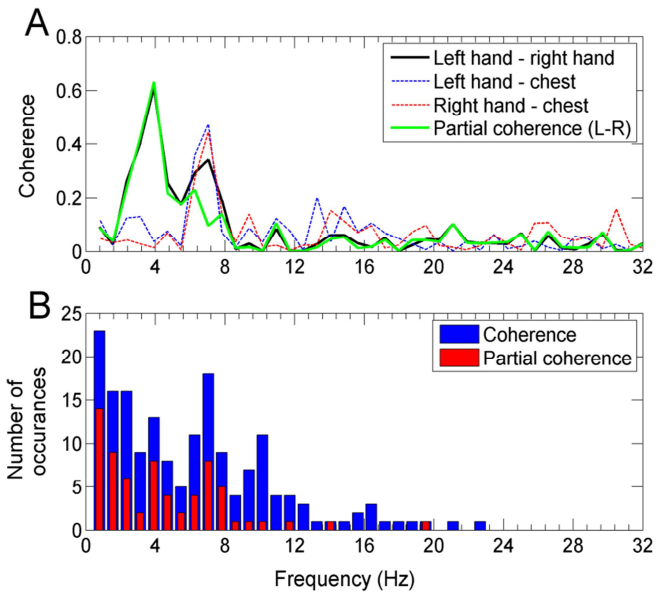

Figure 5.5: Bilateral coherence conditioned on the chest acceleration signal. A) Partial coherence spectrum (green line) between the y-components of the left and the right hand accelerations in position 2 while the contribution from the chest motion is subtracted. Other plots (black solid line, blue and red dashed lines) show the pairwise coherence spectra of the acceleration components of the hands and the chest. **B)** Summary histogram of all the occurrences of higher than 0.3 coherence and partial coherence values (pooled in from all three acceleration components measured in all the three positions) in the group of 12 healthy subjects.

5.3 Discussion

In summary, I found frequently occurring bilateral coherence of hand tremor kinematics in both healthy subjects and ET patients. While the prevalence of bilateral coherence depended on the studied hand position and on the measured spatial component of acceleration, at least 48% of subjects showed significant coherence along at least one spatial direction in all three studied hand positions (section 5.2.2). The healthy subjects and ET patients differed mainly in the magnitude of coherence (with nearly complete bilateral coherence detected in several ET patients) and in the oscillation frequencies at which the coherent motion was observed in the non-resting postures (a narrow range of 4-6 Hz for ET patients vs. the broad frequency range 1-12 Hz in healthy subjects). In both subject groups, the bilateral coherence of hand kinematics was found to be highly intermittent. Epochs of several seconds during which the motion of the hands is highly coherent are separated by intervals with insignificant coherence (section 5.2.3). Partial coherence analysis (section 5.2.4) indicated that in healthy subjects, the bilateral kinematic coherence observed at 8-12 Hz arises from a coupling to the ballistocardiac rhythm. In the following subsections, we compare our findings with those of previous literature, and discuss implications for the possible mechanisms of bilateral coherence in physiological and essential tremor.

5.3.1 Bilaterally coherent tremor is not limited to the resting hand position

We found that in healthy subjects, kinematic bilateral coherence was highly prevalent for tremor in the resting hand position. 97% of healthy subjects showed significant coherence for at least one of three spatial axes, with coherence peaks located in the range 2-12 Hz (Table 5.2 and Fig.5.2A). This finding is consistent with previous literature. In (Marsden et al. 1969c), finger tremor was recorded and its bilateral coherence evaluated for 4 healthy subjects, in a position with relaxed effector muscles. The peak coherence values reported in (Marsden et al. 1969c) ranged from 0.4 to 0.9 and occurred at frequencies 3 to 12 Hz.

Although resting tremor is considered not characteristic of ET, it is known to occur in some cases (Cohen et al. 2003). In our group of 34 ET patients, 21 had a clear spectral peak at 5±1 Hz in the resting hand position, indicating the presence of resting tremor. Correspondingly, the tremor amplitude range (Table 5.1) in the ET patients group extended to 10-fold higher amplitudes than in the healthy subjects group. Highly prevalent bilateral coherence in the resting hand position was found in the ET patients group (Fig.5.2D, Table 5.2). A similar prevalence and distribution of coherence was obtained when evaluated separately for the subgroup of 21 patients with clinical and sub-clinical resting ET tremor (not shown). In addition, for ET patients a positive correlation was found between the coherence magnitude and the tremor displacement amplitude (end of section 5.2.2). This suggests that the ET resting tremor has a fundamentally bilateral origin. We are not aware of any previous assessment of bilateral kinematic coherence for ET in resting position.

Unlike some previous reports, we found that kinematic bilateral coherence was frequent in postural tremor. In both studied postures, at least 73% of healthy subjects and 48% of ET patients showed significant coherence for at least one acceleration component (Table 5.2). Among previous studies, (Marsden et al. 1969a; Morrison and Newell 1999) did not find significant coherence in non-resting upper limb tremor; however, their recordings were restricted to one spatial component of acceleration, and only a standing posture was studied in (Morrison and Newell 1999). The study of (McAuley and Rothwell 2004) reported occasional bilateral coherence of the hand accelerations in ET patients, but in the absence of bilateral EMG coherence considered this finding to be an artifact.

To minimize the possibility that the finding of frequent bilateral coherence was a statistical artifact, I used stringent statistical significance criteria, described in detail in section 4.3.2. While choosing the coherence threshold for rejecting the null hypothesis of no coherence, two aspects were taken into consideration, i. the minimum coherence value that would sufficiently confirm (Wang et al. 2004) the existence of a linear dependence, and ii. the bias error due to the overlapping spectral peaks of the two signals. To take into account the latter I used the method of surrogate data, obtaining the zero-coherence estimates from pairs of mutually independent time series that preserved the spectral content of the measured hand acceleration time series. The coherence thresholds so obtained (0.3 for healthy subjects and 0.4 for essential tremor patients)

are stricter than the threshold (Eq. 2 and Halliday et al. 1995) most commonly used in the previous tremor literature.

In addition to using a conservative criterion for declaring statistically significant coherence, I carried out control experiments to make sure that the bilateral coherence was not an experimental artifact. I repeated the measurements on a smaller group of healthy subjects using a similar, but newer recording device (section 3.2.2, results in section 5.2.4). The findings on bilateral coherence were consistent in the two groups of healthy subjects.

Thus my results indicate that both PT and ET are frequently bilaterally coherent. One reason why some previous studies under-reported this kinematic coherence may lie in its intermittent time structure. The wavelet-based analysis (section 5.2.3) showed that typically, short epochs (several sec) of high coherence are interspersed with intervals of insignificant or low coherence. The coherence magnitude obtained from stationary analysis (as performed in previous studies) reflects the total length of the high coherence vs. low coherence intervals. Limited duration recordings (e.g., 20 sec) may sometime miss the sparse high-coherence intervals, resulting in no detected coherence. A second possible reason is the highly uneven prevalence of bilateral coherence along the different directions of hand motion (discussed in detail in the next subsection). In (Marsden et al. 1969a, 1969c), bilateral coherence was evaluated for motion in the dorsal-volar direction in a posture equivalent to our position 2. In the 18 subjects studied in (Marsden et al. 1969a), only insignificant coherence (0.008 to 0.108) was found. This finding can be viewed as consistent with the results presented in this thesis for motion in the dorso-palmar (i.e., z) direction in position 2 (Fig.5.2B). The motion in proximo-distal (x) and frontal (y) directions, for which I found significant coherence in position 2, was not recorded in (Marsden et al. 1969a). Similarly, the report of no statistically significant coherence between the hand tremors of healthy subjects in (Morrison and Newell 1999) was based on the analysis of only a single component of the hand acceleration.

5.3.2 Strong dependence of bilateral coherence on the axis of motion

Tremor kinematics is most commonly assessed by measuring the hand acceleration along the dorso-palmar axis (e.g.,(Morrison and Newell 1999)). Our triaxial

accelerometer recordings showed, however, that the tremor displacement amplitude was comparable along the three measured axes (Table 5.1). I therefore analyzed and compared the bilateral coherence of motion for all three directions, i.e., the proximo-distal, the frontal (left-right), and the dorso-palmar axis.

In PT, I found that bilateral coherence occurred most frequently between the proximo-distal components of acceleration. For all three studied hand positions (Fig.5.2 A-C), the number of subjects with significant bilateral coherence in this direction was at least 30% higher than in the other two directions. For position 2 (hands extended) and position 3 (arms and hands extended), this pattern matches a bilaterally coherent rigid motion of the hands/arms along the sagittal body axis. For position 1 (relaxed hands), the dominant coherence along the accelerometer x-axis would naturally arise from a coherent rotation of the two hands about the frontal axis of the wrist (see Fig.3.1A). Such rotation generates a centripetal acceleration pointing along the radial direction of the circular motion, i.e., along the proximo-distal axis of the relaxed hand. Both of these types of motion (i.e., bilaterally coherent rigid motion in hand positions 2, 3 and rotational motion in hand position 1) might be generated by a mechanical force acting along the sagittal body axis. A torso swing was unlikely in our experiments as the subjects were instructed to lean their back against the chair backrest. An alternative mechanical source consists of the forces generated in the arms by the blood flow (see next section).

In ET, a weaker predominance of bilateral coherence in proximo-distal direction was seen for hand positions 1 and 2 (Fig.5.2 D, E); while in position 3 the coherence was comparable along all three directions (Fig.5.2F). Unlike the case of PT, we therefore found no evidence that the source of bilateral synchronization in ET acts predominantly in the proximo-distal direction.

5.3.3 Ballistocardiac forcing contributes to the bilateral coherence of physiological tremor

The effect of ballistocardiac forcing (details in section 1.3.2) is expected to be synchronous in both hands, and could therefore contribute to the observed bilateral coherence of tremor kinematics. In my study I explicitly evaluated the extent of this contribution for healthy subjects, by computing the partial coherence (section 4.3.3) between the left and right hand kinematics, conditioned on the motion of the chest wall (measured using a third accelerometer). Results show (Fig.5.5B) that when bilateral

coherence occurred in the frequency range 8 to 12 Hz, it was usually not accompanied by significant partial coherence – i.e., the chest wall motion and the bilaterally coherent component of hand motion had a correlated time course. This suggests that the ballistocardiac forcing is responsible for the observed bilateral coherence. This conclusion agrees with the interpretation made by (Marsden et al. 1969c) for bilateral coherence in resting hand position. For bilateral coherence found at lower frequencies (1 to 8 Hz), however, we found that it was often accompanied by significant partial coherence, indicating an origin independent of ballistocardiac forcing.

While the data supports a relation between the bilateral coherence in the main frequency band of postural PT and the ballistocardiac forcing, it is unlikely that the coherent motion of the hands arises directly and solely by the mechanical action of this force. Two lines of evidence speak against such direct mechanism: 1) The magnitude of the ballistocardiac impulses does not vary in an intermittent way, in contrast to the observed intermittent character of bilateral coherence. 2) The recorded magnitudes of bilateral coherence at 8-12 Hz (Fig.5.2A-C) are comparable in all three hand positions, despites large differences in tremor amplitudes. Also, when the coherence peaks found in a specific hand posture are examined, no significant correlation between the coherence magnitude and the tremor amplitude is found for PT (end of section 5.2.2). This implies (see Eq.4.6) that the power of the coherent component scales with the total tremor power. Such scaling, however, is not expected if the coherent component always arises from the same external force (i.e., ballistocardiac forcing) that is independent of the bilaterally incoherent muscle activity (i.e., the dominant source of postural tremor of varying amplitude).

5.3.4 Possible mechanisms of the observed bilateral coherence

In this section I discuss, on the basis of my kinematic analysis and the previous literature, the likely mechanisms of the observed bilateral coherence.

For PT, I argued above that the bilaterally coherent motion near the main tremor frequency is related to ballistocardiac forcing, but is not directly generated by it. Rather, we propose that the tremors in both upper limbs are simultaneously entrained (Elble et al. 1992; Cathers et al. 2005) by the afferent signal modulation arising from ballistocardiac impulses. In this scenario, the ballistocardiac impulses act as a weak

rhythmic input that influences the nonlinear tremor oscillation. It is a hallmark of noisy nonlinear oscillators that a weak rhythmic input may entrain the oscillator to the external rhythm, but such entrainment is interrupted by intervals during which the synchrony is lost (Pikovsky et al. 2003). In (Elble 1992), tremor entrainment to rhythmic torque stimuli was found to occur intermittently, in epochs lasting 6 to 20 sec. In the mechanism I propose, the left and right tremor oscillators become mutually coherent during the epochs when both are entrained to the common input rhythm. The pattern of overlap of the left and right entrained intervals generates the highly intermittent character of bilateral coherence. The proposed mechanism is also capable of explaining the large amplitudes of bilaterally coherent motion: due to the nonlinear interaction, a weak input is capable of entraining a nonlinear oscillation of large amplitude (Pikovsky et al. 2003). In (Cathers et al. 2005), 0.3° wrist rotations (the lowest stimulus amplitude investigated) were sufficient to fully entrain PT when the stimulus frequency was within 2 Hz of the intrinsic tremor frequency. While ballistocardiac forcing has a much lower principal frequency (~1 Hz), it can generate hand movement perturbations at the mechanical resonance frequency of about 10 Hz (McAuley and Marsden 2000), which may in turn act as an efficient entraining stimulus.

As ET patients were not included in the evaluation of partial coherence conditioned on the chest signal (section 5.2.4), one cannot exclude that ballistocardiac forcing played a role in the observed ET bilateral coherence. However, in this case it would be even more unlikely, compared to the case of postural PT, that the ballistocardiac forces directly generated the coherent motion of the hand. For each of the studied hand positions, the ET tremor amplitudes were several times higher than in PT (Table 5.1), and achieving comparable coherence in ET and PT would therefore require the ballistocardiac forces to be significantly larger in ET patients than in healthy subjects. In fact, even higher magnitudes of bilateral coherence were reached in the ET group, with some cases of nearly full coherence (magnitude 0.9) at the main tremor frequency 3-5 Hz (Fig.5.2D-E). This, together with the finding of significant positive correlation between the coherence magnitude and the tremor amplitude in the resting position (see end of section 5.2.2), indicates that the bilateral coherence in ET does not arise from an external additive influence. Similarly to that proposed for PT, ballistocardiac forcing might nonlinearly entrain the ET in both hands, and thus generate the observed bilateral coherence (which was intermittent but usually more sustained in ET – see section 5.2.3). Achieving the more sustained coherence would, however, require that the ET muscle activity is more prone to entrainment than PT muscle activity. ET entrainment by rhythmic wrist forcing

has been demonstrated in the literature (Elble 1992), however the efficiency of entrainment appeared weaker than in the case of PT (Cathers et al. 2005).

It is therefore more likely that the intermittent bilateral coherence observed in ET arose due to a mutual neural coupling between the left and right tremor oscillators. Such mutual coupling may occur at the level of the brain generators (e.g., as shown by (Muthuraman et al. 2013) for the orthostatic tremor), or at the level of motor control pathway (e.g., as in the synchronization of psychogenic tremors via the pathways that underlie bimanual interference during voluntary movements (Klapp 1979; Hallett 2010)). In ET, a weak interaction between the central tremor generators in the right and left brain has been proposed. (Hellwig et al. 2003) found significant contra- as well as ipsi-lateral corticomuscular coherence during postural hand tremor. While the former was present consistently, the latter appeared in only some of the evaluated 60 sec intervals, indicating a dynamic cross-hemispherical interaction between the central oscillators of ET. These epochs of bilateral corticomuscular coherence were associated with bilateral coherence of muscle activity; kinematic bilateral coherence was not evaluated in (Hellwig et al. 2003). In PT, indications of interaction between the left and right tremor have been recently shown (Morrison and Newell 1996) (Boonstra et al. 2008; Kavanagh et al. 2013); the underlying coupling may potentially generate the cases of bilateral coherence at 1-8 Hz that we found to be unrelated to ballistocardiac forcing (Sec. 5.2.4).

CHAPTER 6

Modular control of wing kinematics of the fruit fly *Drosophila melanogaster*

6.1 Overview

This study was conceived to address the second topic of my study, i.e. the modular control of complex wing stroke variations in fruit flies. For this purpose I analyzed wing motion sampled at a rate of 6250 Hz for long flight durations (up to 12 000 wingbeat cycles) of tethered flying fruit flies (Ref. section 3.3). With such extensive recordings I could apply, for the first time, an advanced statistical analysis designed to identify the full repertoire of independently controlled kinematic patterns (Ref. section 4.6). Results of this part of the study (Chakraborty et al. 2015) are presented in section 6.2.

In the second part of this study I focused on a specific kinematic pattern with recurring single cycle stroke variations. Although this kinematic pattern is not expected to have any crucial functional role, but it has the potential to provide a unique window into the fast time scale neuromotor control of wing kinematics. Among all the sensorimotor control systems of the fly, only the haltere mechanosensors have a sensorimotor delay that is shorter than the wing stroke period and most likely contribute to a stroke-by-stroke wingbeat control. Hence, I studied the effect of haltere ablation on the characteristic properties of these special kinematic patterns. Results of this second part of the study are presented in section 6.3. In section 6.4, I present the discussion related to both the parts of this study.

6.2 Results I: Independently controlled wing stroke patterns

In the first three subsections, I mention the important general features of the wing motion decomposition into least-dependent kinematic patterns, illustrated with specific examples. The fourth subsection provides a classification of the kinematic patterns obtained frequently across 100 test flights from 10 flies, and discusses the correspondence of some of these patterns to known flight maneuvers.

6.2.1 Events with distinct time courses are separated into distinct least-dependent components

A least-dependent component is a specific linear combination of the input signals[7], obtained from LCA analysis (Ref. section 4.6.2). It defines the time course of activation of a particular "stroke deformation mode". The 16 signals (as described in the last part of section 3.2.2) contain events with a variety of durations and forms. As an example, Fig.6.1A shows the 16 signals over 1500 wingbeat cycles from a typical recording. Each event typically appears in multiple input signals. For example, events occurring symmetrically in left and right wings dominate the signals 1, 9, 2, 10, 5, 13, 6 and 14. In addition to these events, sharply peaked events antisymmetric in the two wings are present in signals 5, 13, 6 and 14 (see highlighted regions in Fig.6.1A). In signal 4 the latter are the dominant feature.

The least-dependent component analysis (described in section 4.6) separates events of distinct types into distinct components. Fig.6.1B shows the least-dependent components (LDCs) of the signals shown in Fig.6.1A. In this example, the separation of activation events is as follows:

i. Events symmetric in the two wings are separated in component 13.

[7] The term "input signal" or only "signal" refer to stroke position at a specific phase of the wingbeat cycle, over 2500 cycles (see Fig.6.1A). 16 such signals (8 from each wing) constitute the full set of input signals that are linearly transformed to least-dependent components (LDCs). For details see section 3.3.2.

ii. Events anti-symmetric in left and right wing (the two sharply peaked events highlighted in yellow and green in Fig.6.1A) are isolated in component 1.

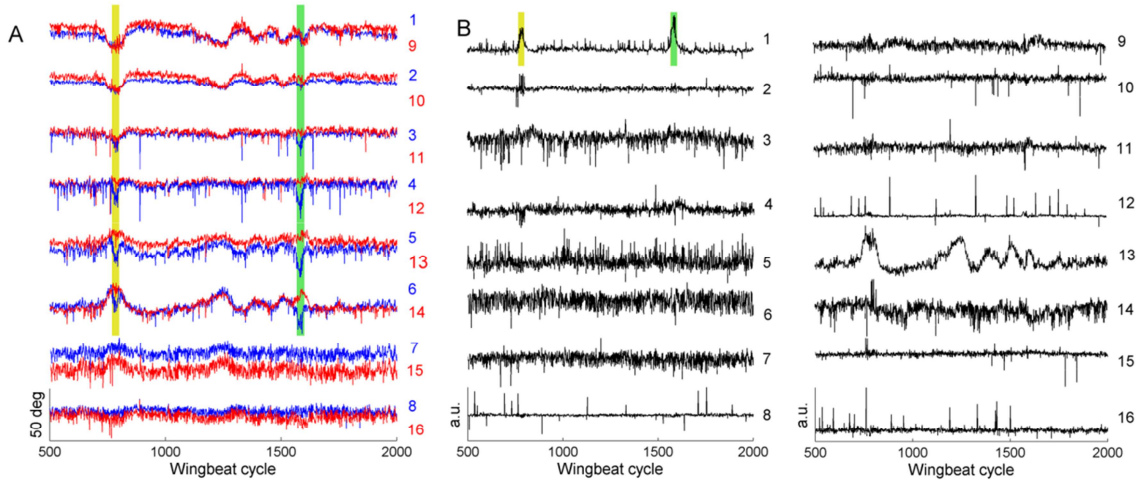

Figure 6.1: Least-dependent components separate distinct temporal features. A) 16 signals extracted from a flight segment of 2500 wingbeat cycles (the signals are numbered according to Fig.3.2A). Red: signals from left wing; Blue: signals from right wing. Yellow and green highlighted regions mark two events with pronounced variations asymmetric in the two wings. **B)** Least-dependent components of signals shown in A.

iii. Gradual drifts occurring at a timescale of many hundreds of wingbeat cycles are separated in 3rd and 14th components.

iv. Several components (8, 12, 15, and 16) consist of isolated short pulses with a duration 1-2 cycles. Such pulses arise mainly in the signals 3, 4 and 11, 12 (phases corresponding to mid-stroke) and are due predominantly to mistracking of the wing (tracking the wing vein or leg instead of wing edges – for an example see (Chakraborty et al. 2015)).

Another example is seen in Fig.4.9A. The triangular-shaped event seen early in component 9 is apparent in most of the 16 input signals (Fig.3.3B), but is isolated in only one component (Fig.4.9A). The two brief events in component 11(Fig.4.9A) do not stand out in the input signals; least-dependent analysis, however, isolates these as events of a particular type. Notice that these two events are similar in time course to the events in component 1 of Fig.6.1B (obtained from a flight recording of a different fly). This is an example of repeated occurrence of components; such components will be analyzed in detail in the last subsection.

The separation of temporal features into distinct components, illustrated in the examples given above, is a typical outcome of the LCA analysis. In rare cases, the separation fails, and several components will contain the same event. In general, however, LCA provides a powerful tool for extracting and sorting the various temporal features of the input signals, as well as for isolating experimental artifacts (Chakraborty et al. 2015).

6.2.2 The least-dependent components are statistically nearly independent

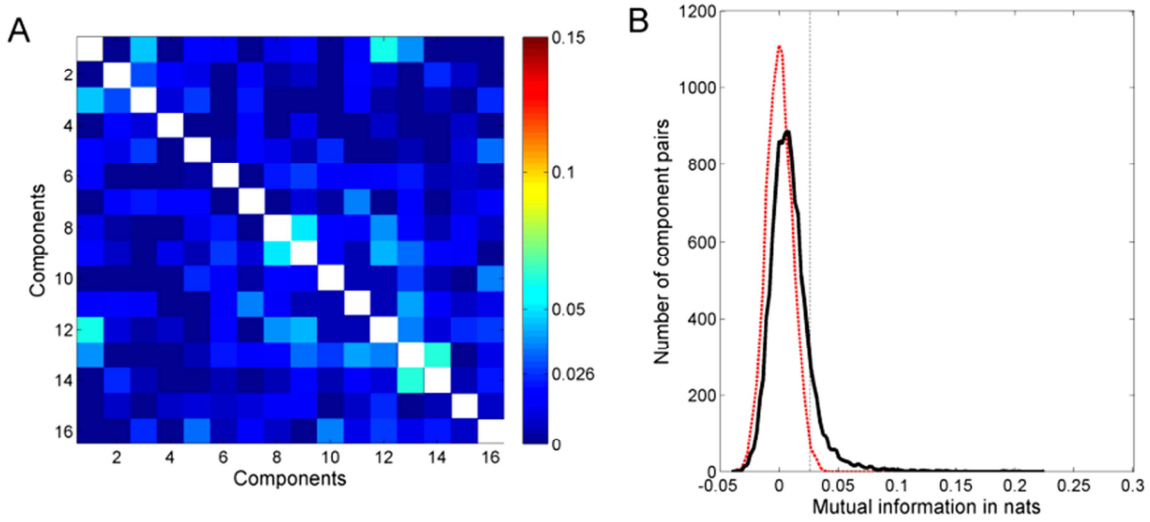

Figure 6.2: Mutual information of least-dependent components. A) Dependency matrix of the components shown in Fig.6.1. The color scale indicates the value of mutual information in nats. Values below 0.026 nats imply statistical independence. **B)** Solid black curve shows the distribution of pairwise mutual information, for pairs of components in a flight segment, over a total of 100 flight segments. Dashed red curve gives the null estimate of this distribution, obtained after randomly reshuffling the activation time course of each component. Dashed black line marks α=0.01 confidence limit for rejecting the null hypothesis of zero mutual information.

The main goal of our study was to identify kinematic patterns that are controlled independently of each other (for example, through parallel neural pathways that activate different steering muscles). If two types of kinematic patterns cannot be controlled independently, then the time courses of their activation will necessarily have some degree of statistical dependence – even during spontaneous, unstimulated flight behavior. Consequently, if the components obtained from LCA are fully statistically independent, they define candidates for elementary kinematic patterns.

The least-dependent component analysis produces the most independent linear combinations of the input signals. To evaluate if the resulting LDCs are fully statistically independent or not, it is necessary to examine their mutual information. Figure 6.2A shows the matrix of estimated pairwise mutual information for the least-dependent components in Fig.6.1B. Mutual information was calculated using Eq.4.21 and the entropies using the algorithm presented in (Kraskov et al. 2004). To determine the significance of mutual information values obtained from the estimator, the statistics of null estimates of mutual information was obtained. To do so, the time series of each of the 16 LDCs from a given flight segment was randomly reshuffled to destroy any residual dependence with other components and then the pairwise mutual information was estimated. The distribution of this null estimate calculated from 100 flight segments (12000 pairs of LDCs) is shown in figure 6.2B (red dashed line). Based on this distribution (fitted to a Gaussian distribution with zero mean), only values above 0.026 nats[8] were considered as significant (α value of 0.01). In the example in figure 6.2A, all but 10 of the 120 pairs of components have mutual information less than 0.026 nats and hence are pairwise statistically independent. 9 out of the remaining 10 pairs (1-3, 1-13, 5-16, 7-11, 8- 9, 8-12, 9-12, 11-13 and 13-14) have mutual information less than 0.04 nats, which is only nominal statistical dependence. Only one pair (i.e. 1-12) has significant mutual information of 0.06 nats. To obtain a similar statistics for the entire set of 100 flight segments, pairwise mutual information of LDCs from individual segments were estimated (12000 pairs of LDCs). The solid black line in Fig.6.2B shows their distribution. 95.5% of pairs were statistically independent and only 0.5% shared mutual information greater than 0.1 nats, testifying that components with large statistical dependence are rare.

6.2.3 Statistical analysis allows to decompose complex stroke trajectories into elementary kinematic patterns

As discussed above, events with distinct time courses are typically separated into distinct components. These distinct types of events occasionally overlap in time. An example seen in components 1 and 13 from Fig.6.1B is shown again in Fig.6.3A for clarity.

[8] Depending on the base of the logarithm in the definition of entropy (see section 4.6.1, footnote 6), entropy is expressed either in bits (base 2) or nats (base e). The conversion factor is: 1 nat = (1 / ln 2) bits = 1.44 bits.

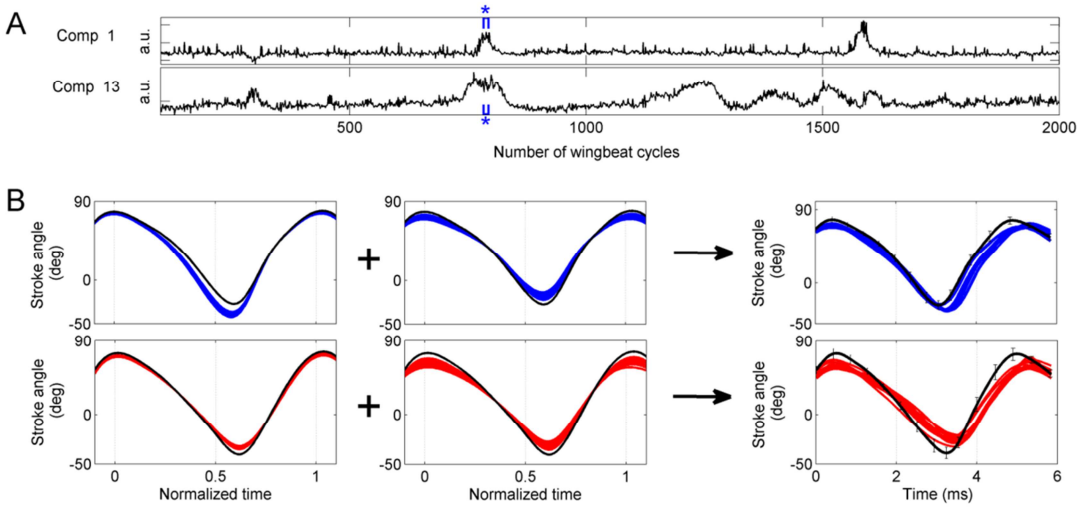

Figure 6.3: Complex changes in stroke trajectory resolved into elementary kinematic patterns. **A)** Activation time course of two kinematic patterns (components 1 and 13 from Fig.6.1B). **B)** Left panel: 10 consecutive cycles (marked with brackets and asterisk symbol in A) of wing stroke deformation reconstructed from only component 1. The reconstructed phase points (not shown for clarity) were interpolated with cubic splines. Blue: left wing, red: right wing. The black line shows the baseline wing stroke. Middle panel: 10 consecutive cycles (marked with brackets and asterisk symbol in A) of wing stroke deformation reconstructed from only component 13. Right panel: Wing stroke trajectories during these 10 cycles. The trajectory deformation in the right panel is resolved into a linear combination of laterally symmetric and antisymmetric deformations.

Events in these two components have distinct time scales; moreover, events in component 1 are accompanied by correlated changes in wingbeat period, whereas those in component 13 are not (correlation coefficients 0.68 and 0.08, respectively). The time courses of these two components are statistically nearly independent (the mutual information evaluated over the whole flight segment of 2500 wingbeat cycles is 0.04 nats). Some activation events, however, occur simultaneously: the first major event in component 1 overlaps in time with a major event in component 13. The stroke deformation modes encoded by components 1 and 13 are shown in the left and middle panels of Fig.6.3B. Component 1 encodes for a change in ventral amplitude that occurs antisymmetrically in the left and right wing, while component 13 encodes a decrease in stroke amplitude occurring symmetrically in both wings. The right panel of Fig.6.3B shows the recorded wing stroke trajectories of 10 wingbeat cycles (marked with blue bracket and asterisk in Fig.6.3A), compared to the baseline trajectory (black). The recorded strokes deviate from the baseline stroke by asymmetric changes in ventral and dorsal amplitudes combined with an increase in stroke duration.

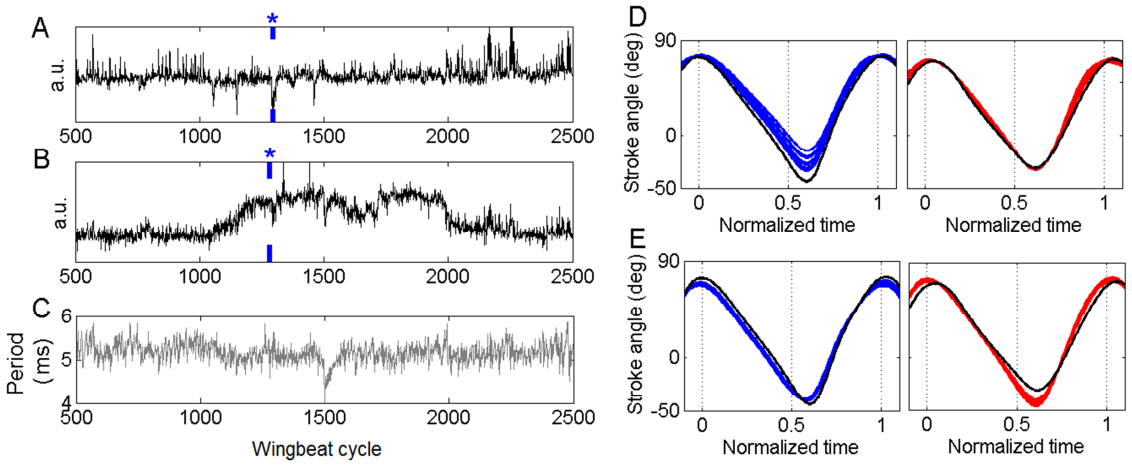

Figure 6.4: Simultaneously active stroke deformation modes of type I and type III kinematic patterns. A) Activation time course of a type I kinematic pattern, with typical spiky activation events. **B)** Activation time course of the type III kinematic pattern in the same flight segment, with a long-duration activation event lasting from cycle 1100 to cycle 2000. Note that some activation events in A occur simultaneously with the long-duration event in B. **C)** Time course of the wingbeat period, which is not correlated with the activation time courses in A and B. **D)** 10 consecutive reconstructed stroke cycles (from the time window marked with blue bracket and asterisk sign in A) with only the type I stroke deformation mode included (blue: left wing; red: right wing). Black lines show the baseline wing stroke. **E)** 10 consecutive reconstructed stroke cycles (from the time window marked with blue bracket and asterisk sign in B) with only the type III stroke deformation mode included.

Based only on this information, it would not be possible to deduce that such a complex deviation is generated by a specific linear combination of more fundamental, independently controlled stroke deformation modes. Based on our statistical analysis, however, we can conclude that the deformation of the stroke trajectory shown in the right panel of Fig.6.3B is a composite of the elementary stroke deformation modes shown in the left and middle panels of Fig.6.3B. This conclusion is possible only after examining (using LCA) the entire segment of 2500 cycles, in which the elementary stroke deformations are seen to occur independently of each other. Similar cases of composite kinematic changes that arise as a superposition of several elementary kinematic patterns are encountered also in other examined flight segments. A second example is shown in figure 6.4.

6.2.4 Classification of frequently obtained least-dependent kinematic patterns

In total, 100 flight segments from 10 flies were analyzed. LCA was carried out in each of these segments, generating a set of $16 \times 100 = 1600$ least-dependent components, each corresponding to a separating vector. Kinematic patterns with certain features were found repeatedly within this set. These kinematic patterns represent stroke deformation modes exercised frequently by different flies, and can thus be presumed to be important for flight control. To characterize such kinematic patterns I classified them into well-defined types. I first divided the kinematic patterns into those showing distinct temporal features and those resembling broad-band noise. As an example, consider the set of components shown in Fig.4.9A. The activation time course of component 14 appears featureless, while for component 15 it is dominated by randomly occurring single cycle jumps. As seen in Fig.4.9B, the Welch power spectra for both these components are flat. Such components were viewed as not relevant for flight control, and were dropped from further analysis. To quantify the spectral flatness, I estimated the Wiener entropy (WE), defined as the ratio of the geometric mean to the arithmetic mean of the spectral density. WE ranges from 0 for sinusoidal waveforms to 1 for white noise. For the components shown in Fig.4.9A, WE vary between 0.19 and 0.93 (see values given in Fig.4.9B). For WE higher than 0.9, the spectrum is visually indistinguishable from a flat one. I chose 0.9 as the threshold value to declare a component to be broadband noise. On average only 12 components per segment were found to have temporal structure, while the remaining 4 had WE greater than 0.9. Among the kinematic patterns with temporal structure, the ones occurring repeatedly in distinct flight tests of the same fly and in different flies were classified. A kinematic pattern was classified as frequently occurring if it was observed in at least 3 out of the 10 analyzed flies. Three supersets of these components can be defined based on the type of their characteristic features:

A. Kinematic patterns characterized by prominent activation events in their time course.
B. Kinematic patterns characterized by dominance of specific signals in their separating vector.
C. Kinematic patterns characterized by spectral density peaks at particular frequencies.

These supersets are not mutually exclusive – a minority of the kinematic patterns belongs to more than one category. The kinematic patterns in each of these supersets can be further divided into several classes. Below I first state (for each type of kinematic pattern) its defining feature. Following this, I discuss additional properties of these kinematic patterns, and list functional interpretations of the stroke deformation modes that they encode. The precise algorithmic criteria for assigning a given component to one of the 7 types is available as supplementary material with (Chakraborty et al. 2015).

A. Kinematic patterns characterized by typical events in the activation time course

Type I: For these kinematic patterns, the time course is dominated by characteristic events of activation with a time scale of 40 to 100 wingbeat cycles. A typical example is shown in Fig.6.5A. Component 1 in Fig.6.1 and component 11 in Fig.4.9 also belong to this type (the 3 examples were obtained from 3 individual flies). This type of component has a very low correlation with the wingbeat period (Pearson coeff. <0.2).

The corresponding stroke deformation modes consist of an increase in ventral amplitude for one wing and a simultaneous decrease for the other wing. 10 successive reconstructed stroke cycles during a typical activation event are shown in Fig.6.5B. Such a stroke deformation mode is expected to generate yaw torque (see Discussion, section 6.4.2). The duration (300-500ms) and the form of these events (Fig.6.5A) match the time course of yaw torque measured for spontaneous saccades during tethered flight (Heisenberg and Wolf 1979; Tammero and Dickinson 2002).

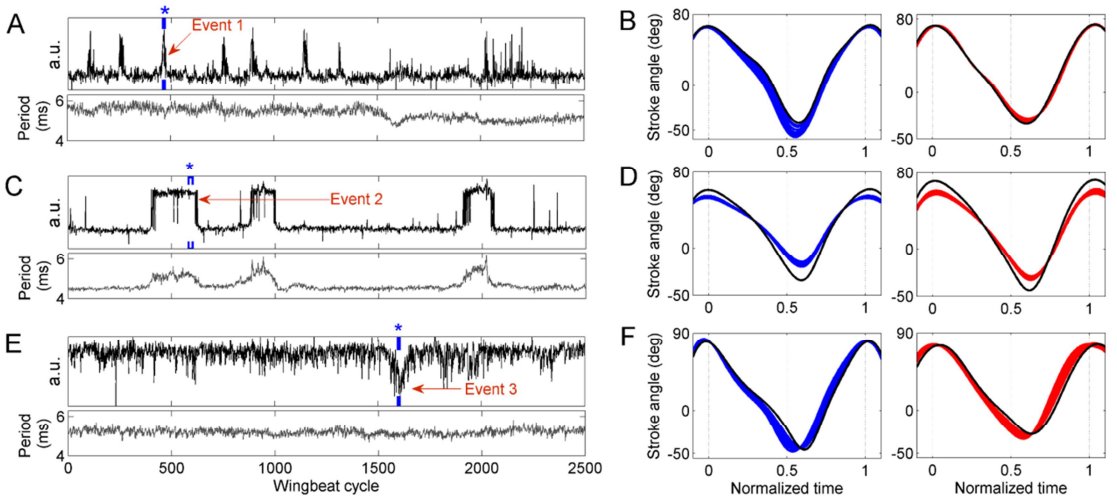

Figure 6.5: Least-dependent kinematic patterns of types I, II and III. A) Activation time course of a type I kinematic pattern (black trace). A typical activation event is marked as Event 1. The lower subpanel shows the wingbeat period (gray trace) during this flight segment. **B)** 10 superposed cycles of wing stroke deformation reconstructed from only the kinematic pattern shown in A (blue: left wing; red: right wing; time window marked with blue bracket and asterisk sign). Black lines show the baseline wing stroke. **C)** Activation time course of a type II kinematic pattern (black trace). A typical activation event is marked as Event 2. The lower subpanel shows the wingbeat period during this flight segment (gray trace). **D)** 20 superposed cycles of wing stroke deformation reconstructed from only the kinematic pattern shown in C (markers as in B). **E)** Activation time course of a type III kinematic pattern (black trace). A typical event is marked as Event 3. The lower subpanel shows the wingbeat period during this flight segment (gray trace). **F)** 10 superposed cycles of wing stroke deformation reconstructed from only the kinematic pattern shown in E (markers as in B).

Type II: The time course in this type of kinematic patterns is correlated (Pearson coeff. >0.45) with changes in wingbeat period. Figure 6.5C shows such a component, with three sharply defined activation events. During these events only the overall stroke duration changes, while the ratio of downstroke to upstroke duration remains unaltered.

The corresponding stroke deformation modes involve a symmetric change in stroke amplitude of both wings. 20 successive reconstructed stroke cycles during one activation event are shown in Fig.6.5D. Such a stroke deformation is expected to alter the total flight force (lift and/or thrust) – see Discussion section 6.4.2.

Type III: These kinematic patterns are dominated by activation events with a time scale of 40 to a few hundred wingbeat cycles, during which the ratio of downstroke to upstroke duration is significantly altered. A typical activation time course is shown in Fig.6.5E.

In these kinematic patterns, the stroke deformation may also involve a change in stroke amplitudes. The change in downstroke-to-upstroke ratio and in the amplitude can be

bilaterally symmetric or asymmetric. In some cases, this stroke deformation is coupled with a change in wingbeat frequency. 10 successive reconstructed stroke cycles during an activation event are shown in Fig.6.5F. Such a stroke deformation, if symmetric in both wings, is expected to result in altered pitch torque (see Discussion, section 6.4.2).

B. Kinematic patterns characterized by the dominance of specific contributing signals

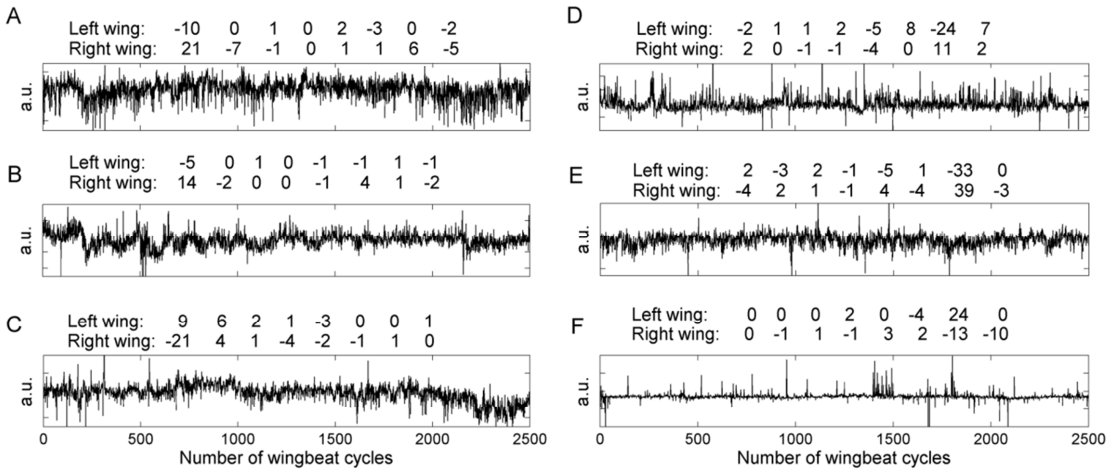

Figure 6.6: Least-dependent kinematic patterns characterized by specific separating vectors. A–C) Activation time course in type IV kinematic patterns. **D–F)** Activation time course in type V kinematic patterns. Examples from 3 different flies are shown for each type. The corresponding separating vectors are printed in two rows for ease of visualization. The vectors are scaled to operate on signals with unit variance (see the main text).

Most of the recurring components are linear combinations that include the majority of the 16 phase points. However, two unusually simple linear combinations were seen to occur repeatedly:

Type IV: These LDCs are dominated by the difference of wing stroke positions at dorsal stroke reversal. Time courses of type IV kinematic patterns from 3 flies are shown in figure 6.6A, B and C together with their separating vectors (coefficients of the linear combination).

Type V: These LDCs are dominated by the difference of wing stroke positions at mid-upstroke. See figure 6.6D, E, F for examples. The separating vectors shown in Fig.6.6 are

scaled to operate on signals of unit variance so that they directly show the relative contribution of the variability of each phase point in constructing the given LDC. The temporal features appearing in components of type IV and V do not have a consistent pattern. The activation time courses in some of these kinematic patterns are nearly spectrally flat (WE> 0.7). These properties suggest that the kinematic patterns corresponding to these two components might not be involved in flight control (see also Discussion).

C. Kinematic patterns characterized by spectral density peaks at particular frequencies

To characterize the time scales that dominate the activation time course of a given kinematic pattern, it is useful to examine its power spectrum. For most of the frequently recurring kinematic patterns, the Welch spectral density (section 4.2.1) of the time course has high power at low frequencies (<0.05/cycle) and is relatively flat at high frequencies (>0.1/cycle), as in the top three panels in Fig.4.9B. Two specific types of deviations from this usual pattern were seen to occur repeatedly and the corresponding kinematic patterns are classified as type VI and VII.

Type VI: For these kinematic patterns, the power spectrum of the activation time course is dominated by the highest frequencies. The power density increases by about an order of magnitude between frequency 0.35/cycle and 0.5/cycle (the Nyquist frequency). The activation time course contains intermittent intervals during which a period-2 pattern develops: the magnitude increases and decreases in successive cycles. In contrast to other types of kinematic patterns, multiple type VI components frequently co-occurred in a flight segment. As an example, Fig.6.7A shows 3 components obtained from a single flight segment. The period-2 patterns do not occur in all three components simultaneously. Figure 6.7B shows the power spectra.

The stroke deformation mode of this type encodes significant symmetric changes in ventral amplitude and varying amounts of changes in the rest of the wing stroke. The exact waveform of the wing stroke varies between components. The stroke deformation modes corresponding to the 3 components in Fig.6.7A (in the highlighted intervals) are shown in

figure 6.7C, D. Their superposition results in somewhat different wing strokes during the two intervals.

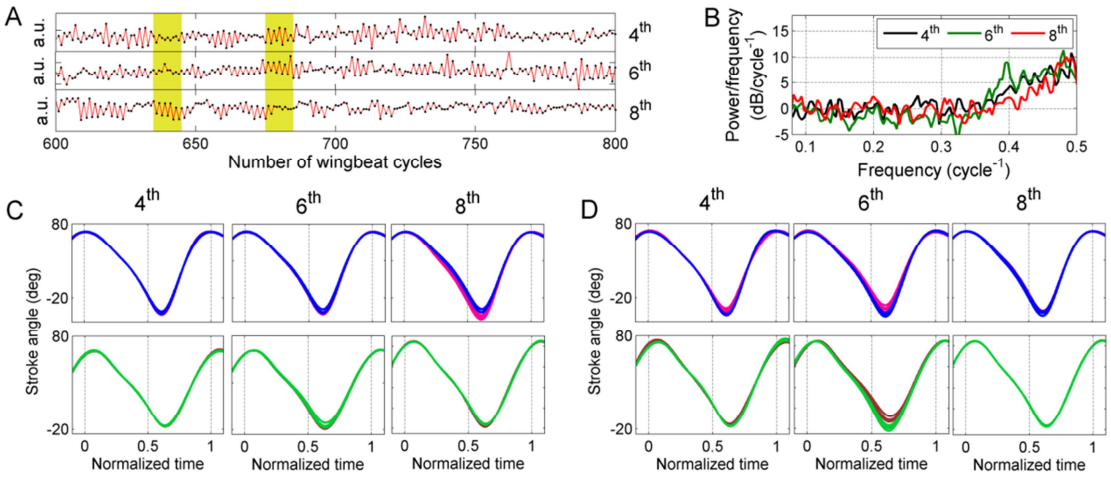

Figure 6.7: Least-dependent kinematic patterns with 2 cycle periodicity in the activation time course (Type VI). A) Activation time course in 3 kinematic patterns of type VI (only 200 wingbeat cycles shown for clarity). **B)** Welch power spectra of the time courses shown in panel A. **C)** 10 consecutive cycles of wing stroke deformation reconstructed from each of the 3 kinematic patterns in A, during the left highlighted interval (upper row: left wing; lower row: right wing). **D)** 10 consecutive cycles of wing stroke deformation during the right highlighted interval in A. Odd-numbered and even-numbered cycles are plotted in different colors. The regular alternation of ventral amplitude between higher and lower values in successive cycles is best visible in C, right column and D, middle column.

Type VII: For these kinematic patters, the power spectrum of the activation time course has a dominant peak at the frequency of 0.02/cycle. The time course is periodically modulated, with a period of 40-50 wingbeat cycles – see figure 6.8A, B. In the flight segments that contained these components, typically only one or at most two type VII components occurred.

For these kinematic patterns, the stroke deformation modes did not show any commonality. For example, component 4 in Fig.6.8A encodes changes in dorsal amplitude whereas component 13 encodes changes in ventral amplitude of the opposite wing (Fig.6.8C and D, respectively). Note also that the periodic modulations in these two components are not fully synchronized.

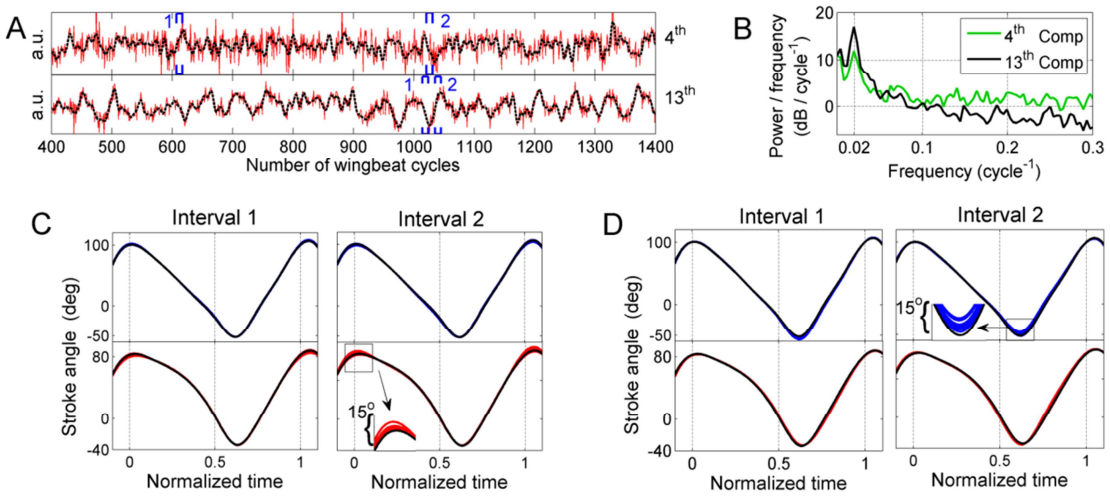

Figure 6.8: Least-dependent kinematic patterns with 40 to 50 cycle periodicity in the activation time course (Type VII). A) Activation time course in two kinematic patterns of type VII, obtained from the same flight segment (black dashed line: low-pass-filtered time course as visual guide). B) Welch power spectra of the time courses presented in A. C) 10 superposed cycles of wing stroke deformations reconstructed from kinematic pattern 4 (blue: left wing; red: right wing). Interval 1 and interval 2 refer to the time windows marked in the upper subpanel of A. The dorsal amplitude of the reconstructed right wing stroke decreases from the baseline value by about 5° in the 1st interval and increases by a similar amount in the 2nd. The reconstructed left wing stroke does not show any deviation from the baseline wing stroke. D) 10 superposed cycles of wing stroke deformations reconstructed from kinematic pattern 13 (otherwise as in C). In this kinematic pattern, the ventral amplitude of the reconstructed left wing stroke increases (in the 1st interval) and decreases (in the 2nd interval) from the baseline value by about 5°.

Figure 6.9A shows a summary of the classification, and gives the number of flies and flight segments in which the kinematic patterns of a particular type were found. Kinematic patterns of types I, II and V are the most commonly occurring ones. Kinematic patterns of type VI, with the striking period-2 pattern of activation, were found in 6 of the 10 examined flies. Fig.6.9B gives the full distribution of occurrences of the classified patterns in the 100 analyzed flight segments.

To evaluate the sensitivity of our results to the number of flies analyzed, we examined how many of the patterns in Fig.6.9B would be classified as frequently occurring within batches of fewer flies. We obtained batches of 5, 6,7,8,9 or 10 flies by subsampling from the measured set of 10 flies (with repetition allowed). A kinematic pattern was declared frequent if it appeared in at least 25% of the flies in a given batch (e.g., in 2 out of 8 flies or in 3 out of 10 flies). In Fig.6.9C, we show the distribution of the number of such frequent patterns in all batches of a given size. It is seen that even in batches of 7 flies, the most

frequently found number of classified types of patterns is 7 (identical to the number we obtained from the full set of flies). For batches of 5 flies, however, the most frequently found number of patterns is 6 – i.e., had we worked with only 5 flies, we would have likely missed one of our 7 classified types of patterns. (For batches of 6 flies, finding 6 patterns or 7 patterns is approximately equally likely). We cannot exclude that additional types of classified patterns would have been found had we worked with more than 10 flies. The repeatability of the classified patterns in recordings from an individual fly can be judged from Fig.6.9B. To summarize this repeatability, we defined a simple measure as follows. For each pair of flight segments from a given fly, we counted the number of classified types of patterns that occurred in both flight segments. The average of these counts over all pairs of segments from a given fly gives a number between 0 and 7, with 0 indicating no repeatability and 7 perfect repeatability of the classified patterns. These averages, as well as the minimal and maximal counts, are shown individually for all 10 flies in Fig.6.9D. It is seen that typically, only 1 or 2 classified types of kinematic patterns are shared by a randomly chosen pair of flight segments. At most 4 types of patterns were found to co-occur in a pair of segments.

Figure 6.9: Classification summary and repeatability of kinematic patterns. A) 1600 kinematic patterns from 100 flight segments (measured in 10 flies) were first divided into kinematic patterns with and without temporal features in the activation time course. Among kinematic patterns with temporal features, the ones occurring frequently were further classified into 7 types (for classification criteria see (Chakraborty et al. 2015)). **B)** Distribution of the 7 classified types of kinematic patterns (filled boxes) among the 100 flight segments. Horizontal lines separate individual flies. **C)** Given the distribution of kinematic patterns in B, the probability of finding a given number of frequently occurring kinematic patterns when a randomly selected sub-sample of the flies is analyzed. Legend indicates the number of flies in the sub-sample. **D)** The number of types of classified kinematic patterns that co-occur in a pair of flight segments from a given fly. Filled circle: the number of co-occurring types averaged over all pairs of flight segments; bar: the range of the number of co-occurring types. For details see text.

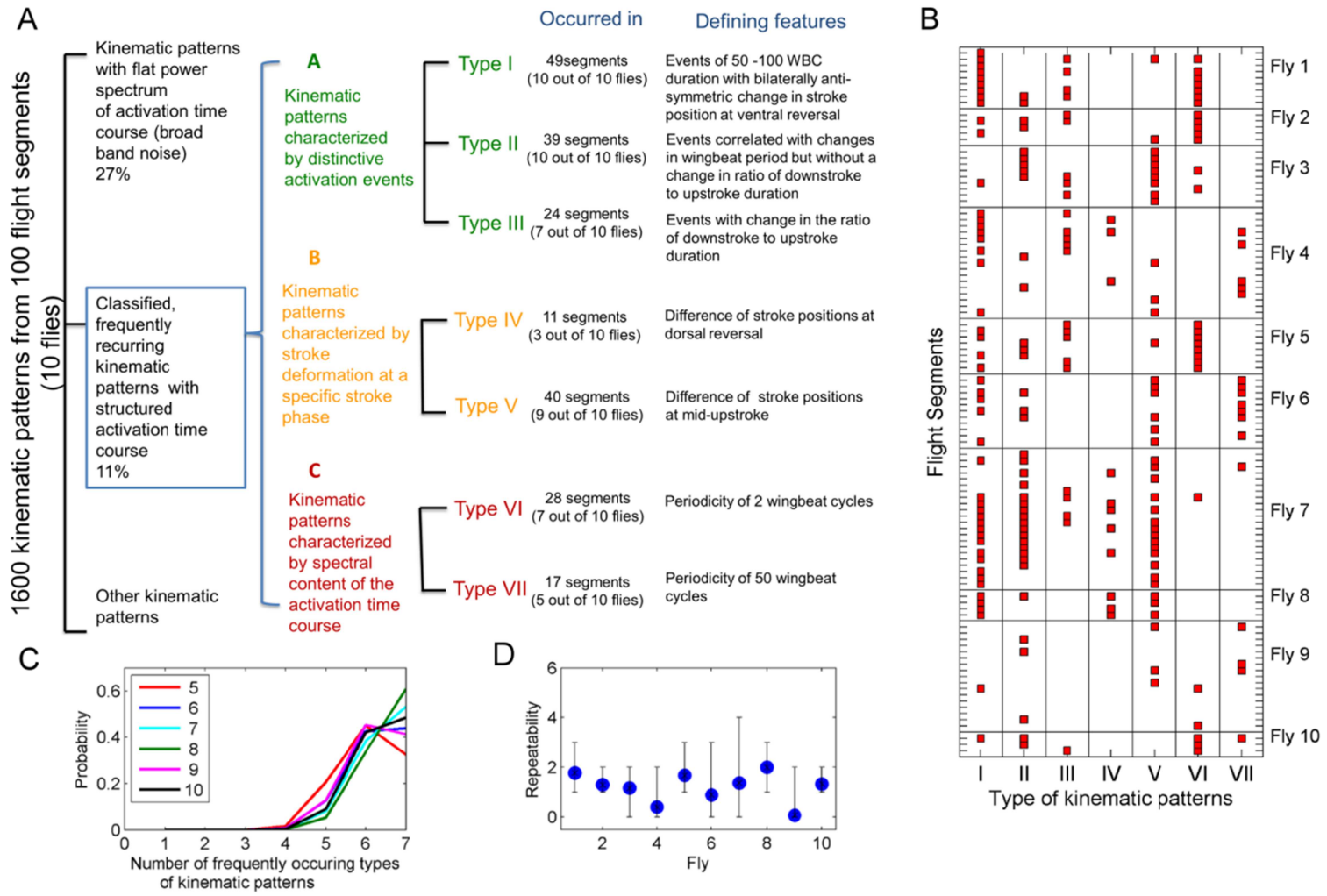
A
1600 kinematic patterns from 100 flight segments (10 flies)
Kinematic patterns with flat power spectrum of activation time course (broad band noise) 27%
Classified, frequently recurring kinematic patterns with structured activation time course 11%
Other kinematic patterns
A
Kinematic patterns characterized by distinctive activation events
B
Kinematic patterns characterized by stroke deformation at a specific stroke phase
C
Kinematic patterns characterized by spectral content of the activation time course
Occurred in
Defining features
Type I
49segments (10 out of 10 flies)
Events of 50 -100 WBC duration with bilaterally anti-symmetric change in stroke position at ventral reversal
Type II
39 segments (10 out of 10 flies)
Events correlated with changes in wingbeat period but without a change in ratio of downstroke to upstroke duration
Type III
24 segments (7 out of 10 flies)
Events with change in the ratio of downstroke to upstroke duration
Type IV
11 segments (3 out of 10 flies)
Difference of stroke positions at dorsal reversal
Type V
40 segments (9 out of 10 flies)
Difference of stroke positions at mid-upstroke
Type VI
28 segments (7 out of 10 flies)
Periodicity of 2 wingbeat cycles
Type VII
17 segments (5 out of 10 flies)
Periodicity of 50 wingbeat cycles
B
Flight Segments
Fly 1
Fly 2
Fly 3
Fly 4
Fly 5
Fly 6
Fly 7
Fly 8
Fly 9
Fly 10
I II III IV V VI VII
Type of kinematic patterns
C
Probability
0 0.2 0.4 0.6
5 6 7 8 9 10
0 1 2 3 4 5 6 7
Number of frequently occuring types of kinematic patterns
D
Repeatability
0 2 4 6
2 4 6 8 10
Fly

6.3 Results II: Kinematic pattern controlled at the time scales of a single wing stroke

This section starts (6.3.1) with a general comparison of the wing stroke parameters between the group of flies with intact halteres and that with both their halteres ablated. Section 6.3.2 characterizes the special kinematic pattern on which I focused this part of my study and in section 6.3.3 I describe the effect of haltere ablation on these specific kinematic patterns. In section 6.3.4 I discuss the results obtained in this part of the study.

6.3.1 Overall kinematic parameters

Table 6.1: Basic average wing stroke parameters in each fly of the two groups.

Fly	Halteres	Amplitude (deg.) (Mean ± std)	Frequency (Hz) (Mean ± std)	Downstroke-to-upstroke ratio (Mean ± std)
1	Untreated	107±22	191±10	1.26±0.1
2	Untreated	153±9	172±5	1.36±0.1
3	Untreated	152±8	187±6	1.43±0.1
4	Untreated	151±10	203±9	1.43±0.1
5	Untreated	165±8	146±3	1.54±0.2
Overall		**142±22**	**182±20**	**1.4±0.15**
6	Ablated	85±6	240±20	1.17±0.1
7	Ablated	106±8	243±7	1.29±0.1
8	Ablated	116±16	248±15	1.24±0.1
9	Ablated	108±11	247±10	1.45±0.1
10	Ablated	113±16	232±12	1.35±0.1
Overall		**110±15**	**241±13**	**1.31±0.12**

I first compared the most frequently studied parameters of the wing strokes i.e., stroke amplitude, stroke duration and the downstroke-to-upstroke ratio, between the two groups of flies. Table 6.1 lists the average value of these parameters for measured test flights from individual flies. The group with both their halteres ablated have significantly different wingbeat frequency (241±13 Hz) as compared to the untreated flies (182±20 Hz) (KS test, $p<0.05$). The average wingbeat frequency of the haltere ablated flies is 32% higher than that of untreated flies, similar to that reported previously in Drosophila (Dickinson 1999; Bartussek and Lehmann 2016). In addition to the change in baseline frequency I also noted about 26% (Table 6.1) decrease in average wingbeat amplitude in haltere ablated flies (KS test, $p<0.05$). It is not to say that the haltere ablated flies cannot beat their wings at stroke amplitudes comparable to that of untreated flies; amplitudes around 160 degrees are also attained by haltere ablated flies, but only for few cycles (for example of such an interval see Fig.6.11B).

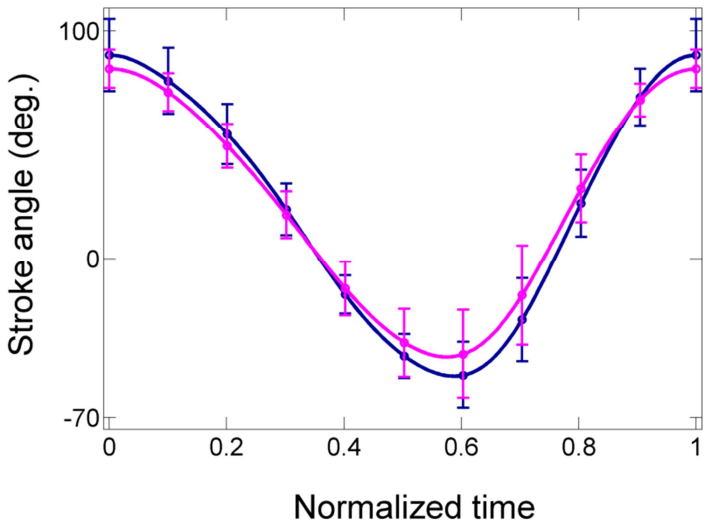

Figure 6.10: Average stroke trajectory of untreated and haltere ablated flies. Average trajectory of ~$5x10^5$ strokes measured from 5 untreated flies (blue) and ~$2.5x10^5$ strokes measured from 5 haltere ablated flies (pink). Error bars on both the traces show the standard deviation at the marked phases of the stroke. Time axis normalized to unit stroke duration.

Other than the above mentioned changes in the stroke parameters the overall shape of the stroke trajectory remained largely unaltered. This result was partially drawn from the fact that the average downstroke-to-upstroke ratio (Table 6.1) is statistically similar in the two groups of flies (KS test $p<0.05$). In addition, the average[9] shape of the stroke trajectories measured in haltere ablated flies when compared with that of untreated flies showed no

[9] each stroke cycle was first normalized to unit stroke duration and then the stroke angle at each phase point was averaged over all measured stroke cycles from the flies in the respective group.

obvious distortion (for example, the kind of distortion shown in figure 4A of (Fry et al. 2005)). Mean and the standard deviation of the stroke position at each phase point are shown in Fig.6.10. However, the variance near the ventral reversal phase of the stroke trajectories in case of haltere ablated flies is about twice as that of untreated flies.

6.3.2 Characterizing the recurring single cycle stroke deformations

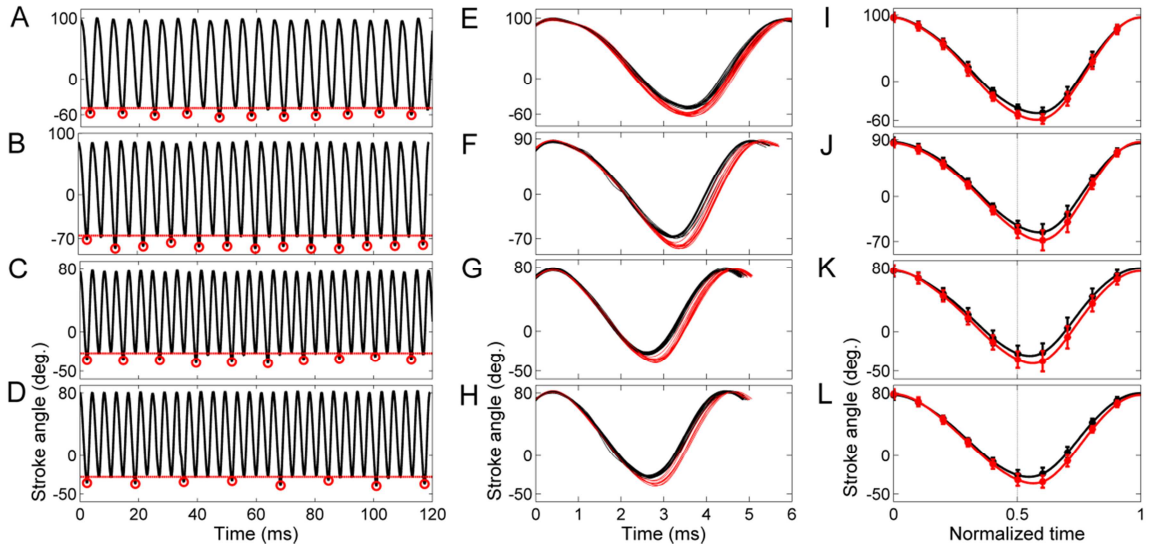

Figure 6.11: Kinematic patterns with recurring characteristic single cycle stroke modification. A- D) Time course of stroke position (right wing) showing the recurrence of a characteristic trajectory modification in every 2 strokes (A, B), 3 strokes (C) and 4 strokes (D). A: untreated fly; B, C D: haltere ablated flies. Recurring special strokes are marked with red circles in each case. **E-H)** Superposed stroke cycles from the intervals shown in A-D respectively. Strokes with the characteristic trajectory modifications (marked with red circles in A-D) are plotted in red and rest of the strokes are in black. **I-L)** Average shape of the stroke trajectory with ventral amplitude jump (red) and the immediate preceding stroke (black), pooled from all the data-based prototypical events of a given periodicity. Time axis of each stroke is normalized to unit stroke duration. Error bars show the standard deviation at the marked phase of the trajectory.

As discussed in section 6.2.4 (Type VI), the kinematic patterns with sub-harmonic variations comprise of single cycle stroke deformations that recur periodically for a stretch of a few dozens of wingbeat cycles. In my data set from the two groups of flies (i.e. normal and haltere ablated flies) I found episodes with recurrence periods of 2, 3 and 4 wing strokes. To study the properties of the recurring stroke trajectories I isolated the episodes of their occurrences in the measured flight segments. Details of the screening procedure are discussed in section 4.4.2; here I briefly mention the main steps. As these stroke

deformations always involve changes near the ventral reversal, I used the ventral amplitude time series to identify the intervals with sub-harmonic variations. The ventral amplitude time series of each flight segment was analyzed using a non-stationary frequency analyses method, called wavelet analysis (Morlet wavelet transform at pseudo frequencies of 0.5, 0.33 and 0.25 $cycle^{-1}$). This transform is such that the coefficients have high magnitudes at the specific intervals where 2, 3 or 4 cycle periodic variations exist. Intervals where the coefficient values exceeded the estimated thresholds for each periodicity were extracted. The ventral amplitude variations during these isolated intervals were further checked against a set of criterion defining prototypical events for each sub-harmonic variation. The prototypical events so isolated were then saved in a database.

Figure 6.11 shows examples of stroke trajectories during the prototypical events of the sub-harmonic variations. The stroke cycles with abrupt increase in ventral amplitude are marked by red circles at the ventral reversal phase in the stroke trajectory (Fig.6.11A-D). To look closely into the change in trajectory shape during these special stroke cycles and its variability within the selected interval, I superposed all the stroke cycles during the event (Fig.6.11E-H). The stroke trajectories marked by red circles in (Fig.6.11A-D) are plotted in red in (Fig.6.11E-H). The shape of these special stroke trajectories are seen to be highly similar. The deviation of the trajectories in red from that in black always comprises of a sudden increase in ventral amplitude. This change is accompanied by a variable degree of change in stroke duration. Details of the correlation between the changes in ventral amplitude and that of the stroke duration are discussed in a later subsection. However, for most of the recurring characteristic stroke cycles, the stroke duration as estimated from one dorsal reversal to the next and the ventral amplitude are seen to increase simultaneously. The downstroke-to-upstroke ratios for the two types of trajectories (black and red) do not show any statistically significant difference. The third column of figure 6.11 (i.e. I-L) shows the mean traces of these special stroke trajectories (red) and that of the immediate preceding stroke (black) from all the databased prototypical events of each type. As different flies have different wingbeat frequencies, to make sure that the stroke angles are averaged at the same phase of stroke cycle I normalized the time axis to unit stroke duration to make sure that the stroke cycles are averaged at the same phases. The error bars show the standard deviation at the marked phase of the trajectory. It is seen that the kind of trajectory change during these special cycles is not only consistent within a single

event (as seen in Fig.6.11E-H), but across all the events selected from the individual flies of a given group (as seen in Fig.6.11I-L). This shows that all the prototypical events characterized by the same periodic variation of the ventral amplitude and extracted from either of the two groups of flies belong to a single type of kinematic pattern. Further if the kinematic patterns with different sub-harmonic variations (Fig.6.11 I-L) are mutually compared the trajectory deviations from the black to the red trace comprise of the same basic changes.

However, a major drawback of the wavelet analysis based algorithm is that the coefficients at all the scales increase considerably at instances of large abrupt changes in the time series. At low frequencies, due to decrease in temporal resolution, high coefficient values at such jumps persist over broader time intervals and are occasionally mistaken for events of sub-harmonic variations. Cases of such erroneously selected events are rare for the period 2 variations and less than 5% for the period 3 variations. However, for the 4 cycle periodic variations the number of such erroneous events was found to be comparable to the number of real events. Hence, for all further statistical characterization of the sub-harmonic events, the ones with 4 cycle periodic variations have not been used.

Ventral amplitude jumps of the characteristic stroke deformations have a well-defined range of magnitude

An important characteristic feature of this kinematic pattern is the consistency of the ventral amplitude jump magnitudes across all the events of a given fly. To compare the ventral amplitude changes I estimated the magnitude of jump from one cycle to the next for all the prototypical events of each type. Figure 6.12 shows the scatter plots of pairs of consecutive ventral amplitude (VA) jumps. Such scatter plots of system variables are called Poincare plots and are widely used to study the short time scale dynamics of the system. In this case, the Poincare plots of VA jumps have been used to study the cycle-by-cycle dynamics of the wings, during the short intervals of the events. Subplots A, B show the Poincare plots for the 2 cycle periodic events obtained from the left (A) and the right (B) wings of fly 2. Both the plots show two distinct clusters in the second and the fourth quadrant. For the left wing (Fig.6.12A) the clusters are centered at (-5˚, 5˚) and (5˚, -5˚). This implies that during these events, whenever the ventral amplitude increases by about 5˚ w.r.t its previous stroke cycle, in the next stroke cycle it decreases by almost the same amount.

An example of the pairs of VA jumps that populate these two clusters is shown in Fig.6.12D. Similarly for the right wing (Fig.6.12B) the ventral amplitudes increase and decrease by a value close to 10˚ in alternate stroke cycles. This difference between the absolute values of the VA jumps of the two wings is because for fly 2 in general (i.e. even outside the selected events of interest) the left wing spanned a smaller angular range (-49˚ to 99˚) than the right wing (-52˚ to 99˚). Fig.6.12C shows the Poincare plot for VA jumps in 2 cycle periodic events from all the 5 untreated flies. The two distinct clusters in the second and the third quadrant indicate the presence of similar discrete VA jumps for all the untreated flies. The spread along the main axis of the distribution is because different flies (or even two wings of the same fly) have slightly different absolute values of the jumps.

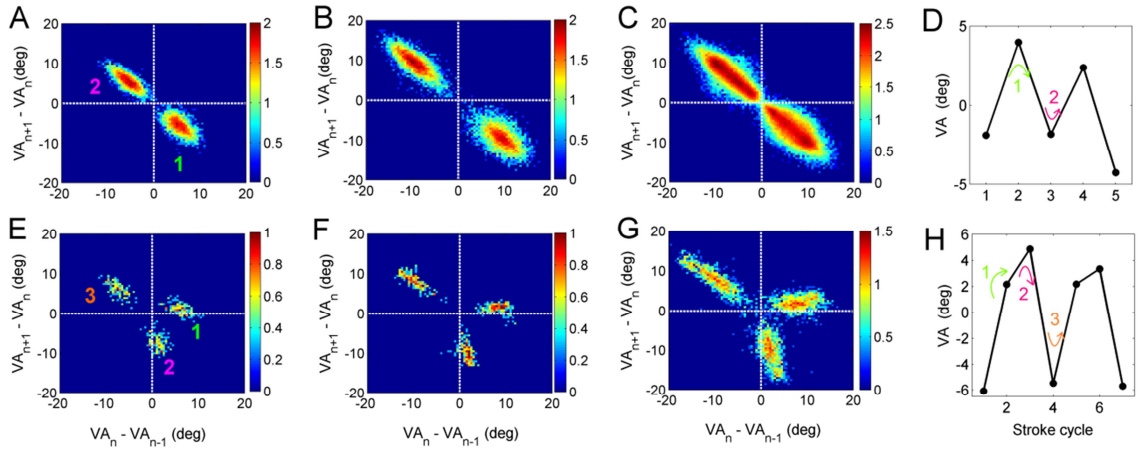

Figure 6.12: Poincare plots of high-pass filtered ventral amplitudes during databased events of subharmonic variations. A-B) Events with 2 cycle periodic variations from left wing (A) and right wing (B) of fly 2. Color axis shows the number of stroke cycles (log scale, base 10) at each position of the Poincare plot. **C)** Prototypical events with 2 cycle periodic variations from all 5 untreated flies (events from both the wings pooled together). **D)** An example of ventral amplitude jumps during a period 2 event, demonstrating the type of jumps that populate the two clusters in A-C. **E-F)** Prototypical events with 3 cycle periodic variations from left wing (E) and right wing (F) of fly 7. **G)** Prototypical events with 3 cycle periodic variations from all 5 haltere ablated flies (events from both the wings pooled together). **H)** An example of ventral amplitude jumps during a period 3 event, demonstrating the type of jumps that populate the three clusters in E-G.

6.3.3 Effect of haltere ablation on the chosen kinematic pattern

Shift in the recurrence period of the characteristic stroke deformations

Figure 6.13A shows one example each of the three types of sub-harmonic variations in ventral amplitude. During these special kinematic patterns the ventral amplitude changes

abruptly over a single stroke (as discussed and shown in section 6.3.2), and this change recurs periodically for dozens of wing beats. Figure 6.13B shows the frequency of occurrence of the 2 cycle periodic events in the measured test flights of the untreated (blue bar) and the haltere ablated flies (red bar). It is seen that the 2 cycle periodic variations are much more frequent in flies with intact halters as compared to those with both their halteres ablated; whereas the 3 cycle periodic variations (also 4 cycle ones, result not shown) are more frequent in haltere ablated flies. The ordinate scales of the supper panels in Fig.6.13B, C also indicate that the incidences of such sub-harmonic periodic variations decrease considerably in the flies without halteres.

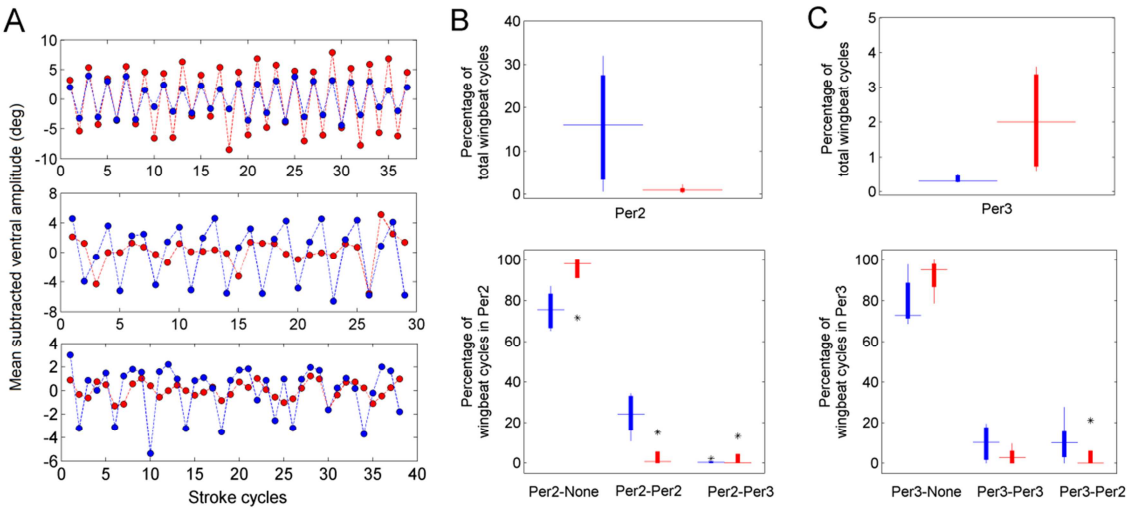

Figure 6.13: Sub-harmonic variations of ventral amplitude and the frequency of their occurrences in the two groups of flies. A) Intervals of mean subtracted ventral amplitude time series of the left (blue circles) and the right (red circles) wing, featuring one event from each type of the sub-harmonic variations. Top panel: 2 cycle periodic variations, middle panel: 3 cycle periodic variations and bottom panel: 4 cycle periodic variations. **B)** Upper panel: Percentage of the total number of stroke cycles (from all measured flies) showing 2 cycle periodic variations. Lower panel: Percentage of 2 cycle periodic variations that occur, a) only in one wing, b) simultaneously in both the wings and c) simultaneously with a three cycle periodic variation in the other wing. The plots show the quartile range of values (blue boxes: untreated flies; red boxes: haltere ablated flies), the full range of values (vertical thin lines) and the median values (horizontal thin lines) for the two groups of flies. **C)** Similar plots as B, for 3 cycle periodic variations

Figure 6.13 provides the overview (from all the measured flies) of the fraction of wingbeats showing sub-harmonic variations and the correspondence between the two wings. Looking at the bilateral coordination between the two wings during these fast sub-harmonic variations it is seen that most of these events occur dominantly in one wing (Fig.6.13D, E).

This one sided occurrences of the sub-harmonic variations become even more pronounced in haltere ablated flies.

Weak coupling between ventral amplitude and ventral-to-ventral stroke durations

Another feature of the wing kinematics that is distinctly affected by the haltere ablation is the short time scale variations of the stroke duration between two consecutive ventral reversals. As discussed in section 6.2 of this chapter and reported in (Chakraborty et al. 2015), the fruit fly can modify the ratio of the upstroke and the downstroke duration independently from the overall stroke duration. This would allow the fly to independently change the duration between two consecutive dorsal reversals and two consecutive ventral reversals. It is particularly important to take into account this difference between the two durations for variations occurring at time scales of a couple of stroke cycles. So, I estimated the dorsal-to-dorsal and the ventral-to-ventral stroke durations separately for the stroke cycles in the subharmonic events. These parameters are defined in the glossary at the end of the thesis and demonstrated pictorially in figure 6.15A. Figure 6.14 shows the scatter plots of these two stroke durations against the ventral amplitude for the stroke cycles with 2 cycle variations for the untreated flies and the 3 cycle periodic variations for the haltere ablated flies. These specific types of events were selected for presentation as they provide the best statistics for the two groups of flies. However, similar results were obtained from the other types of subharmonic events in both the groups.

The dorsal-to-dorsal stroke duration, which is the commonly used estimation of stroke duration, is seen to have a high correlation with the ventral amplitude during these subharmonic events from both the group of flies. For the untreated flies the R2 value is 0.47 and the slope is 0.4, while that for the haltere ablated flies the numbers are 0.55 and 0.52 respectively. For both the groups the stroke cycles with higher than average ventral amplitudes more often have higher than average stroke duration, as can be seen in the examples shown in figure 6.4. Such a correlation between the two stroke parameters implies that in the stroke cycles with larger than average ventral amplitudes the wing velocity is not increased.

For the untreated flies although the dorsal-to-dorsal stroke durations change in correlation with the ventral amplitudes, the ventral-to-ventral stroke durations remain essentially

constant (Fig.6.14A, B). This difference is prominent also in the data from only a single fly negating the possibility that the apparent lack of correlation is due to the pooling of data from 5 different flies. However, in case of the haltere ablated flies both the dorsal-to-dorsal and the ventral-to-ventral stroke durations are seen to have high correlation with the ventral amplitudes, albeit the changes in the later are much smaller. This indicates that the halteres play a key role in stabilizing the time course of subsequent ventral reversals in the face of changing ventral amplitudes of the stroke cycles.

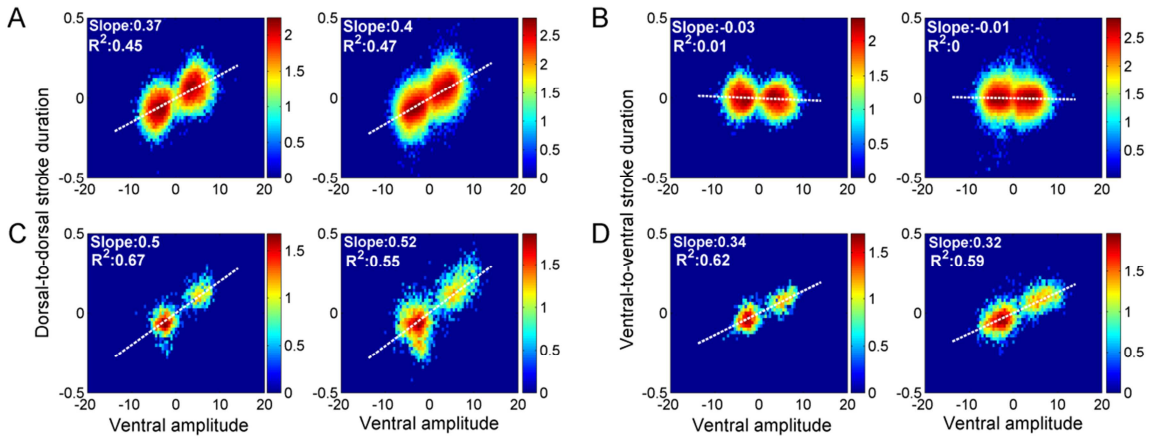

Figure 6.14: Correlation of the ventral amplitude and the stroke durations. A) Scatter plot of dorsal-to-dorsal stroke duration vs. ventral amplitude for the 2 cycle periodic events. Data from the untreated fly 2 is shown in left panel and that from all the 5 untreated flies is shown in the right panel. The numbers of points in each bin of size 0.5deg x 0.02ms is color coded in log scale of base 10 for better visualization of the density. **B)** Similar scatter plots as in A for the ventral-to-ventral stroke duration. 3 cycle periodic events from the haltere ablated fly 7 (left panel) and those from all the 5 haltere ablated flies (right panel). **C)** Stroke duration as estimated from one ventral reversal to the next for the 2 cycle periodic events from the untreated fly 2 (left panel) and those from all the 5 untreated flies (right panel). **D)** Similar scatter plots as in C for the 3 cycle periodic events from the haltere ablated fly 7 (left panel) and those from all the 5 haltere ablated flies (right panel).

To have some understanding of the underlying phenomenon by which the untreated flies maintain such constant ventral-to-ventral stroke duration while the haltere ablated flies cannot, I looked into the variations of the half stroke durations. I chose to work with the 2 cycle periodic events for both the untreated and the haltere ablated flies, as these events are the simplest of the three patterns. Figure 6.15 shows the scatter plots of the VA of a stroke cycle against its upstroke duration (US) and against the downstroke duration (DS) of the next stroke cycle. For the untreated flies, in a stroke cycle where the VA increases the upstroke duration also increases, but the downstroke duration in the next cycle decreases by almost the same amount. Hence, the overall interval between two consecutive ventral

stroke reversals is conserved. The upstroke durations and downstroke durations estimated for the 2 cycle periodic events from the 5 untreated flies have an average correlation value of 0.55 (range:). Such a balance is not maintained in case of the 2 cycle periodic events from the 5 haltere ablated flies. As seen in Fig.6.15 D, E the downstroke duration is more strongly coupled to the changes in the ventral amplitude, whereas the upstroke duration is uncorrelated to the ventral amplitude. As a result after a stroke cycle with higher than average ventral amplitude, not only is the next ventral amplitude smaller than average but it also comes sooner. The cartoon shown in figure 6.15A illustrates stroke cycles with exaggerated variations in a 2 cycle periodic event, as in untreated flies.

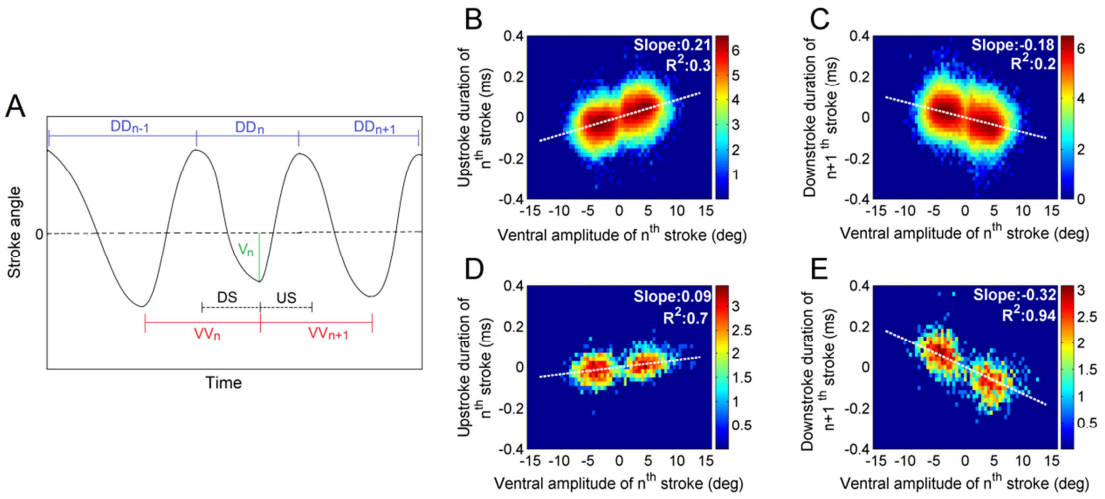

Figure 6.15: Correlation of the ventral amplitude and the half stroke durations. (A) Cartoon diagram of 3 stroke trajectories (bold black line) to illustrate the various stroke parameters, DD_n: duration between the dorsal reversals of the n^{th} and the $(n+1)^{th}$ stroke. VV_n: duration between the ventral reversals of the $(n-1)^{th}$ and the n^{th} stroke. DS_n: Down stroke duration of the n^{th} stroke. US_n: Up stroke duration of the n^{th} stroke. V_n: Ventral amplitude of the n^{th} stroke. Horizontal dashed line shows the reference line for measuring the stroke angles. **(B)** Scatter plot of upstroke duration vs. the ventral amplitude of the same stroke for untreated flies. For better visualization of the density of points, the numbers of points in each bin of 0.5 deg x 0.02 s is color coded in log10 scale. **C)** Scatter plot of downstroke duration vs. the ventral amplitude of the previous stroke for untreated flies. **(D-E)** Corresponding figures (as B and C respectively) for the haltere ablated flies.

6.4 Discussion

6.4.1 Least-dependent component analysis as a tool for identifying independently controlled kinematic patterns

The goal of this study was to identify kinematic patterns of the wing motion that are controlled independently of each other. Physiologically, these independent kinematic patterns can arise, for instance, from the activity of parallel anatomical pathways. The complete set of such elementary kinematic patterns can be viewed as a basis from which the fly composes its various maneuvers. Our method was designed to identify elementary patterns that are repeatedly activated in the available kinematic dataset, but cannot judge the completeness of the obtained set of patterns.

Independent control of some aerodynamic and kinematic parameters has already been proposed in previous insect flight studies (David 1985; Zanker 1988; Balint and Dickinson 2004); for a review refer to (Taylor 2001). Typically, the independence was assessed by estimating the correlation of these parameters during a flight recording. For example, in the study of Balint and Dickinson for blowflies (Balint and Dickinson 2004), the downstroke deviation was shown to have no significant correlation with either the dorsal amplitude of the same wing or the wingbeat period. Uncorrelatedness is a necessary, but not sufficient condition for statistical independence; non-linear statistical dependencies can persist even if the correlation coefficient is zero. Examining a scatter plot of two variables (as in (Balint and Dickinson 2004)) can help in excluding such non-linear dependencies. For an automatized computational approach, however, a quantitative evaluation is necessary. In our study, we assessed statistical independence using mutual information. This measure captures both linear and non-linear statistical dependencies: two variables are statistically independent if and only if their mutual information is zero. In contrast to previous studies, we attempted to systematically identify all independently controlled kinematic patterns

that occurred in the measured flies. Rather than examining a pre-determined set of kinematic features, we started off from the full wing stroke trajectory and used least-dependent component analysis (LCA) to compute a set of kinematic patterns that have minimal mutual information. Each kinematic pattern was associated with a specific deformation mode of the wing stroke. While for some patterns this deformation can be expressed in terms of a single standard kinematic parameter (such as stroke amplitude), for others the stroke deformation was more complex, involving e.g. example a change in both stroke amplitude and downstroke-to-upstroke ratio. In blowflies, Balint and Dickinson (Balint and Dickinson 2004) identified the downstroke deviation and the dorsal amplitude as two mutually independently controlled kinematic features, and pointed out that a change in either of these features was closely coupled with changes in other aspects of the wing stroke. Our method directly searches for independently activated deformations of the entire wing stroke. Another significant difference compared to (Balint and Dickinson 2004) is that our analysis takes into account the motion of both wings, and the degree of bilateral (anti)-symmetry is a defining feature of the kinematic patterns we identify.

Our computational method is based on least-dependent component analysis with explicit evaluation of mutual information. To successfully apply this advanced statistical tool, a sufficiently large sample size is necessary, typically thousands of wingbeat cycles. Long-duration flight recording increases the probability of the fly exerting multiple types of kinematic patterns during the recording, as well as the probability of repeated occurrence of activation events in each kinematic pattern. The former is crucial for identification of patterns that occur mutually independently and the latter enhances the reliability of their separation. Fig.6.16 shows the result of applying LCA to a flight segment of insufficient length (500 cycles). This leads to a failure in separating some of the kinematic patterns that were successfully separated when the analysis was applied instead to a 2500 cycle segment. It is likewise important for the analysis to start from a sufficient number of input signals to LCA. Each signal corresponds to a specific phase point in the wing stroke cycle; a higher number of phase points capture the stroke deformations more precisely. We used 16 phase points (8 for each wing), as we found that working with more points did not yield additional deformation modes with structured time course of activation (but considerably increased the computation time).

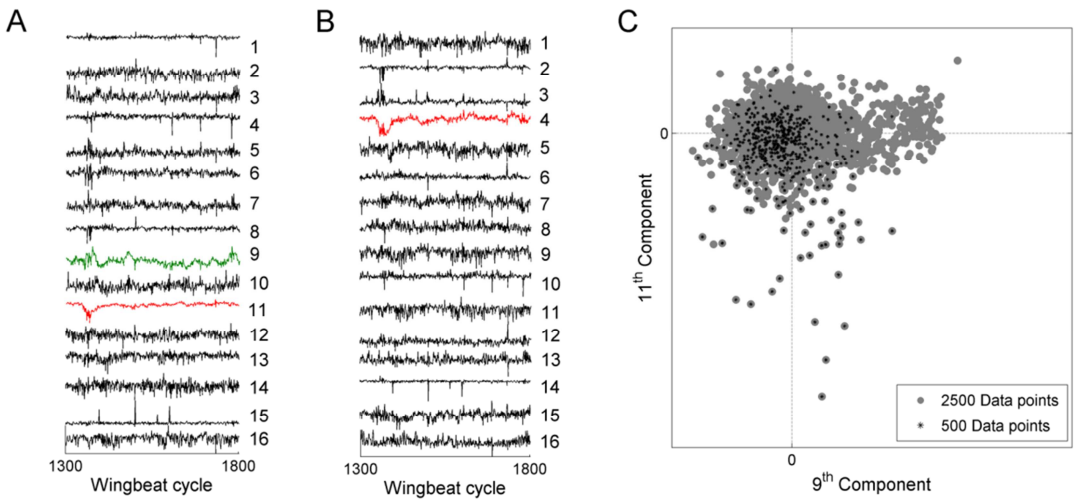

Fig 6.16: Data length and success of LCA analysis. A) Least-dependent components obtained by analyzing a flight segment of 2500 wingbeat cycles (input signals as in Fig.6.1A). A segment of 500 wingbeat cycles is shown (cycles 1300 to 1800 in Fig.6.1B). Component 9 and component 11 correspond to kinematic patterns of Type II and I, respectively. B) Least-dependent components obtained by analyzing the input signals from only this restricted segment of 500 WBCs. LCA failed to separate the type II kinematic pattern from other kinematic variations (there is no analogue of component 9 in A). Component 4 isolates the type I kinematic pattern, but not as cleanly as the analogous component 11 in A. C) Scatter plot of component 9 vs. component 11 in the full flight segment (2500 WBCs). The points belonging to the restricted segment (cycles 1300 to 1800) are highlighted in black. It is seen that the short segment does not sufficiently capture the full distribution of the data (the full distribution is more elongated in the x-direction).

Our computational analysis assumed that the elementary kinematic patterns (i.e., the stroke deformations generated by independent neuromotor controls) superpose linearly. This assumption is expected to be satisfied only approximately. On one hand, as the direct steering muscles all attach to the wing hinge, a linear summation of their effects on the wing stroke may be expected. On the other hand, the muscles insert at different sclerites that can to some extent move with respect to each other; this likely leads to nonlinear summation in blowflies ((Balint and Dickinson 2001) and references there in). A linear superposition of the effects of indirect muscles and direct steering muscles was inferred for Drosophila in (Frye and Dickinson 2004). The elementary kinematic patterns identified in our analysis adequately represented the wing kinematics both when active one-by-one and when active simultaneously (Fig.6.3). This provides a consistency check for the assumption of linear superposition (which was used in identifying the elementary kinematic patterns). A direct test of this assumption would be possible in a stimulated-flight setup, using stimuli that activate the individual kinematic patterns.

6.4.2 Classification of the least-dependent kinematic patterns and implications for flight control

In most of the flight segments analyzed, LCA decomposed the wing motion into a set of linear components with insignificant or only marginally significant mutual dependence. Each such component is associated with a specific deformation mode of the wing stroke (terminology defined at the end of the thesis). The deformation mode together with the time course of its activation specifies a kinematic pattern of the wing motion. The kinematic patterns defined by components that are statistically independent could, in principle, result from independent neuromotor controls.

Alternatively, some of the obtained statistically independent kinematic patterns may reflect other sources, such as noise in neuromuscular activity, experimental artifacts, or variability unrelated to flight control. To narrow down the set of candidates for elementary kinematic patterns (i.e., patterns that are generated by independent neuromotor flight controls), I restricted further analysis to components that (i) had temporal structure significantly distinct from white noise, and (ii) occurred repeatedly in multiple flight segments and in different flies. The first criterion was motivated by our expectation that the activation course of the elementary patterns will contain time scales similar to those seen in various flight maneuvers (i.e., between several wing stroke cycles and hundreds of cycles). Components with a flat power spectrum, on the other hand, are more likely to result from physiological noise or from measurement artifacts. The second criterion required the pattern coded by the component to occur in at least 3 of the 10 analyzed flies. We cannot exclude that some of the infrequently obtained independent components do represent elementary patterns. The rarely obtained components can, however, also arise e.g. from transient nonlinear couplings between elementary patterns, or from statistical limitations (limited duration of the recorded flight segment). In our search for the elementary kinematic patterns, I therefore chose not to classify the rarely occurring components. The described elimination may be viewed as a dimensional reduction; its goal, however, was to construct a lower-dimensional space that still contains the frequently activated independent kinematic patterns, rather than best approximating the time course of the original signal.

The resulting classification of kinematic patterns is summarized in Fig.6.9. I identified 7 types of frequently recurring patterns. For five of these types, the kinematic pattern was found in at least 6 of the 10 examined flies. As our analysis was based on recordings of unstimulated flight of limited duration, I do not view as surprising that some kinematic patterns were not observed in all flies. To help in deciding which of the 7 frequently recurring types of patterns should be viewed as elementary kinematic patterns, I evaluated their possible functional roles.

To functionally interpret a given kinematic pattern, we first examined the stroke deformation mode associated with it. Previous studies (Sane and Dickinson 2001; Fry et al. 2005) used dynamically scaled robotic models to establish the correspondence between changes in wing stroke kinematics and changes in aerodynamic forces. The full 3-dimensional kinematics of each wing is specified by the time course of three angles: the stroke position, the morphological angle of attack, and the deviation. In this study, only the stroke position was measured. I therefore could not directly evaluate the aerodynamic forces and their moments, as was done in (Sane and Dickinson 2001; Balint and Dickinson 2004). However, previous studies with optically stimulated tethered fruit flies (Gotz 1983) established a linear relation between the difference of stroke amplitudes in the two wings and the yaw torque generated by the fly; likewise, the difference of stroke amplitudes is correlated with yaw torque during a free flight saccade (Fry et al. 2003). We therefore concluded that the wing stroke deformation typical for type I kinematic patterns (i.e., a bilaterally antisymmetric change in stroke amplitude and no change in wing period) is associated primarily with a change in yaw torque. For the type II kinematic patterns, the stroke deformation mode involves a bilaterally symmetric change in stroke amplitude coupled with a change in wingbeat period. A similar stroke deformation can be evoked by optical stimulation (vertical movement of the background pattern) and results in a change of total flight power (Lehmann and Dickinson 1998). For the type III kinematic pattern, the stroke deformation involves a change in the ratio of downstroke duration to upstroke duration. When symmetric in both wings, this change in stroke trajectory is expected to alter primarily the pitch torque acting on the body. In Ref. (Fry et al. 2005), the aerodynamic output was evaluated for wing strokes recorded in hovering free flight and in tethered flight; these wing strokes differed primarily by the downstroke-to-upstroke ratio (1.16 in

free flight vs.1.53 in tethered flight). It was shown that in the tethered case, the wing stroke generates a strong pitch torque (that would cause an untethered fly to pitch nosedown by 20° after a single stroke cycle) (Fry et al. 2005). In our flight tests, the downstroke-to-upstroke ratio was in the range 1.45–1.55 for the baseline wing stroke, but decreased to values as low as 1.1 when a type III kinematic pattern was activated. We therefore associate the type III kinematic patterns with a strong change in pitch torque.

The inferences given above were based on the similarity of stroke position trajectory in the stroke deformations identified by us and in the kinematic changes analyzed in previous literature. We cannot exclude that there are differences in the morphological angle of attack or in stroke deviation that would modify the torques or forces acting on the body. In Ref. (Balint and Dickinson 2004) kinematic changes in the three rotational degrees of freedom were found to be mutually strongly coupled, resulting in concerted modifications of the entire wing stroke. It is, however, possible that the deformation of the stroke position trajectory (even when sampled at a high rate) is not fully indicative of the full 3-dimensional wing kinematics.

To further judge the functional relevance of the kinematic pattern of a specific type, we next compared the typical features in its activation time course to the typical time courses of known flight maneuvers. For the type I kinematic pattern, the time course of the activation events matches the time course reported for fictive saccades induced by visual expansion stimulus in tethered flight (Heisenberg and Wolf 1979; Tammero and Dickinson 2002). The type I kinematic pattern can therefore be identified with activations of the saccade motor program (see (Bender and Dickinson 2006) for a discussion of the relation between tethered and free flight saccades).The activation events for the kinematic patterns of type II and III are typically of longer duration, consistent with the time scales on which Drosophila is known to control flight power and pitch.

In type VI kinematic patterns, the ventral amplitude for both wings in turn increases and decreases in successive wing strokes; such regular switching persists for dozens of cycles. It is plausible that this kinematic pattern is caused by some steering muscle(s) becoming active in every other wingbeat cycle. Due to the novelty and the unique temporal characteristics of this kinematic pattern I studied it in details (see section 6.3). It appears

unlikely that this pattern has a direct functional role in flight control, yet the pattern occurred frequently and was observed in the majority of the examined flies.

Kinematic patterns of types IV and V involve a bilaterally antisymmetric change in the dorsal reversal positions (type IV) or in the stroke angles at the mid-upstroke phase of the stroke cycle (type V). The activation time courses in these kinematic patterns do not have prominent temporal features, and we have not been able to relate these patterns to any known flight maneuver. It is possible that these two types of kinematic pattern simply reflect particular sources of noise in neuromuscular activity. In this case, the fly would control the bilaterally symmetric variations in dorsal amplitudes (which are prominent in type II kinematic patterns), but not the antisymmetric variations (which are usually of lower magnitude). In blowflies (Balint and Dickinson 2004), dorsal amplitude was found to vary independently of downstroke deviation. Because the 3D kinematics of an individual wing was studied in (Balint and Dickinson 2004), a direct comparison to our findings on stroke deformations evaluated jointly for both wings is difficult.

The type VII kinematic pattern, which was obtained as a separate component in 8 flight segments, is characterized by a slow periodic modulation of the wing stroke (with a period of 40–50 wingbeat cycles). In other flight segments, however, such periodic modulation was not isolated by LCA into a separate component, but rather remained mixed with other kinematic patterns (predominantly of type I). This indicates that the type VII kinematic pattern may be nonlinearly coupled with other pattern types. Consequently this kinematic pattern was not included among the elementary kinematic patterns that form a linear basis for the construction of the total wing stroke. The type VII kinematic pattern may be related to the yaw torque fluctuations with similar periodicity that were reported by Heisenberg and Wolf (Heisenberg and Wolf 1988).

Based on the properties described above, it was proposed that the kinematic patterns of types I, II, III and VI are elementary kinematic patterns. I view these 4 elementary patterns as part of the basis, from which the total deviation of the wing kinematics from the baseline stroke is composed by linear superposition. For each of these 4 kinematic patterns, the corresponding stroke deformation modes are typically activated intermittently, with well-delineated activation events separated by intervals of relative inactivity. The activation

events of the 4 elementary patterns occurred both one-at-a-time (demonstrating that the 4 corresponding neuromotor controls are not coupled by strong mutual excitation) as well as simultaneously (demonstrating that they are not coupled by strong mutual inhibition).

One cannot exclude that there are additional elementary kinematic patterns, which were not activated frequently during our measurements, or which are not activated at all during tethered, unstimulated flight. It is also possible that some of the elementary kinematic patterns that I identified result from the simultaneous activation of several neuromotor controls that may act mutually independently in other behavioral settings. Our finding of 4 elementary kinematic patterns therefore gives only a lower bound for the number of independent neuromotor controls.

Our results have a partial correspondence to the control system implemented in the simulations of Dickson et al. (Dickson et al. 2008). In their integrative model of Drosophila flight, the navigation through a virtual environment was achieved by the appropriate activation of four "deformation modes": the pitch mode, the yaw mode, the roll mode, and the throttle mode. Each mode consists of a suitable deformation of the wing stroke that achieves the required change in flight torque or force. The activation of each of these modes is achieved by a separate controller. The yaw mode and the throttle mode defined in Ref. (Dickson et al. 2008) are in direct correspondence to the kinematic patterns of type I and II I found in my study. The pitch mode in Ref. (Dickson et al. 2008) is functionally similar to the kinematic pattern of type III, but consists of a different deformation of the wing stroke. The deformation modes in Ref. (Dickson et al. 2008) were designed a priori, based on previous conceptions of Drosophila flight control. In contrast, in this study the independently controlled deformation modes of type I, II and III were extracted from an automatized computational analysis of unstimulated flight recordings. The results of this study thus provide support to the control framework of Dickson et al.

6.4.3 Physiological explanation for the periodic single cycle ventral amplitude jumps

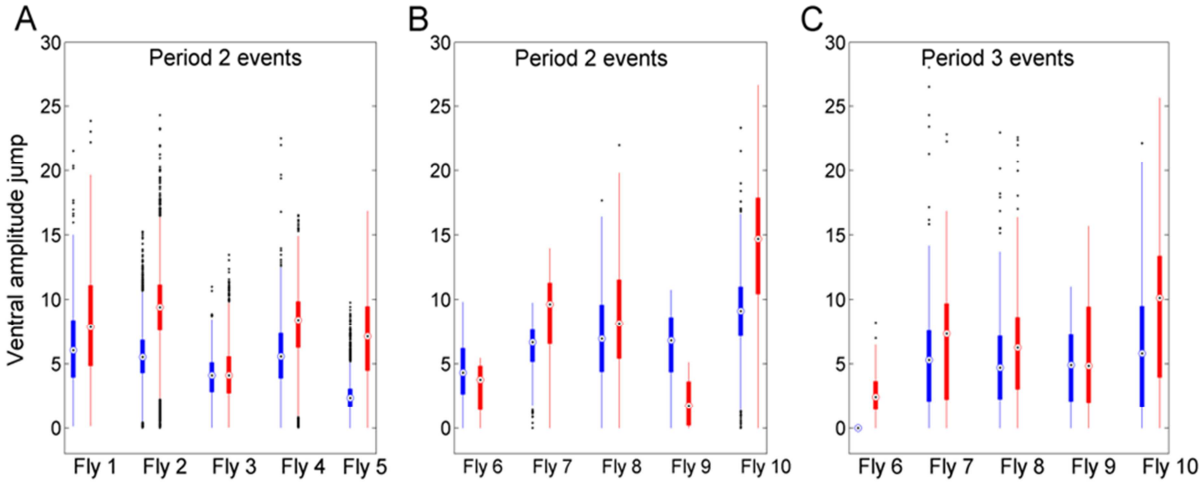

Figure 6.16: Box plots of magnitudes of the ventral amplitude jumps during databased events of subharmonic variations. A) Period 2 events from untreated flies (blue: left wing; red: right wing). Filled boxes mark the quartile range of the VA jump magnitudes and the vertical lines show the full range. Black dot in the hollow circle mark the median value. Outliers are shown in black dots. Serial number of the corresponding fly is mentioned along the x-axis. **B-C)** Period 2 **(B)** and period 3 **(C)** events from haltere ablated flies. Other specifications are same as that for A.

A strikingly robust feature of the subharmonic stroke variations is the narrow range of VA jump magnitudes in each wing. Figure 6.16 shows the box plots of these jumps during the 2 cycle periodic events from each untreated fly (Fig.6.16A) and 2, 3 cycle periodic events from each haltere ablated fly (Fig.6.16B, C). In all 5 untreated flies the interquartile range is less than 5 degrees; except in case of the right wing of fly 1, where the range spans 6.3 degrees. This spread in the magnitude of the jumps is pretty small considering that in each case the count of jumps is in thousands and is distributed over a recording period of 60 secs. For example, the interquartile range of 11835 jumps from the left wing and 23805 jumps from the right wing of fly 4 are 3.5 degrees and 3.6 degrees respectively. The interquartile range of the VA jumps from the haltere ablated flies are also less than 6 degrees, except in the case of fly 10, right wing, where the range is 7 degrees. However, in this group of flies the number of stroke cycles in such events count only in hundreds (data not shown), and hence the statistics is weaker. The interquartile ranges of the VA jumps in 2cycle periodic events from the untreated and the haltere ablated flies are statistically similar (KS test $p<0.01$). In case of the 3 cycle periodic events the range of jump magnitudes are expected to be higher,

as each recurring unit constitutes of two large jumps and an intermediate smaller jump (Fig.6.12). Even for these events the interquartile range for jump magnitudes (Fig.6.17C) are less than 8 degrees in all but one case (fly 10, right wing). Such sharply maintained VA jump magnitudes indicate that a single or a particular group of muscles is primarily responsible for causing these single stroke increases in VA.

One group of muscles whose activities have clearly been seen to be associated with sudden increase in wingbeat amplitude is the one inserting in the basalare sclerite (M.b1, M.b2, M.b3). For anatomical details of these muscles see section 1.4.3. In their study Heide and Gotz (Heide and Götz 1996) showed that, as the flies increase their stroke amplitudes while trying to stabilize a moving pattern on the screen (optomotor response), the second basalare muscle M.b2 shows bursts of activity; and the first basalare muscle M.b1 is activated at a slightly earlier phase during each stroke. In a more direct study Lehmann and Gotz (Lehmann and Götz 1996) showed that the increase of VA of the ipsilateral wing is the principal effect of M.b2 activation. They showed that an increase of 8-12 degrees in the VA can be achieved by stimulating M.b2 with an average of one electrical pulse (>1.2V) in every wingbeat cycle. Stimulating at a lower rate, i.e. once in every two cycle, results in a slightly smaller increase in VA; on the other hand stimulating with a long lasting pulse burst result in an average increase of 14 degrees in the VA of the ipsilateral wing (Lehmann and Götz 1996). These numbers match very closely with the range of jump magnitudes seen during the subharmonic variations across the studied group of flies. In addition, it was also shown that the electrical stimulation of M.b2 does not introduce any change in wingbeat frequency (or in stroke duration). They measured the stroke durations as the interval between two consecutive ventral to dorsal reversals. This again agrees with our finding of the constancy of the ventral-to-ventral stroke duration during the events. Together both these features of the subharmonic events strongly indicate a principal role of the M.b2 muscle in their generation, both in the untreated and the haltere ablated flies. The different median values of the VA jumps in different flies and sometimes even in two wings of the same fly may thus be due to differences in the extent or the relative phase of stimulation of M.b2. Another possible cause of this discrepancy may be the transient activity of other muscles that alter the mode of oscillation of the wing articulation, as discussed in (Walker et al. 2014) for Calliphora (blow fly).

However, it should be noted that the activity of the second basalare muscle has mostly been recorded during the optomotor response behavior (Heide and Götz, 1996; Balint and Dickinson, 2001) where the muscle is impinged with bursts of neuromuscular spikes. Under such activation regime the muscle elicits a rapid increase in VA almost within the next stroke cycle. This increased VA then persists for another few dozen wingbeats. It is often seen in the examples shown, and also explicitly reported in (Lehmann and Götz 1996) that after the last muscle activation pulse of a long enough activation period, it takes about a dozen or more wingbeats for the VA to come back to its pre-activation value. Hence, it is not clear what kind of muscle activation regime of M.b2 may lead to such single cycle increase in VA. Nevertheless, to confirm the role and mode of activation of M.b2 in the generation of these periodic VA jumps electrophysiological studies or better still, time-resolved microtomographic imaging of the thorax is needed (Walker et al. 2014).

6.4.4 Change in recurrence rate of the ventral amplitude jumps in absence of haltere feedback

Given the strong similarity of the stroke deviations in all these prototypical events from both the group of flies, it was concluded that they are not distinct kinematic patterns but the same kinematic pattern with the characteristic stroke deviation recurring after different intervals. The slight difference between the two traces in subplots K-L compared to I-J of figure 6.11 during the upstroke is because a large number of prototypical events coming from fly 5 have an associated decrease in dorsal amplitude in addition to the increase in ventral amplitude. However, this periodic change in the dorsal amplitude is not always present for all the events of even the same fly and hence cannot be considered to be a defining feature of the concerned kinematic pattern.

In this studied kinematic pattern it appears that in the presence of simultaneous wing and haltere feedback, the concerned muscle (or the synergy) is activated once in every 2 cycles; whereas if the haltere feedback is rendered weak, the same muscle synergy is activated after one or two extra cycles. The most plausible mechanism that can explain such a long and consistent increase in latency is the temporal summation of the excitatory postsynaptic potentials (EPSP). Wingbeat synchronous feedbacks to the steering muscles are known to come from two distinct sources, the mechanosensors on the wing blade and those at the base of the halteres (Fayyazuddin and Dickinson 1999; Mureli and Fox 2015; Bartussek and

Lehmann 2016). The temporal summation hypothesis would mean that the summed EPSP generated by the haltere and the wing is strong enough to activate the muscle synergy every other cycle. But the wing-driven EPSP alone would more often require the cumulative effect over at least two cycles to activate the post synaptic neuromuscular junction. Hence, the very regular 2 cycle periodic kinematic pattern in untreated flies disperses into 2, 3 and 4 cycle periodic events in haltere ablated flies. Such cases of sub-threshold EPSP summation to generate post synaptic action potentials have been shown to exist in the neck muscles of the blowfly *Calliphora vicina*. (Huston and Krapp 2009) showed that the neck motor neurons receive small, sustained sub-threshold EPSPs from the visual afferents which by themselves are incapable of activating the neck muscles. However, when combined with the afferent signals due to an out-of-plane haltere movement, result in an action potential in the neck motor neurons, and thus instigating a head turn.

A second possibility is that in absence of haltere feedback, the wing afferents stimulate the concerned steering muscles with increased temporal delays, hence resulting in prolonged recurrence period of the single cycle VA jumps. The EPSPs of both the haltere and the wing sensory nerves (as studied for the first basalar muscle in Fayyazuddin and Dickinson, 1999) constitute of a low latency sharp peak and a long latency broad peak. The low latency component comes from a monosynaptic electrical synapse, while the high latency component comes from a possibly polysynaptic Ca^{2+} dependent chemical synapse (Fayyazuddin and Dickinson 1996). In case of the haltere afferents the former peak dominates, resulting in a fast and temporally precise sensorimotor feedback; whereas in the case of the wing afferents the later peak dominates, resulting in a stronger but slow and temporally less precise feedback. The latencies of the Ca^{2+} dependent EPSP peaks (w.r.t mechanosensory stimulation) are highly variable, and can be as high as 8 ms in the fruit fly drosophila (as studied in genetically modified flies by Trimarchi and Murphey, 1997). Hence, although the wing mechanosensors can drive the wingbeat synchronous activation of the basalar muscles in the absence of halteres, the phase of activation is expected to be highly variable.

Conclusion

The findings of my PhD research regarding the neuromuscular control of rhythmic motor activities can broadly be summarized in two points:

i. Bilateral coherence in physiological and essential tremor expressed in the two hands is more common than has previously been reported. In both the cases the oscillations of the two hands are intermittently synchronized. It was proposed that in postural physiological tremor, bilateral coherence at the main tremor frequency arises from transient simultaneous entrainment of the left and right hand oscillations to ballistocardiac forcing; the hand acceleration data from essential tremor patients that I analyzed did not enable us to clarify the mechanisms for essential tremor, additional studies are needed in this front.

ii. Complicated wing movements during insect flight, such as that during a banked turn, can be generated from linear superposition of elementary kinematic patterns that are controlled mutually independently. This provides strong evidence for the presence of modular motor control of rhythmic motion in invertebrates.

Summary

My PhD research in broad sense is kinematic study of rhythmic motions arising in specific parts of the neuromuscular system. Rhythmic motor activities are particularly interesting as it is the ubiquitous mode of locomotion in the animal kingdom and has evolutionarily developed some of the fastest yet precise sensorimotor systems. At the same time, involuntary rhythmic motions of the limbs are the most prevalent form of motion disorder viz. tremors. Understanding the genesis and the underlying dynamics of these rhythmic motor patterns leads to a better understanding of the neural control mechanisms and also helps to develop methods for controlling the progression of related diseases.

I worked on two specific aspects of rhythmic motion control, i) bilateral coordination of spontaneous rhythmic motions, viz. tremors, and ii) modular control of locomotor patterns. For the former I studied the cases of the two most common types of hand tremors in human, the physiological tremor (PT) and the essential tremor (ET). The locomotor patterns are a more complicated form of rhythmic motion; owing to the necessities of providing the necessary drive, maneuverability, stability and adaptation to the environment. As a result, for ages studies on model organisms, which provide a simpler basis both for experimental and theoretical analyses, have aided in understanding the functionality of analogous structures and motivated studies in higher organisms. Insect flight provides a powerful model system for neuromotor control. Hence, for the second part of my study I analyzed wing kinematics of fruit flies, *Drosophila melanogaster.*

In the first part of my study I explored the prevalence and the temporal structure of bilateral coherence in PT and ET, in human subjects. Bilateral coherence of hand kinematics provides a sensitive measure of synchronizing influences on the left and right tremor oscillations, which in turn points towards a common mechanism of bilateral tremor genesis.

In addition, the understanding of bilateral tremor coherence in healthy subjects is important in the context of bilateral entrainment tests for differential diagnosis of tremor diseases. I analyzed triaxial accelerometric recordings from both hands in 30 healthy subjects and 34 ET patients using spectral coherence and wavelet coherence methods. The majority of both healthy and ET subjects displayed significant bilateral coherence. While in healthy subjects, bilateral coherence was most frequently found in resting hand position (97% of subjects); in ET the prevalence was comparable for resting (54%) and postural (49%-57%) positions. In both PT and ET, short epochs of several seconds with strong coherence were separated by intervals of insignificant coherence. To estimate the contribution of the mechanical forcing due to the cardioballistic impulse in the bilateral coherence, I measured the chest acceleration simultaneously with the hand acceleration in 12 additional healthy subjects. In PT, bilateral coherence at the main tremor frequency (8-12 Hz) was coupled with the ballistocardiac rhythm.

In the second part of my study I aimed to find elementary components of wing motion control in the fruit flies, *Drosophila melanogaster*, that could be thought of as the building blocks for more complicated wing movements. If present, this will provide a much simpler system (as compared to vertebrate systems) to study the working principles of modular motor control. Using a high-speed computer vision system, the wing motion of tethered flying fruit flies were recorded for up to 12000 consecutive wing strokes at a sampling rate of 6250 Hz. I then decomposed the joint motion pattern of both wings into components that had the minimal mutual information (a measure of statistical dependence). I classified such kinematic patterns, i.e. a specific deformation of the wing stroke and the sequence of its activation from cycle to cycle, obtained from recordings of 10 flies. Out of the 7 classified types of kinematic patterns, four showed strong evidence for being considered elementary kinematic patterns. They can be activated mutually independently, and occur both in isolation and in linear superposition. This indicates existence of modular motor control in flies and provides a lower bound for the number of independent neuromotor controls of wing motion. Three of the identified elementary patterns can be associated with yaw control during body saccades, pitch control, and control of flight power. A fourth kinematic pattern consists in the alteration of stroke amplitude with a period of 2 wingbeat cycles, extending for dozens of cycles.

Due to the novelty of the fourth elementary kinematic pattern I studied it in some details. This kinematic pattern involves a characteristic modification of the stroke trajectory lasting for only one stroke cycle, and recurring periodically; implying a control system that has effects at the time scale of a single stroke cycle. Neurophysiology of the fly sensorimotor system suggests a potential role of the mechanosensory feedback from the modified hind wings called the halteres, in the control mechanism of this special kinematic pattern. To check this plausibility I analyzed wing kinematics of tethered flying flies with both their halteres ablated. As expected, missing haltere signaling considerably modified this special kinematic pattern; of special mention is the development of a weak coupling between the cycle-to-cycle changes in ventral stroke amplitudes and the timings of the ventral reversal.

In conclusion my PhD research has put forth two major findings regarding the neuromuscular control of rhythmic motor activities: i. bilateral coherence in PT and ET expressed in the two hands is much more common than has previously been reported. In both the cases the oscillations of the two hands are intermittently synchronized. We propose that in postural PT, bilateral coherence at the main tremor frequency arises from transient simultaneous entrainment of the left and right hand oscillations to ballistocardiac forcing. ii. Overall wing kinematics during insect flight can be generated from linear superposition of elementary kinematic patterns that are controlled mutually independently. This provides strong evidence for the presence of modular motor control of rhythmic motion in invertebrates.

List of publications

Full length papers in peer reviewed journals

- Chakraborty, S., Kalisova, J., Sprdlik, O., Hoskovcova, M., Ulmanova, O., Ruzicka ,E., Zapotocky, M. (2017) Intermittent bilateral coherence in physiological and essential hand tremor. (Accepted for publication in Clinical Neurophysiology) (IF: 3.426)

- Chakraborty, S., Bartussek, J., Fry, S. N. and Zapotocky, M. (2015). Independently Controlled Wing Stroke Patterns in the Fruit Fly Drosophila melanogaster. PLoS ONE 10, e0116813. (IF: 3.057)

Published Matlab codes and data

- Chakraborty, S., Bartussek, J., Fry, S. N. and Zapotocky, M. (2015). Wing stroke kinematics and its independent components in Drosophila melanogaster. Figshare. https://dx.doi.org/10.6084/m9.figshare.1244993.v1

Published peer reviewed abstracts (In journals with impact factor)

- Chakraborty, S., Bartussek, J., Fry, S. N., Zapotocky, M. (2011) Independent component analysis of flight maneuvers in Drosophila melanogaster. Proceedings of Computational Neuroscience and Neurotechnology Bernstein conference and Neurex Annual Meeting, Freiburg 2013, Front. Comput. Neurosci. (IF: 2.147)

- Chakraborty, S., Bartussek, J., Fry, S. N., Zapotocky, M. (2013) Independent components of wing kinematics in the fruit y Drosophila. Proceedings of Twenty Second Annual Computational Neuroscience Meeting: CNS 2013, Paris 2013. BMC Neuroscience 2013, 14(Suppl 1):P429 (IF: 2.845)

Full length paper in preparation for peer reviewed journal

- Chakraborty, S., Bartussek, J., Fry, S. N. and Zapotocky, M. Periodic wing stroke patterns regulated by fast mechanosensory feedback in Drosophila. (Expected: 2017)

List of abbreviations

ET: Essential tremor

MILCA: Mutual information based least-dependent component analysis

LDC: Least-dependent component

PT: Physiological tremor

VA: Ventral amplitude

Glossary of selected terms used in chapter 6

baseline wing stroke: Set of 16 stroke positions obtained by averaging each of the 16 input signals over the 2500 wingbeat cycles in a given flight segment.

dorsal amplitude: maximum stroke position closer to the head, at the point where the wing reverses its course.

elementary kinematic pattern: Least-dependent kinematic pattern that is claimed to be controlled independently.

input signal: Stroke position at a specific phase of the wingbeat cycle, over 2500 cycles (see Fig.3.3). 16 such signals (8 from each wing) constitute the full set of input signals to LCA.

kinematic pattern: a specific deformation of the wing stroke and the sequence of its activation from cycle to cycle.

least-dependent component analysis: Linear transformation of a set of signals into another set of signals that have minimum mutual dependence.

least-dependent component: A specific linear combination of the input signals, obtained from LCA. It defines the time course of activation of a particular "stroke deformation mode".

least-dependent kinematic pattern: Stroke deformation mode and its time course of activation. (Refers jointly to a specific LDC and its separating vector)

reconstructed wing stroke: Array of phase points computed by back-transforming a subset of least-dependent components. Used for visualization of "stroke deformation modes".

stroke angle: It is defined as the angle between the stroke plane and the

stroke deformation mode: Specific form of deviation of the wing stroke from the baseline wing stroke. Defined by the separating vector of a specific LDC.

stroke position: Angular position of the fly wing on the stroke plane with respect to the lateral axis of the fly body.

stroke trajectory: Time course of stroke positions of the wing, as recorded with our apparatus.

ventral amplitude: maximum stroke position closer to the abdomen, at the point where the wing reverses its course.

Bibliography

Abbott RH, Cage PE. A possible mechanism of length activation in insect fibrillar flight muscle. J Muscle Res Cell Motil. 1984 Aug;5(4):387–97.

Addison PS. The Illustrated Wavelet Transform Handbook: Introductory Theory and Applications in Science, Engineering, Medicine and Finance. CRC Press; 2002.

Albo Z, Di Prisco GV, Chen Y, Rangarajan G, Truccolo W, Feng J, et al. Is partial coherence a viable technique for identifying generators of neural oscillations? Biol Cybern. 2004 May;90(5):318–26.

Arbib MA, editor. The handbook of brain theory and neural networks. 2. ed. Cambridge, Mass.: MIT Press; 2003. (A Bradford book).

Arce-McShane FI, Ross CF, Takahashi K, Sessle BJ, Hatsopoulos NG. Primary motor and sensory cortical areas communicate via spatiotemporally coordinated networks at multiple frequencies. Proc Natl Acad Sci. 2016 May 3;113(18):5083–8.

d'Avella A, Bizzi E. Shared and specific muscle synergies in natural motor behaviors. Proc Natl Acad Sci. 2005 Feb 22;102(8):3076–81.

Baker SN, Kilner JM, Pinches EM, Lemon RN. The role of synchrony and oscillations in the motor output. Exp Brain Res. 1999 Sep;128(1–2):109–17.

Balint CN, Dickinson MH. The correlation between wing kinematics and steering muscle activity in the blowfly Calliphora vicina. J Exp Biol. 2001 Dec;204(Pt 24):4213–26.

Balint CN, Dickinson MH. Neuromuscular control of aerodynamic forces and moments in the blowfly, Calliphora vicina. J Exp Biol. 2004 Oct;207(Pt 22):3813–38.

Bartussek J, Lehmann F-O. Proprioceptive feedback determines visuomotor gain in Drosophila. R Soc Open Sci. 2016 Jan;3(1):150562.

Bartussek J, Mutlu AK, Zapotocky M, Fry SN. Limit-cycle-based control of the myogenic wingbeat rhythm in the fruit fly Drosophila. J R Soc Interface. 2013 Mar 6;10(80):20121013.

Bell AJ, Sejnowski TJ. An information-maximization approach to blind separation and blind deconvolution. Neural Comput. 1995 Nov;7(6):1129–59.

Bendat JS, Piersol AG. Random Data: Analysis and Measurement Procedures. 2nd edition. Hoboken, N.J: Wiley; 1986.

Bender JA, Dickinson MH. Visual stimulation of saccades in magnetically tethered Drosophila. J Exp Biol. 2006 Aug 15;209(16):3170–82.

Berger W, Dietz V, Quintern J. Corrective reactions to stumbling in man: neuronal co-ordination of bilateral leg muscle activity during gait. J Physiol. 1984 Dec;357:109–25.

Bergou AJ, Ristroph L, Guckenheimer J, Cohen I, Wang ZJ. Fruit flies modulate passive wing pitching to generate in-flight turns. Phys Rev Lett. 2010 Apr 5;104(14):148101.

Boonstra TW, Daffertshofer A, van Ditshuizen JC, van den Heuvel MRC, Hofman C, Willigenburg NW, et al. Fatigue-related changes in motor-unit synchronization of quadriceps muscles within and across legs. J Electromyogr Kinesiol. 2008 Oct;18(5):717–31.

Bour LJ, Aramideh M, de Visser BW. Neurophysiological aspects of eye and eyelid movements during blinking in humans. J Neurophysiol. 2000 Jan;83(1):166–76.

Brillinger DR. Time Series: Data Analysis and Theory. Philadelphia: SIAM: Society for Industrial and Applied Mathematics; 2001.

Brockwell PJ, Davis RA. Time Series: Time Series: Theory and Methods. 2nd ed. 1991. 2nd printing 2009. Softcover reprint of the original 2nd ed. 1991. Springer; 1991.

Brown TG. The Intrinsic Factors in the Act of Progression in the Mammal. Proc R Soc Lond B Biol Sci. 1911 Dec 8;84(572):308–19.

Card G, Dickinson MH. Visually mediated motor planning in the escape response of Drosophila. Curr Biol CB. 2008 Sep 9;18(17):1300–7.

Cathers I, O'Dwyer N, Neilson P. Entrainment to extinction of physiological tremor by spindle afferent input. Exp Brain Res. 2005 Nov 24;171(2):194–203.

Cazalets JR, Sqalli-Houssaini Y, Clarac F. Activation of the central pattern generators for locomotion by serotonin and excitatory amino acids in neonatal rat. J Physiol. 1992 Sep;455:187–204.

Chakraborty S, Bartussek J, Fry SN, Zapotocky M. Independently Controlled Wing Stroke Patterns in the Fruit Fly Drosophila melanogaster. PLoS ONE. 2015 Feb 24;10(2):e0116813.

Cham R, Redfern MS. Changes in gait when anticipating slippery floors. Gait Posture. 2002 Apr;15(2):159–71.

Chan WP, Dickinson MH. Position-specific central projections of mechanosensory neurons on the haltere of the blow fly, Calliphora vicina. J Comp Neurol. 1996 Jun 3;369(3):405–18.

Chang S, Wang ZJ. Predicting fruit fly's sensing rate with insect flight simulations. Proc Natl Acad Sci. 2014 Aug 5;111(31):11246–51.

Cheng B, Deng X. Translational and Rotational Damping of Flapping Flight and Its Dynamics and Stability at Hovering. IEEE Trans Robot. 2011 Oct;27(5):849–64.

Cohen O, Pullman S, Jurewicz E, Watner D, Louis ED. Rest tremor in patients with essential tremor: prevalence, clinical correlates, and electrophysiologic characteristics. Arch Neurol. 2003 Mar;60(3):405–10.

Corden DM, Lippold OC, Buchanan K, Norrington C. Long-latency component of the stretch reflex in human muscle is not mediated by intramuscular stretch receptors. J Neurophysiol. 2000 Jul;84(1):184–8.

Craven P, Wahba G. Smoothing noisy data with spline functions. Numer Math. 1978 Dec 1;31(4):377–403.

Darton K, Lippold OC, Shahani M, Shahani U. Long-latency spinal reflexes in humans. J Neurophysiol. 1985 Jun;53(6):1604–18.

Daubechies I. Ten Lectures on Wavelets. SIAM; 1992.

David CT. Visual control of the partition of flight force between lift and thrust in free-flying Drosophila. Nature. 1985 Jan 3;313(5997):48–50.

Degallier S, Ijspeert A. Modeling discrete and rhythmic movements through motor primitives: a review. Biol Cybern. 2010 Oct;103(4):319–38.

Derham W. Physico-theology, Or, A Demonstration of the Being and Attributes of God from His Works of Creation: Being the Substance of Sixteen Sermons Preached in St. Mary-le-Bow Church, London, at the Honourable Mr. Boyle's Lectures, in the Years 1711, and 1712 : with Large Notes, and Many Curious Observations. W. and J. Innys; 1720.

Desmedt JE, editor. Physiological tremor, pathological tremors and clonus. Basel ; New York: S. Karger; 1978. (Progress in clinical neurophysiology).

Deuschl G, Raethjen J, Lindemann M, Krack P. The pathophysiology of tremor. Muscle Nerve. 2001 Jun;24(6):716–35.

Dicaprio null. Plateau potentials in motor neurons in the ventilatory system of the crab. J Exp Biol. 1997;200(Pt 12):1725–36.

Dickinson MH. Haltere-mediated equilibrium reflexes of the fruit fly, Drosophila melanogaster. Philos Trans R Soc Lond B Biol Sci. 1999 May 29;354(1385):903–16.

Dickinson MH. The initiation and control of rapid flight maneuvers in fruit flies. Integr Comp Biol. 2005 Apr 1;45(2):274–81.

Dickinson MH, Farley CT, Full RJ, Koehl MAR, Kram R, Lehman S. How animals move: an integrative view. Science. 2000 Apr 7;288(5463):100–6.

Dickinson MH, Lehmann F-O, Chan WP. The Control of Mechanical Power in Insect Flight. Am Zool. 1998a;38(4):718–28.

Dickinson MH, Lehmann F-O, Chan WP. The Control of Mechanical Power in Insect Flight. Am Zool. 1998b;38(4):718–28.

Dickinson MH, Lehmann FO, Gotz KG. The active control of wing rotation by Drosophila. J Exp Biol. 1993 Sep 1;182(1):173–89.

Dickinson MH, Lehmann F-O, Sane SP. Wing rotation and the aerodynamic basis of insect flight. Science. 1999 Jun 18;284(5422):1954–60.

Dickinson MH, Tu MS. The function of dipteran flight muscle. Comp Biochem Physiol A Physiol. 1997 Mar;116(3):223–38.

Dickson WB, Straw AD, Dickinson MH. Integrative model of drosophila flight. AIAA J. 2008;46(9):2150–64.

Dietz V, Quintern J, Sillem M. Stumbling reactions in man: significance of proprioceptive and pre-programmed mechanisms. J Physiol. 1987 May;386:149–63.

Dudley R. The biomechanics of insect flight: form, function, evolution. 2. print., 1. paperback print. Princeton, NJ: Princeton Univ. Press; 2002.

Dupuis MJM, Delwaide PJ, Boucquey D, Gonsette RE. Homolateral disappearance of essential tremor after cerebellar stroke. Mov Disord. 1989;4(2):183–7.

Elble R, Bain P, João Forjaz M, Haubenberger D, Testa C, Goetz CG, et al. Task force report: Scales for screening and evaluating tremor: Critique and recommendations: Tremor Scales. Mov Disord. 2013 Nov;28(13):1793–800.

Elble RJ. Central mechanisms of tremor. J Clin Neurophysiol Off Publ Am Electroencephalogr Soc. 1996 Mar;13(2):133–44.

Elble RJ. Gravitational artifact in accelerometric measurements of tremor. Clin Neurophysiol Off J Int Fed Clin Neurophysiol. 2005 Jul;116(7):1638–43.

Elble RJ. Tremor disorders. Curr Opin Neurol. 2013a Aug;26(4):413–9.

Elble RJ. What is Essential Tremor? Curr Neurol Neurosci Rep. 2013b Jun;13(6).

Elble RJ, Higgins C, Hughes L. Longitudinal study of essential tremor. Neurology. 1992 Feb;42(2):441–3.

Elble RJ, Randall JE. Motor-unit activity responsible for 8- to 12-Hz component of human physiological finger tremor. J Neurophysiol. 1976 Mar;39(2):370–83.

Elson MS, Berkowitz A. Flexion Reflex Can Interrupt and Reset the Swimming Rhythm. J Neurosci. 2016 Mar 2;36(9):2819–26.

Faes L, Pinna GD, Porta A, Maestri R, Nollo G. Surrogate data analysis for assessing the significance of the coherence function. IEEE Trans Biomed Eng. 2004 Jul;51(7):1156–66.

Faisal AA, Selen LPJ, Wolpert DM. Noise in the nervous system. Nat Rev Neurosci. 2008 Apr;9(4):292–303.

Farina D, Negro F. Common Synaptic Input to Motor Neurons, Motor Unit Synchronization, and Force Control: Exerc Sport Sci Rev. 2015 Jan;43(1):23–33.

Farina D, Negro F, Dideriksen JL. The effective neural drive to muscles is the common synaptic input to motor neurons: Effective neural drive to muscles. J Physiol. 2014 Aug 15;592(16):3427–41.

Faruque I, Sean Humbert J. Dipteran insect flight dynamics. Part 1 Longitudinal motion about hover. J Theor Biol. 2010a May 21;264(2):538–52.

Faruque I, Sean Humbert J. Dipteran insect flight dynamics. Part 2: Lateral–directional motion about hover. J Theor Biol. 2010b Aug 7;265(3):306–13.

Fasano A, Herzog J, Raethjen J, Rose FEM, Muthuraman M, Volkmann J, et al. Gait ataxia in essential tremor is differentially modulated by thalamic stimulation. Brain. 2010 Dec 1;133(12):3635–48.

Fayyazuddin A, Dickinson MH. Haltere afferents provide direct, electrotonic input to a steering motor neuron in the blowfly, Calliphora. J Neurosci Off J Soc Neurosci. 1996 Aug 15;16(16):5225–32.

Fayyazuddin A, Dickinson MH. Convergent mechanosensory input structures the firing phase of a steering motor neuron in the blowfly, Calliphora. J Neurophysiol. 1999 Oct;82(4):1916–26.

Fentress JC, Stilwell FP. Grammar of a Movement Sequence in Inbred Mice. Nature. 1973 Jul 6;244(5410):52–3.

Flash T, Hochner B. Motor primitives in vertebrates and invertebrates. Curr Opin Neurobiol. 2005 Dec;15(6):660–6.

Fod A, Matarić MJ, Jenkins OC. Automated Derivation of Primitives for Movement Classification. Auton Robots. 2002;12(1):39–54.

Fox JL, Daniel TL. A neural basis for gyroscopic force measurement in the halteres of Holorusia. J Comp Physiol A Neuroethol Sens Neural Behav Physiol. 2008 Oct;194(10):887–97.

Fraenkel G, Pringle JWS. Biological Sciences: Halteres of Flies as Gyroscopic Organs of Equilibrium. Nature. 1938 May 21;141(3577):919–20.

Fry SN, Sayaman R, Dickinson MH. The aerodynamics of free-flight maneuvers in Drosophila. Science. 2003 Apr 18;300(5618):495–8.

Fry SN, Sayaman R, Dickinson MH. The aerodynamics of hovering flight in Drosophila. J Exp Biol. 2005 Jun 15;208(12):2303–18.

Frye MA, Dickinson MH. Fly flight: A model for the neural control of complex behavior. Neuron. 2001 Nov 8;32(3):385–8.

Frye MA, Dickinson MH. Motor output reflects the linear superposition of visual and olfactory inputs in Drosophila. J Exp Biol. 2004 Jan;204:123–31.

Geurten BRH, Kern R, Braun E, Egelhaaf M. A syntax of hoverfly flight prototypes. J Exp Biol. 2010 Jul 15;213(Pt 14):2461–75.

Ghahramani Z. Computational neuroscience: Building blocks of movement. Nature. 2000 Oct 12;407(6805):682–3.

Gnatzy W, Grünert U, Bender M. Campaniform sensilla of Calliphora vicina (Insecta, Diptera). Zoomorphology. 1987 Mar;106(5):312–9.

Gordon AM, Huxley AF, Julian FJ. Tension development in highly stretched vertebrate muscle fibres. J Physiol. 1966a May 1;184(1):143–69.

Gordon AM, Huxley AF, Julian FJ. The variation in isometric tension with sarcomere length in vertebrate muscle fibres. J Physiol. 1966b May;184(1):170–92.

Goslow GE, Seeherman HJ, Taylor CR, McCutchin MN, Heglund NC. Electrical activity and relative length changes of dog limb muscles as a function of speed and gait. J Exp Biol. 1981 Oct 1;94(1):15–42.

Gotz KG. Bewegungssehen und flugsteuerung bei der fliege Drosophila. In: BIONA report. Fischer, Stuttgart; 1983. p. 21–34. (2).

Graetzel CF, Fry SN, Nelson BJ. A 6000 Hz computer vision system for real-time wing beat analysis of Drosophila. In: The First IEEE/RAS-EMBS International Conference on Biomedical Robotics and Biomechatronics, 2006 BioRob 2006. 2006. p. 278–83.

Greenspan RJ, Dierick HA. “Am not I a fly like thee?” From genes in fruit flies to behavior in humans. Hum Mol Genet. 2004 Oct 1;13(suppl_2):R267–73.

Grenander U. On empirical spectral analysis of stochastic processes. Ark För Mat. 1951 Aug;1(6):503–31.

Grillner S, Wallén P, Brodin L, Lansner A. Neuronal network generating locomotor behavior in lamprey: circuitry, transmitters, membrane properties, and simulation. Annu Rev Neurosci. 1991;14:169–99.

Grinsted A, Moore JC, Jevrejeva S. Application of the cross wavelet transform and wavelet coherence to geophysical time series. Nonlin Process Geophys. 2004 Nov 18;11(5/6):561–6.

Grosse P, Cassidy MJ, Brown P. EEG-EMG, MEG-EMG and EMG-EMG frequency analysis: physiological principles and clinical applications. Clin Neurophysiol Off J Int Fed Clin Neurophysiol. 2002 Oct;113(10):1523–31.

Guertin PA. The mammalian central pattern generator for locomotion. Brain Res Rev. 2009 Dec;62(1):45–56.

Hagbarth KE, Young RR. Participation of the stretch reflex in human physiological tremor. Brain J Neurol. 1979 Sep;102(3):509–26.

Hallett M. Physiology of Psychogenic Movement Disorders. J Clin Neurosci Off J Neurosurg Soc Australas. 2010 Aug;17(8):959–65.

Hallett M. Tremor: Pathophysiology. Parkinsonism Relat Disord. 2014 Jan;20:S118–22.

Hallett M, Dubinsky RM. Glucose metabolism in the brain of patients with essential tremor. J Neurol Sci. 1993 Jan;114(1):45–8.

Halliday DM, Conway BA, Farmer SF, Rosenberg JR. Load-independent contributions from motor-unit synchronization to human physiological tremor. J Neurophysiol. 1999 Aug;82(2):664–75.

Halliday DM, Rosenberg JR, Amjad AM, Breeze P, Conway BA, Farmer SF. A framework for the analysis of mixed time series/point process data--theory and application to the study of physiological tremor, single motor unit discharges and electromyograms. Prog Biophys Mol Biol. 1995;64(2–3):237–78.

Hardie RC, Raghu P. Visual transduction in Drosophila. Nature. 2001 Sep 13;413(6852):186–93.

Haridas C, Zehr EP, Misiaszek JE. Postural uncertainty leads to dynamic control of cutaneous reflexes from the foot during human walking. Brain Res. 2005 Nov 16;1062(1–2):48–62.

Hausdorff JM, Rios DA, Edelberg HK. Gait variability and fall risk in community-living older adults: a 1-year prospective study. Arch Phys Med Rehabil. 2001 Aug;82(8):1050–6.

Hedenström A. How Insect Flight Steering Muscles Work. PLoS Biol. 2014 Mar 25;12(3):e1001822.

Heide G, Götz KG. Optomotor control of course and altitude in Drosophila melanogaster is correlated with distinct activities of at least three pairs of flight steering muscles. J Exp Biol. 1996 Aug;199(Pt 8):1711–26.

Heisenberg M, Wolf R. On the fine structure of yaw torque in visual flight orientation of Drosophila melanogaster. J Comp Physiol. 1979 Jun 1;130(2):113–30.

Heisenberg M, Wolf R. Reafferent control of optomotor yaw torque in Drosophila melanogaster. J Comp Physiol A. 1988 May 1;163(3):373–88.

Hellwig B, Häussler S, Schelter B, Lauk M, Guschlbauer B, Timmer J, et al. Tremor-correlated cortical activity in essential tremor. Lancet Lond Engl. 2001 Feb 17;357(9255):519–23.

Hellwig B, Schelter B, Guschlbauer B, Timmer J, Lücking CH. Dynamic synchronisation of central oscillators in essential tremor. Clin Neurophysiol Off J Int Fed Clin Neurophysiol. 2003 Aug;114(8):1462–7.

Hess CW, Pullman SL. Tremor: Clinical Phenomenology and Assessment Techniques. Tremor Hyperkinetic Mov . 2012 Jun 28

Hogan N, Sternad D. On rhythmic and discrete movements: reflections, definitions and implications for motor control. Exp Brain Res. 2007 Jul;181(1):13–30.

Hogan N, Sternad D. Dynamic primitives of motor behavior. Biol Cybern. 2012 Dec;106(11–12):727–39.

Holmes G. The symptoms of acute cerebellar injuries due to gunshot injuries. Brain. 1917;40(4):461–535.

Hong Y, Brueggemann G-P. Changes in gait patterns in 10-year-old boys with increasing loads when walking on a treadmill. Gait Posture. 2000 Jun 1;11(3):254–9.

Horak FB. Postural orientation and equilibrium: what do we need to know about neural control of balance to prevent falls? Age Ageing. 2006 Sep 1;35(suppl 2):ii7-ii11.

Hua SE. Posture-Related Oscillations in Human Cerebellar Thalamus in Essential Tremor Are Enabled by Voluntary Motor Circuits. J Neurophysiol. 2004 Aug 18;93(1):117–27.

Hughes GM, Wiersma C a. G. The Co-ordination of Swimmeret Movements in the Crayfish, Procambarus Clarkii (Girard). J Exp Biol. 1960 Dec 1;37(4):657–70.

Huston SJ, Krapp HG. Nonlinear integration of visual and haltere inputs in fly neck motor neurons. J Neurosci Off J Soc Neurosci. 2009 Oct 21;29(42):13097–105.

Hyvarinen A. Fast and robust fixed-point algorithms for independent component analysis. IEEE Trans Neural Netw. 1999;10(3):626–34.

Hyvarinen A, Karhunen J, Oja E. Independent Component Analysis. S.l: Wiley-Interscience; 2001.

Hyvärinen A, Oja E. Independent component analysis: algorithms and applications. Neural Netw Off J Int Neural Netw Soc. 2000 Jun;13(4–5):411–30.

Ishiwata S, Shimamoto Y, Fukuda N. Contractile system of muscle as an auto-oscillator. Prog Biophys Mol Biol. 2011 May;105(3):187–98.

Ivanenko YP. Coordination of Locomotion with Voluntary Movements in Humans. J Neurosci. 2005 Aug 3;25(31):7238–53.

Jacobson S, Marcus EM. Neuroanatomy for the neuroscientist. New York, NY: Springer; 2008.

Jennings BH. Drosophila – a versatile model in biology & medicine. Mater Today. 2011 May;14(5):190–5.

Jerbi K, Lachaux J-P, N'Diaye K, Pantazis D, Leahy RM, Garnero L, et al. Coherent neural representation of hand speed in humans revealed by MEG imaging. Proc Natl Acad Sci. 2007 May 1;104(18):7676–81.

Katz PS. Evolution of central pattern generators and rhythmic behaviours. Phil Trans R Soc B. 2016 Jan 5;371(1685):20150057.

Kavanagh JJ, Cresswell AG, Sabapathy S, Carroll TJ. Bilateral tremor responses to unilateral loading and fatiguing muscle contractions. J Neurophysiol. 2013 Jul 15;110(2):431–40.

Kiehn O. Decoding the organization of spinal circuits that control locomotion. Nat Rev Neurosci. 2016 Apr;17(4):224–38.

Kiehn O, Eken T. Prolonged Firing in Motor Units: Evidence of Plateau Potentials in Human Motoneurons? J Neurophysiol. 1997 Dec 1;78(6):3061–8.

Kiehn O, Kjaerulff O, Tresch MC, Harris-Warrick RM. Contributions of intrinsic motor neuron properties to the production of rhythmic motor output in the mammalian spinal cord. Brain Res Bull. 2000 Nov 15;53(5):649–59.

Kimura T, Haggard P, Gomi H. Transcranial magnetic stimulation over sensorimotor cortex disrupts anticipatory reflex gain modulation for skilled action. J Neurosci Off J Soc Neurosci. 2006 Sep 6;26(36):9272–81.

Klapp ST. Doing two things at once: The role of temporal compatibility. Mem Cognit. 1979;7(5):375–81.

Kraskov A, Stögbauer H, Grassberger P. Estimating mutual information. Phys Rev E. 2004 Jun 23;69(6):66138.

Lakie M, Vernooij CA, Osborne TM, Reynolds RF. The resonant component of human physiological hand tremor is altered by slow voluntary movements. J Physiol. 2012 May 1;590(Pt 10):2471–83.

Lakie M, Walsh EG, Wright GW. Passive mechanical properties of the wrist and physiological tremor. J Neurol Neurosurg Psychiatry. 1986 Jun 1;49(6):669–76.

Land MF, Collett TS. Chasing behaviour of houseflies (Fannia canicularis). J Comp Physiol. 1974 Dec;89(4):331–57.

Lauk M, Köster B, Timmer J, Guschlbauer B, Deuschl G, Lücking CH. Side-to-side correlation of muscle activity in physiological and pathological human tremors. Clin Neurophysiol Off J Int Fed Clin Neurophysiol. 1999 Oct;110(10):1774–83.

Lehmann FO, Dickinson MH. The control of wing kinematics and flight forces in fruit flies (Drosophila spp.). J Exp Biol. 1998 Feb 1;201(3):385–401.

Lehmann FO, Götz KG. Activation phase ensures kinematic efficacy in flight-steering muscles of Drosophila melanogaster. J Comp Physiol A. 1996 Sep;179(3):311–22.

Lehmann F-O, Pick S. The aerodynamic benefit of wing–wing interaction depends on stroke trajectory in flapping insect wings. J Exp Biol. 2007 Apr 15;210(8):1362–77.

Lindqvist T. Finger tremor and the α-waves of the electro-encephalogram. Acta Med Scand. 1941 Jan 12;108(6):580–5.

Louis ED. Essential tremor. Lancet Neurol. 2005 Feb;4(2):100–10.

Louis ED. Essential tremors: a family of neurodegenerative disorders? Arch Neurol. 2009 Oct;66(10):1202–8.

Louis ED. Essential tremor: evolving clinicopathological concepts in an era of intensive post-mortem enquiry. Lancet Neurol. 2010 Jun;9(6):613–22.

Louis ED, Babij R, Cortés E, Vonsattel J-PG, Faust PL. The inferior olivary nucleus: a postmortem study of essential tremor cases versus controls. Mov Disord Off J Mov Disord Soc. 2013 Jun;28(6):779–86.

Louis ED, Barnes L, Albert SM, Cote L, Schneier FR, Pullman SL, et al. Correlates of functional disability in essential tremor. Mov Disord Off J Mov Disord Soc. 2001 Sep;16(5):914–20.

Louis ED, Faust PL, Vonsattel J-PG, Honig LS, Rajput A, Robinson CA, et al. Neuropathological changes in essential tremor: 33 cases compared with 21 controls. Brain J Neurol. 2007 Dec;130(Pt 12):3297–307.

Louis ED, Ferreira JJ. How common is the most common adult movement disorder? Update on the worldwide prevalence of essential tremor. Mov Disord. 2010 Apr 15;25(5):534–41.

Louis ED, Jurewicz EC, Applegate L, Factor-Litvak P, Parides M, Andrews L, et al. Association between essential tremor and blood lead concentration. Environ Health Perspect. 2003 Nov;111(14):1707–11.

Louis ED, Ottman R, Hauser WA. How common is the most common adult movement disorder? estimates of the prevalence of essential tremor throughout the world. Mov Disord Off J Mov Disord Soc. 1998 Jan;13(1):5–10.

Louis ED, Zheng W, Jurewicz EC, Watner D, Chen J, Factor-Litvak P, et al. Elevation of blood beta-carboline alkaloids in essential tremor. Neurology. 2002 Dec 24;59(12):1940–4.

Mallat S. A Wavelet Tour of Signal Processing. Academic Press; 1999.

Marder E, Bucher D. Central pattern generators and the control of rhythmic movements. Curr Biol CB. 2001 Nov 27;11(23):R986-996.

Marder E, Calabrese RL. Principles of rhythmic motor pattern generation. Physiol Rev. 1996 Jul 1;76(3):687–717.

Marsden CD, Meadows JC, Lange GW, Watson RS. Effect of deafferentation on human physiological tremor. The Lancet. 1967 Sep;290(7518):700–2.

Marsden CD, Meadows JC, Lange GW, Watson RS. The relation between physiological tremor of the two hands in healthy subjects. Electroencephalogr Clin Neurophysiol. 1969a Aug;27(2):179–85.

Marsden CD, Meadows JC, Lange GW, Watson RS. The relation between physiological tremor of the two hands in healthy subjects. Electroencephalogr Clin Neurophysiol. 1969b Aug;27(2):179–85.

Marsden CD, Meadows JC, Lange GW, Watson RS. The Role of the Ballistocardiac Impulse in the Genesis of Physiological Tremor. Brain. 1969c Mar 1;92(3):647–62.

Mataric MJ, Zordan VB, Williamson MW. Making complex articulated agents dance: An analysis of control methods drawn from robotics, animation, and biology. Auton Agents Multi-Agent Syst. 1999 Mar;2(1):23–44.

Maul H, Maner WL, Saade GR, Garfield RE. The physiology of uterine contractions. Clin Perinatol. 2003 Dec;30(4):665–76.

Mazzaro N, Grey MJ, Sinkjaer T, Andersen JB, Pareyson D, Schieppati M. Lack of on-going adaptations in the soleus muscle activity during walking in patients affected by large-fiber neuropathy. J Neurophysiol. 2005 Jun;93(6):3075–85.

McAuley J, Rothwell J. Identification of psychogenic, dystonic, and other organic tremors by a coherence entrainment test. Mov Disord. 2004 Mar 1;19(3):253–67.

McAuley JH, Marsden CD. Physiological and pathological tremors and rhythmic central motor control. Brain. 2000 Aug 1;123(8):1545–67.

McAuley JH, Rothwell JC, Marsden CD. Frequency peaks of tremor, muscle vibration and electromyographic activity at 10 Hz, 20 Hz and 40 Hz during human finger muscle contraction may reflect rhythmicities of central neural firing: Exp Brain Res. 1997 May 13;114(3):525–41.

Mehta AR, Brittain J-S, Brown P. The Selective Influence of Rhythmic Cortical versus Cerebellar Transcranial Stimulation on Human Physiological Tremor. J Neurosci. 2014 May 28;34(22):7501–8.

Miyan JA, Ewing AW. How Diptera Move Their Wings: A re-Examination of the Wing Base Articulation and Muscle Systems Concerned with Flight. Philos Trans R Soc B Biol Sci. 1985 Nov 19;311(1150):271–302.

Mold JW, Vesely SK, Keyl BA, Schenk JB, Roberts M. The prevalence, predictors, and consequences of peripheral sensory neuropathy in older patients. J Am Board Fam Pract. 2004 Oct;17(5):309–18.

Moore GP, Ding L, Bronte-Stewart HM. Concurrent Parkinson tremors. J Physiol. 2000 Nov 15;529(1):273–81.

Morrison S, Newell KM. Bilateral organization of physiological tremor in the upper limb. Eur J Appl Physiol. 1999 Dec;80(6):564–74.

Morrison S, Newell KM. Postural and resting tremor in the upper limb. Clin Neurophysiol Off J Int Fed Clin Neurophysiol. 2000 Apr;111(4):651–63.

Muijres FT, Elzinga MJ, Melis JM, Dickinson MH. Flies Evade Looming Targets by Executing Rapid Visually Directed Banked Turns. Science. 2014 Apr 11;344(6180):172–7.

Mulloney B, Smarandache C. Fifty Years of CPGs: Two Neuroethological Papers that Shaped the Course of Neuroscience. Front Behav Neurosci. 2010;4.

Mureli S, Fox JL. Haltere mechanosensory influence on tethered flight behavior in Drosophila. J Exp Biol. 2015 Aug 1;218(16):2528–37.

Murthy VN, Fetz EE. Oscillatory activity in sensorimotor cortex of awake monkeys: synchronization of local field potentials and

relation to behavior. J Neurophysiol. 1996 Dec;76(6):3949–67.

Muthuraman M, Hellriegel H, Paschen S, Hofschulte F, Reese R, Volkmann J, et al. The central oscillatory network of orthostatic tremor. Mov Disord. 2013 Sep 1;28(10):1424–30.

Nalbach G. The halteres of the blowfly Calliphora: I. Kinematics and dynamics. J Comp Physiol A. 1993 Sep;173(3):293–300.

Negro F, Holobar A, Farina D. Fluctuations in isometric muscle force can be described by one linear projection of low-frequency components of motor unit discharge rates: Principal components of motor unit discharge rates. J Physiol. 2009 Dec 15;587(24):5925–38.

Nichols CD. Drosophila melanogaster neurobiology, neuropharmacology, and how the fly can inform central nervous system drug discovery. Pharmacol Ther. 2006 Dec;112(3):677–700.

Okamura N, Ishiwata S 'ichi. Spontaneous oscillatory contraction of sarcomeres in skeletal myofibrils. J Muscle Res Cell Motil. 1988 Apr;9(2):111–9.

Peterka RJ. Sensorimotor Integration in Human Postural Control. J Neurophysiol. 2002 Sep 1;88(3):1097–118.

Pierrot-Desseilligny E, Burke DC. The circuitry of the human spinal cord: its role in motor control and movement disorders. Cambridge: Cambridge University Press; 2005.

Pikovsky A, Rosenblum M, Kurths J. Synchronization: A Universal Concept in Nonlinear Sciences. Cambridge University Press; 2003.

Pinto AD, Lang AE, Chen R. The cerebellothalamocortical pathway in essential tremor. Neurology. 2003 Jun 24;60(12):1985–7.

Placantonakis DG, Bukovsky AA, Zeng X-H, Kiem H-P, Welsh JP. Fundamental role of inferior olive connexin 36 in muscle coherence during tremor. Proc Natl Acad Sci U S A. 2004 May 4;101(18):7164–9.

Priestley MB. Spectral analysis and time series: vol. 1: univariate series ; vol. 2: multivariate series, prediction and control. San Diego [u.a.]: Acad. Press; 2001.

Pringle JWS. The Gyroscopic Mechanism of the Halteres of Diptera. Philos Trans R Soc Lond B Biol Sci. 1948 Nov 2;233(602):347–84.

Prisk GK, Verhaeghe S, Padeken D, Hamacher H, Paiva M. Three-dimensional ballistocardiography and respiratory motion in sustained microgravity. Aviat Space Environ Med. 2001 Dec;72(12):1067–74.

Prochazka A, Trend PS. Instability in human forearm movements studied with feed-back-controlled muscle vibration. J Physiol. 1988 Aug;402:421.

Pruszynski JA, Kurtzer I, Scott SH. The long-latency reflex is composed of at least two functionally independent processes. J Neurophysiol. 2011 Jul 1;106(1):449–59.

Pullman SL. Spiral Analysis: A New Technique for Measuring Tremor With a Digitizing Tablet. Mov Disord. 1998 Oct 20;13(S3):85–9.

Raethjen J, Deuschl G. The oscillating central network of Essential tremor. Clin Neurophysiol. 2012 Jan;123(1):61–4.

Raethjen J, Govindan RB, Kopper F, Muthuraman M, Deuschl G. Cortical Involvement in the Generation of Essential Tremor. J Neurophysiol. 2007 Mar 7;97(5):3219–28.

Raethjen J, Kopper F, Govindan RB, Volkmann J, Deuschl G. Two different pathogenetic mechanisms in psychogenic tremor. Neurology. 2004 Sep 14;63(5):812–5.

Raethjen J, Lindemann M, Dümpelmann M, Wenzelburger R, Stolze H, Pfister G, et al. Corticomuscular coherence in the 6-15 Hz band: is the cortex involved in the generation of physiologic tremor? Exp Brain Res. 2002 Jan 1;142(1):32–40.

Raethjen J, Lindemann M, Schmaljohann H, Wenzelburger R, Pfister G, Deuschl G. Multiple oscillators are causing parkinsonian and essential tremor. Mov Disord Off J Mov Disord Soc. 2000a Jan;15(1):84–94.

Raethjen J, Pawlas F, Lindemann M, Wenzelburger R, Deuschl G. Determinants of physiologic tremor in a large normal population. Clin Neurophysiol Off J Int Fed Clin Neurophysiol. 2000b Oct;111(10):1825–37.

Ristroph L, Bergou AJ, Ristroph G, Coumes K, Berman GJ, Guckenheimer J, et al. Discovering the flight autostabilizer of fruit flies by inducing aerial stumbles. Proc Natl Acad Sci.

Ristroph L, Ristroph G, Morozova S, Bergou AJ, Chang S, Guckenheimer J, et al. Active and passive stabilization of body pitch in insect flight. J R Soc Interface. 2013 Aug 6;10(85):20130237.

Rosenbaum DA. Human motor control. 2nd ed. Amsterdam ; Boston, MA: Elsevier Inc; 2010.

Rothwell JC. Physiology and anatomy of possible oscillators in the central nervous system. Mov Disord Off J Mov Disord Soc. 1998;13 Suppl 3:24–8.

Ruegg JC, Steiger GJ, Schadler M. Mechanical activation of the contractile system in skeletal muscle. Pflugers Arch Eur J Physiol. 1970;319(2):139–45.

Ryckebusch S, Laurent G. Rhythmic patterns evoked in locust leg motor neurons by the muscarinic agonist pilocarpine. J Neurophysiol. 1993 May;69(5):1583–95.

Sane SP, Dickinson MH. The control of flight force by a flapping wing: lift and drag production. J Exp Biol. 2001 Aug 1;204(15):2607–26.

Sanes JN, Donoghue JP. Oscillations in local field potentials of the primate motor cortex during voluntary movement. Proc Natl Acad Sci U S A. 1993 May 15;90(10):4470–4.

Sanger TD. Human arm movements described by a low-dimensional superposition of principal components. J Neurosci Off J Soc Neurosci. 2000 Feb 1;20(3):1066–72.

Schaal S. Dynamic Movement Primitives -A Framework for Motor Control in Humans and Humanoid Robotics. In: Kimura H, Tsuchiya K, Ishiguro A, Witte H, editors. Adaptive Motion of Animals and Machines . Tokyo: Springer Tokyo; 2006. p. 261–80.

Schaal S, Sternad D, Osu R, Kawato M. Rhythmic arm movement is not discrete. Nat Neurosci. 2004 Oct;7(10):1136–43.

Schafer WR. Mechanosensory molecules and circuits in C. elegans. Pflugers Arch. 2015;467:39–48.

Schlurmann M, Hausen K. Motoneurons of the flight power muscles of the blowfly Calliphora erythrocephala : Structures and mutual dye coupling. J Comp Neurol. 2007 Jan 20;500(3):448–64.

Schnitzler A, Münks C, Butz M, Timmermann L, Gross J. Synchronized brain network associated with essential tremor as revealed by magnetoencephalography. Mov Disord Off J Mov Disord Soc. 2009 Aug 15;24(11):1629–35.

Schreiber T, Schmitz A. Improved Surrogate Data for Nonlinearity Tests. Phys Rev Lett. 1996 Jul 22;77(4):635–8.

Schuessler RB, Boineau JP, Bromberg BI. Origin of the sinus impulse. J Cardiovasc Electrophysiol. 1996 Mar;7(3):263–74.

Schwab RS, Cobb S. Simultaneous electromyograms and electroencephalograms in paralysis agitans. J Neurophysiol. 1939 Jan 1;2(1):36–41.

Semmler JG. Motor unit synchronization and neuromuscular performance. Exerc Sport Sci Rev. 2002 Jan;30(1):8–14.

Shemmell J, An JH, Perreault EJ. The differential role of motor cortex in stretch reflex modulation induced by changes in environmental mechanics and verbal instruction. J Neurosci Off J Soc Neurosci. 2009 Oct 21;29(42):13255–63.

Simonsen EB. Contributions to the understanding of gait control. Dan Med J. 2014 Apr;61(4):B4823.

Sláma K. A new look at the comparative physiology of insect and human hearts. J Insect Physiol. 2012 Aug;58(8):1072–81.

Sláma K, Lukáš J. Myogenic nature of insect heartbeat and intestinal peristalsis, revealed by neuromuscular paralysis caused by the sting of a braconid wasp. J Insect Physiol. 2011 Feb;57(2):251–9.

Smith DS. The Structure of Insect Muscles. In: King RC, Akai H, editors. Insect Ultrastructure: Volume 2. Boston, MA: Springer US; 1984. p. 111–50.

Šprdlík O, Hurák Z, Hoskovcová M, Ulmanová O, Růžička E. Tremor analysis by decomposition of acceleration into gravity and inertial acceleration using inertial measurement unit. Biomed Signal Process Control. 2011 Jul;6(3):269–79.

Staras K, Kemenes G, Benjamin PR. Pattern-Generating Role for Motoneurons in a Rhythmically Active Neuronal Network. J Neurosci. 1998 May 15;18(10):3669–88.

Stögbauer H, Kraskov A, Astakhov SA, Grassberger P. Least-dependent-component analysis based on mutual information. Phys Rev E. 2004 Dec 13;70(6):66123.

Sun M, Xiong Y. Dynamic flight stability of a hovering bumblebee. J Exp Biol. 2005 Feb;208(Pt 3):447–59.

Szent-Györgyi AG. Calcium regulation of muscle contraction. Biophys J. 1975 Jul;15(7):707–23.

Tammero LF, Dickinson MH. Collision-avoidance and landing responses are mediated by separate pathways in the fruit fly, Drosophila melanogaster. J Exp Biol. 2002 Sep 15;205(18):2785–98.

Taylor GK. Mechanics and aerodynamics of insect flight control. Biol Rev Camb Philos Soc. 2001 Nov;76(4):449–71.

Thoroughman KA, Shadmehr R. Learning of action through adaptive combination of motor primitives. Nature. 2000 Oct 12;407(6805):742–7.

Timmer J, Lauk M, Deuschl G. Quantitative analysis of tremor time series. Electroencephalogr Clin Neurophysiol. 1996 Oct;101(5):461–8.

Timmer J, Lauk M, Haussler S, Radt V, Koster B, Hellwig B, et al. Cross-spectral analysis of tremor time series. Int J Bifurc Chaos. 2000a;10:2595–610.

Timmer J, Lauk M, Haussler S, Radt V, Koster B, Hellwig B, et al. Cross-spectral analysis of tremor time series. Int J Bifurc Chaos. 2000b;10:2595–610.

Torrence C, Compo GP. A Practical Guide to Wavelet Analysis. Bull Am Meteorol Soc. 1998a;79:61–78.

Torrence C, Compo GP. A Practical Guide to Wavelet Analysis. Bull Am Meteorol Soc. 1998b Jan 1;79(1):61–78.

Tresch MC, Kiehn O. Motor coordination without action potentials in the mammalian spinal cord. Nat Neurosci. 2000;3:593–9.

Trimarchi JR, Murphey RK. The shaking-B2 mutation disrupts electrical synapses in a flight circuit in adult Drosophila. J Neurosci Off J Soc Neurosci. 1997 Jun 15;17(12):4700–10.

Tripodi M, Stepien AE, Arber S. Motor antagonism exposed by spatial segregation and timing of neurogenesis. Nature. 2011 Nov 3;479(7371):61–6.

Truong TQ, Phan VH, Sane SP, Park HC. Pitching moment generation in an insect-mimicking flapping-wing system. J Bionic Eng. 2014 Jan;11(1):36–51.

Tu MS, Dickinson MH. The control of wing kinematics by two steering muscles of the blowfly (Calliphora vicina). J Comp Physiol A. 1996 Jun;178(6):813–30.

Vernooij CA, Reynolds RF, Lakie M. A dominant role for mechanical resonance in physiological finger tremor revealed by selective minimization of voluntary drive and movement. J Neurophysiol. 2013 May;109(9):2317–26.

Victor JD. Binless strategies for estimation of information from neural data. Phys Rev E Stat Nonlin Soft Matter Phys. 2002 Nov;66(5 Pt 1):51903.

Vigoreaux JO. Nature's versatile engine: insect flight muscle inside and out. Georgetown, Tex. : New York, N.Y: Landes Bioscience/Eurekah.com ; Springer Science+Business Media; 2006. (Molecular biology intelligence unit).

Walker SM, Schwyn DA, Mokso R, Wicklein M, Müller T, Doube M, et al. In Vivo Time-Resolved Microtomography Reveals the Mechanics of the Blowfly Flight Motor. PLoS Biol. 2014 Mar 25;12(3):e1001823.

Wang S-Y, Liu X, Yianni J, Christopher Miall R, Aziz TZ, Stein JF. Optimising coherence estimation to assess the functional correlation of tremor-related activity between the subthalamic nucleus and the forearm muscles. J Neurosci Methods. 2004 Jul 30;136(2):197–205.

Wen Q, Po MD, Hulme E, Chen S, Liu X, Kwok SW, et al. Proprioceptive Coupling within Motor Neurons Drives C. elegans Forward Locomotion. Neuron. 2012 Nov 21;76(4):750–61.

West BJ, Scafetta N. Nonlinear dynamical model of human gait. Phys Rev E. 2003 May 20;67(5).

Whaley NR, Putzke JD, Baba Y, Wszolek ZK, Uitti RJ. Essential tremor: phenotypic expression in a clinical cohort. Parkinsonism Relat Disord. 2007 Aug;13(6):333–9.

Wills AJ, Jenkins IH, Thompson PD, Findley LJ, Brooks DJ. Red nuclear and cerebellar but no olivary activation associated with essential tremor: A positron emission tomoraphic study. Ann Neurol. 1994 Oct;36(4):636–42.

Wilson DM. The central nervous control of flight in a locust. J Exp Biol. 1961 Jun 1;38(2):471–90.

Wilson DM. Central nervous mechanisms for the generation of rhythmic behaviour in arthropods. Symp Soc Exp Biol. 1966;20:199–228.

Wilson DM, Wyman RJ. Motor Output Patterns during Random and Rhythmic Stimulation of Locust Thoracic Ganglia. Biophys J. 1965 Mar;5(2):121–43.

Wolpert DM, Flanagan JR. Q&A: Robotics as a tool to understand the brain. BMC Biol. 2010 Jul 23;8:92.

Zanker JM. On the mechanism of speed and altitude control in Drosophila melanogaster. Physiol Entomol. 1988;13(3):351–361.

Zanker JM. The Wing Beat of Drosophila Melanogaster. I. Kinematics. Philos Trans R Soc Lond B Biol Sci. 1990a Feb 28;327(1238):1–18.

Zanker JM. The wing beat of Drosophila melanogaster. III. Control. Philos Trans R Soc Lond B Biol Sci. 1990b Feb 28;327(1238):45–64.

Zatorre RJ, Chen JL, Penhune VB. When the brain plays music: auditory–motor interactions in music perception and production. Nat Rev Neurosci. 2007 Jul;8(7):547–58.

Zhang Y, Sun M. Dynamic flight stability of a hovering model insect: lateral motion. Acta Mech Sin. 2009 Oct 16;26(2):175–90.